MECHANICAL ENGINEERING

SHAPE MEMORY ALLOYS
IN THE DESIGN OF
MORPHING STATOR VANES

by

KASUN WICKRAMASINGHE

JUNE 2016

Supervisors: Dr Jem Rongong and Dr Rachel Tomlinson

Dissertation submitted to the University of Sheffield in partial fulfillment of the requirements for the degree of

Doctor of Philosophy
in
Mechanical engineering

ABSTRACT

The thesis can be summarised as an exercise in linking the theoretical knowledge of Nickel Titanium Shape Memory Alloys to a practical space. Background work includes establishing a thorough understanding of the behaviour of Shape Memory Alloys, locating the opportunities for actuation available in gas turbine engines, and evaluating past studies that utilise SMA technologies in aerospace applications. Using this knowledge base, an experimental methodology is devised, focused on assessing criteria specifically related to SMA actuation demands. FEM techniques are employed, using data from the experimental study, to develop and analyse SMA actuator concepts. The culmination of these various streams of work effects the conceptualization of a novel solid-state flexural actuator for the gas turbine engine variable stator vane assembly.

CONTENTS

ACKNOWLEDGEMENT

This thesis has been brought to a conclusion thanks to the contributions and help of numerous people.

I would like to express my special appreciation and thanks to my supervisors Dr. Jem Rongong and Dr. Rachel Tomlinson who have been tremendous mentors for me over a period of four years at Sheffield. They gave me enough encouragement, guidance and supervision for my research allowing me to grow as a researcher. Their advices on various issues, brilliant comments on my progress and suggestions for alternative actions were always invaluable.

A considerable portion of my research was shouldered by laboratory work. I would also like to thank my laboratory technicians Mr. Leslie Morton and Mr. David Webster who have helped me immensely in experimental plans and tests.

I take this opportunity to also thank my parents Dr and Mrs Wickramasinghe and my in laws Mr and Mrs Ram for all the care, support and encouragement.

Above all, special thanks go to my beloved wife Jessy who sacrificed her time by always being by my side and travelling with me through this stiff journey. The motivation you had given is enormous.

CHAPTER 1
INTRODUCTION

1.1 Background

Gas turbine performance development has been traditionally governed by the "worst case" deterioration and operating condition which leads to large safety margins and severe compromises. This design and control philosophy necessitates rigid limits and margins, and as a result the potential performance of engine components are often not exploited.

One way to overcome this situation is through the introduction of active control of the engine operation using smart materials. Such a system has the ability to diagnose the current operating condition and react with an adequate control action. This results in independent, narrower, more optimised operating envelopes, each catered for a different operating requirement. The flexibility that this system offers lifts the restraints brought about by operational limits or singular events and ensures the best possible efficiency at any given operating condition. As a result, this system can

potentially enhance gas turbine engine capability, environmental impact, safety and affordability.

Shape Memory Alloys (SMAs), a specialised subgroup of smart materials, exhibit severable desirable characteristics exploitable for this purpose. The foremost draw is their ability to convert a non-mechanical input into a mechanical output (actuator) and mechanical input into a non-mechanical output (sensor). The subsequent mechanical response of these materials are typically one or more orders of magnitude greater than the response resulting from conventional material behaviour such as thermal expansion.

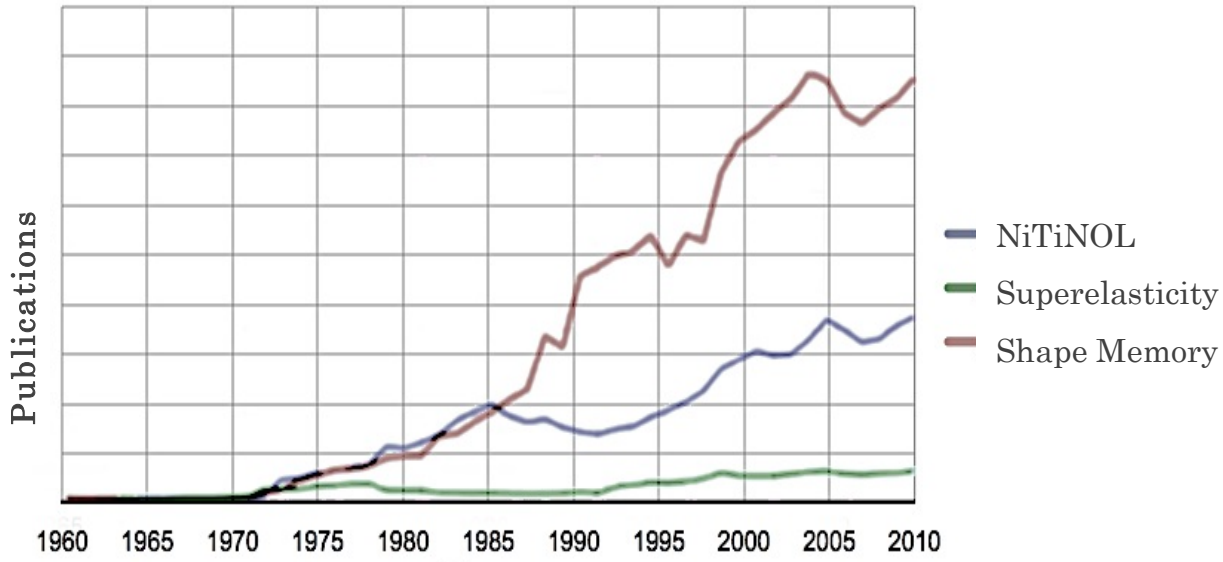

Figure 1.1: *SMA related publications per year (Compiled with data from Stoeckel 2011 [53])*

The unique attributes of NiTi SMAs have lead to their use in different applications. Figure 1.1 demonstrates the exponential nature of the rise in interest since the recent discovery of the property [53]. Due to research into understanding SMA characteristics and control being new, there has not been enough time for this understanding to find its way to real world applications on a large scale. Therefore, the general consensus is that the best uses of the material are yet to come. This has given researchers great impetus in pursuing this research avenue in the hope of finding the "next big thing".

1.2 Purpose of the Study

This study is an exploration into the introduction of actuation and control to gas turbine blades structures. It will comprise the coupling between the extensive requirements demanded by application, to the enormous potential offered by Nickel Titanium (NiTi) SMA plate. These efforts summate towards the conceptualisation of a novel solid-state variable stator vane system incorporating NiTi SMA plate.

From an academic perspective, this study evaluates SMA behaviour from a purely actuator-centric perspective. The experimental study focuses on shape-recovery on four-point bending– replicating operation of a solid-state flexural actuator, to provide a

comprehensive map of NiTi SMA behaviour in the flexural deformation mode. Moreover, through the adoption of in-situ observational techniques, the study evaluates SMA microstructural response as it is subjected to tests replicating actuation behaviour. This enables a correlation study that links microstructural observations and macroscopic responses together.

1.3 Key Contributions

Several contributions have been made in both academic and practical fields through this novel study. The key contributions can be summarised as:

(1) Understanding of NiTi behaviour through thermal and stress induced transformations in the flexural deformation mode.

(2) DIC strain-field analysis revealing microstructural level mechanisms behind the Shape Memory Effect.

(3) Verification and validation of model via comparative study against experimental data.

(4) Development of actuator concepts utilising different deformation/ strain recovery domains.

(5) Development of a Variable Stator Vane concept.

1.4 Structure

The contents of this body of work is organised into seven chapters. Chapter 2 explores current knowledge on the subject area and highlights where this study fits in. The chapter is comprised of 4 specific literature reviews. The first is a review into NiTi SMA, citing the materials unique characteristics, constitutive response and the macromechanical and microstructural factors that govern this behaviour. This follows a review of advances in SMA understanding through experimental studies that utilise light optical microscopy and ones that examine the constitutive response in the flexural bending mode. The third section is dedicated to a review of gas turbine engine stator vane operation. This section identifies shortcomings of the current system, potential opportunities for improvement and past implementations of NiTi SMAs in gas turbine engines. The chapter concludes with an assessment of the ecosystem of SMA modelling approaches.

The experimental techniques employed for this study are highlighted in chapter 3. Key methodologies adapted include; envisioning of test criteria, development of a test schedule to address these criteria, the preparation of specimens that allow for in-situ DIC analysis, and the design of the test stage.

Chapter 4 is dedicated to the experimental findings. The main objective of the study is to map the thermal and stress induced transformation behaviour of NiTi plate under flexural deformation.

In addition, in-situ techniques are employed allowing the simultaneous observation at a microstructural and macromechanical level.

Chapter 5 commences with an introduction of the Auricchio derived built-in ABAQUS SMA model, and an assessment of its criteria. This is followed by a comparative study for verification and validation purposes, against data from flexural and uniaxial tests from the experimental study. FEM modelling techniques are employed to conceptualize two actuator designs, each exploiting a different deformation application/recovery domain. The modus operandi of these concepts and the resulting pros and cons are detailed and discussed. The outstanding concept is further developed into a fully operational variable stator vane.

Chapter 6 is the discussion chapter, which critically analyses the methodological, empirical and artifact contributions in light of the literature review.

The thesis is concluded in Chapter 7, which lists the findings, conclusions and possible future studies stemming from this work.

CHAPTER 2
LITERATURE REVIEW

2.1 Introduction

As this thesis is a unification of many different disciplines, a number of literature reviews on the differing areas is necessitated. To begin with, the thesis explores opportunities for utilising NiTi SMA in future applications, requiring a study of literature concerning the material characteristics (Section 2.2). From an academic perspective, the thesis explores advances in SMA understanding made through using experimental studies (section 2.4), which leads to the conceptualisation of the experimental study. From a practical perspective, the study addresses the pressing issue of gas turbine engine's inability to adapt to different operating requirements, necessitating a study of literature concerning gas turbine shortcomings, opportunities, and past uses of SMAs (Section 2.3). An exploration of SMA modelling techniques is initiated to identify the most suitable model (Section 2.5), with which the novel NiTi solid-state actuator concept is conceived and its operative capability tested. The chapter is concluded with a summary of the findings, identifying gaps in knowledge and justifying the adopted research approach.

2.2 Shape Memory Alloys

SMAs include nickel-titanium, copper-aluminium-nickel, copper-zinc-aluminium and iron- manganese-silicon alloys. Of these, NiTi SMAs, based on an equiatomic compound of nickel and titanium, are regarded as the most useful in commercial applications [1]. Besides the ability of tolerating quite large amounts of shape memory strain, NiTi shows high stability in cyclic applications, possesses an elevated electrical resistivity, and is corrosion resistant [2].

In 1961, William Buehler, a researcher at the Naval Ordnance Laboratory, discovered that NiTi possesses a unique property in shape memory. The alloy was named NiTiNOL after this place. This properties actual discovery is said to have come about by accident: at a laboratory management meeting, Dr. David Muzzey with his pipe lighter, heated a strip of NiTi that was bent out of shape many times, and to everyone's bemusement, the strip stretched back to its original form.

Following this discovery, there was still a question. Exactly, what made these metals "remember" their original shape? Dr. Frederick Wang, an expert in crystal physics, identified the structural changes at the atomic level to be the contributing factor in the unique properties these alloys have [3]. SMA-characteristics were later studied by Warlimont et al [4] and Sun and Hwang [5], who identified five significant phenomena:

1. The Shape Memory Effect by transformation
2. The Shape Memory Effect by re-orientation
3. Pseudoelasticity by transformation
4. Pseudoelasticity by re-orientation
5. The Two Way Shape Memory Effect.

2.2.1 Properties and constitutive response

NiTi SMAs have two stable phases with different crystal lattice structures and material characteristics; the low temperature martensitic phase and the high temperature austenite or parent phase. The common mechanical properties of austenitic and martensitic NiTi and stainless steel are presented in Table 1.1. Lowest and highest values are compiled from picked references [6-9].

TABLE 1.1: Selected mechanical properties of NiTi (austenite & martensite phases) and stainless steel (316LVM) [6-9]

	NiTi		Stainless Steel
	Austenitic	martensitic	
Ultimate tensile strength (MPa)	800-1500	103-1100	483-1850
Tensile yield strength (MPa)	100-800	50-300	190-1213
Modulus of elasticity (GPa)	70-100	21-69	190-200
Elongation at failure (%)	1-20	up to 60	12-40

NiTi in its martensitic phase is soft and ductile and can be easily deformed, somewhat like soft pewter. Austenitic NiTi is strong and hard, similar to titanium. From the point of view of practical applications, another form of NiTi, stress-induced martensite, is particularly important. In this form, NiTi is highly elastic, almost rubber-like. This behaviour is observed at a temperature range below pure austenitic behaviour. The material starts as austenite but transforms into martensite form as a result of applied stress. The constitutive response of each phase exhibited by equiatomic NiTi SMA is schematically depicted in Figure 2.1, highlighting the above characteristics. This figure is an oversimplification with the actual behaviour influenced by many different factors. The following sections will review this behaviour in detail.

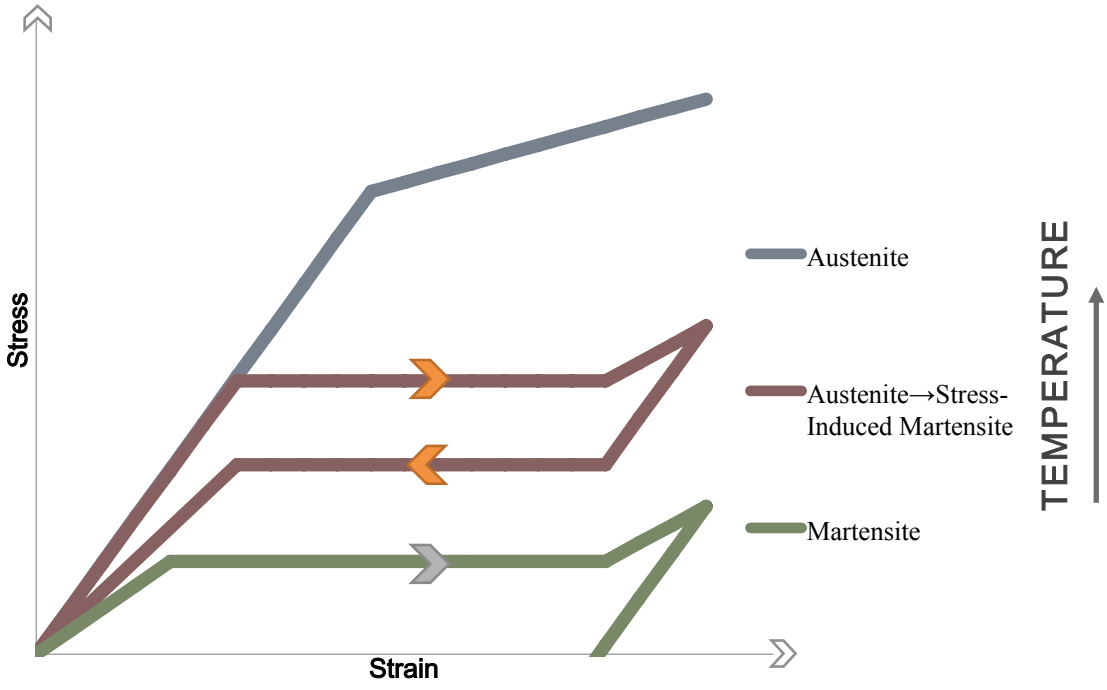

FIGURE 2.1: *Stress strain behaviour of different states of equiatomic NiTi at constant temperature*

2.2.2 Crystallographic aspects of phase transformation

The shape memory phenomenon of NiTi is attributed to a diffusionless solid-to-solid phase transformation between the austenite (parent) and martensitic phase. The austenite phase is characterised by an ordered body centred cubic crystal form (B2 – Figure 2.2 (a)) [10]. Cooled beyond a critical temperature, it undergoes a thermo-elastic martensitic transformation to an intermediate orthorhombic (B19 – Figure 2.2 (c)) phase and then to a distorted monoclinic or "twinned" structure (B19' – Figure 2.2 (d)) referred to as martensitic plane variants, via a shear-like mechanism [11].

The first step in martensitic transformation is known as the Bain strain or lattice deformation, and it consists of all movements that are needed to form the new structure from the old. In real materials, Bain strain generally consists of several atomic shuffles in addition to the movement illustrated [11]. To accommodate internal stresses resulting from transformation to the B19' phase, formation of up to 24 multiple martensitic variants is possible [2]. This part of martensitic transformation is referred to as lattice invariant shear.

One mechanical property that changes during phase transformation is the point of apparent yield (the onset of the stress-strain plateau

in Figure 2.1). The martensitic structure deforms by moving twin boundaries, which are quite mobile. It thus has lower yield strength compared to austenite, which deforms by dislocation generation and movement.

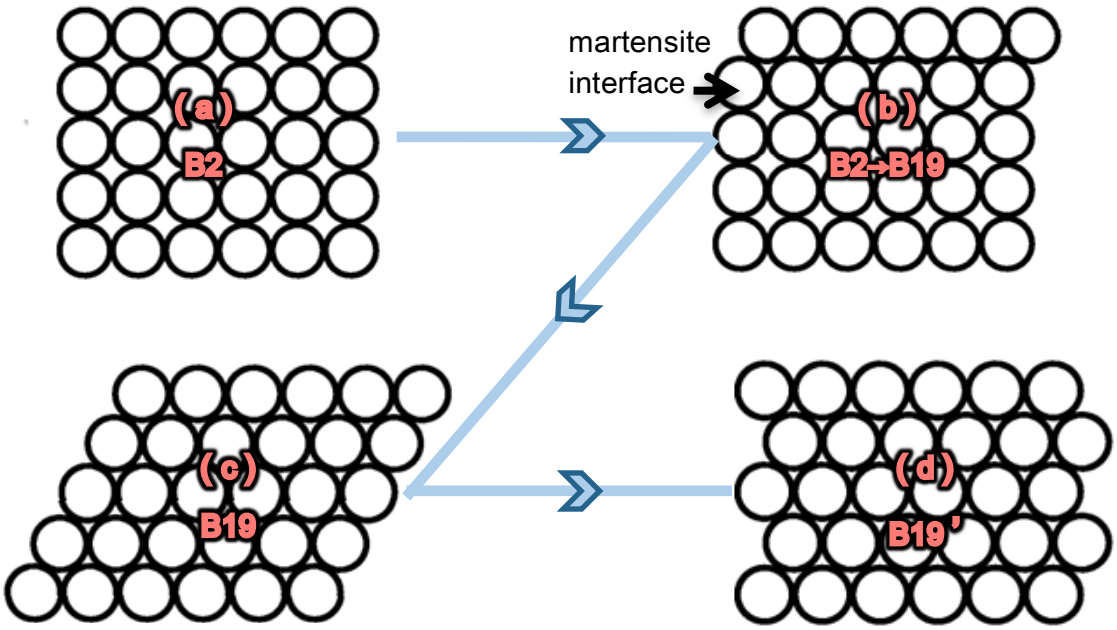

FIGURE 2.2: *Thermally induced transformation from austenite to martensite in two-dimensions (a) B2 - completely austenitic and (d) B19' - completely martensitic (b) the interface advances, each layer of atoms is displaced slightly (c) B19 - intermediate orthorhombic phase*

2.2.3 Phase Transformation temperatures

The transformation to martensite by twinning is completely

reversible [12] and occurs over a temperature range due to the varying local stresses between the grains [11]. There are four stress dependent parameters referred to as the transformation onset and finish temperatures (see below). They characterise the start and finish temperatures to induce forward and reverse phase transformations:

- Forward transformation: (1) M_s, martensite start temperature – austenite begins to change to martensite. (2) M_f, martensite finish temperature – completion of martensitic transformation
- Reverse transformation: (1) A_s, austenite start temperature – martensite begins to change to austenite. (2) A_f, austenite finish temperature – completion of austenitic transformation

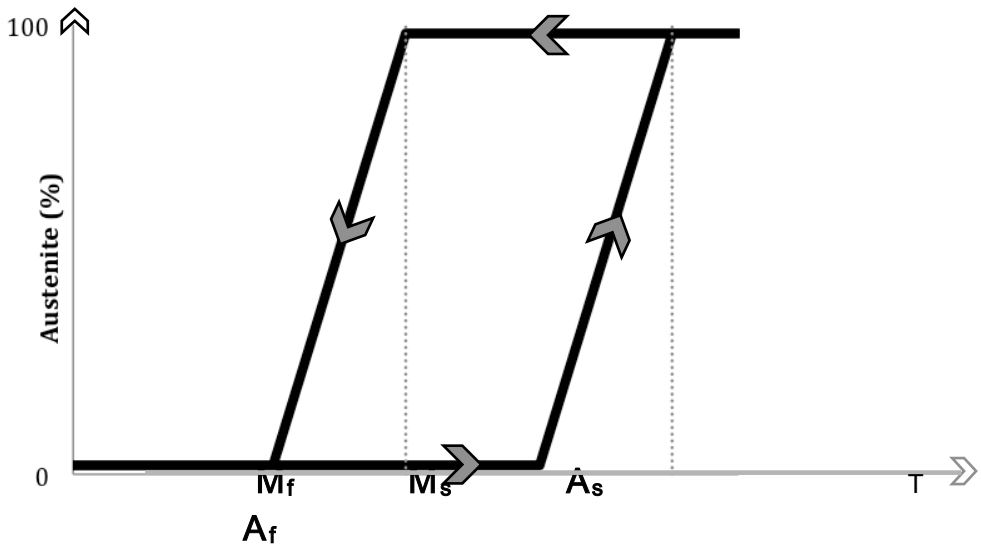

Figure 2.3: *Phase transformation and hysteresis upon a change of temperature*

These transformation temperatures are depicted in Figure 2.3, displaying the relationship between austenite percentage and change in temperature. The forward and reverse transformations result in a thermoelastic hysteresis: the temperature range for the reverse transformation (martensite-to-austenite) is higher than that for the forward transformation. Hysteresis, defined as the difference between the temperatures at which the material is 50% transformed to austenite upon heating and 50% transformed to martensite upon cooling, can be up to 20 to 30°C in NiTi SMAs [6,7]. This can be microscopically attributed to friction associated with the reorientation of twin-related martensite boundaries [11].

An idealized phase transformation diagram for typical NiTi SMA material showing the effects of applied stress and temperature on the transformation characteristics is depicted in Figure 2.4. The transformation temperatures increase linearly with applied stress [14-17] with gradients C_M and C_A, stress-temperature coefficients for martensitic and austenitic transformation boundaries. This linear behaviour is observed until the movement of dislocations in the crystal structure becomes energetically more favourable than the formation of the de-twinned martensite [18]. The red, green and blue shaded areas correspond to twinned martensite, de-twinned martensite and austenite, respectively. At the yellow shaded area, all variants of NiTi are possible, and the stable phase

is determined by temperature history. The grey shaded areas represent where the phase transformations occur.

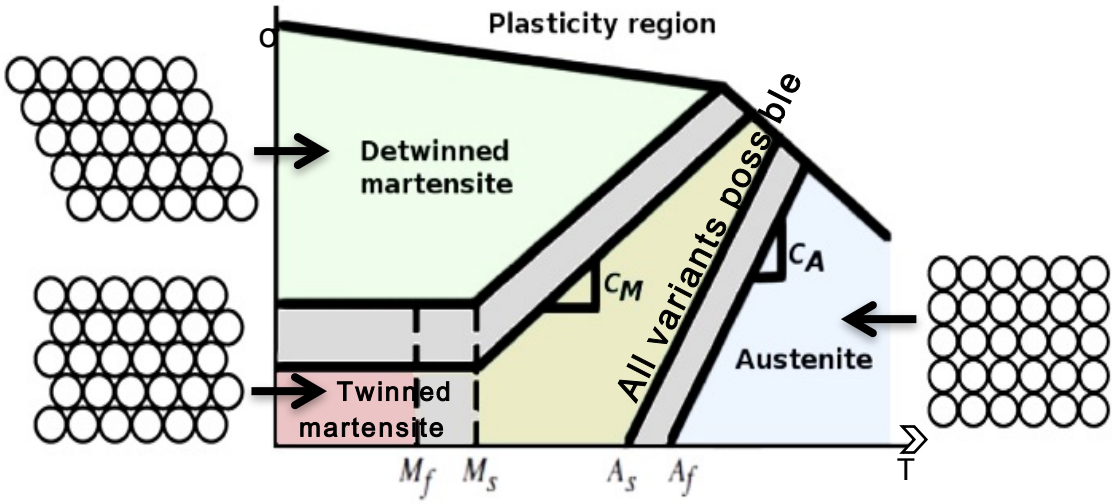

Figure 2.4: *Phase diagram of NiTi SMA showing the effect of applied stress on the transformation temperatures: red - twinned martensite, green - detwinned martensite, blue – austenite, yellow – all variants possible, grey – phase transformation areas*

Generally, the phase transition temperature of an equiatomic - 50%Ni-50%Ti – falls in the region of -50°C→+100°C. These phase transformation temperatures are principally dependent on the alloy composition of the NiTi SMA. The relationship between the nickel-titanium ratio and the onset of forward martensitic transformation is depicted in Figure 2.5. Titanium-rich Ni-Ti contains a second phase Ti2Ni in the matrix and displays higher transformation

temperatures compared to more nickel-rich alloys [20]. Conversely, excess nickel in the alloy reduces the transformation temperatures and increases the permanent yield strength of the austenite phase. As a result, control over the transformation temperatures of NiTi SMA can be achieved during the manufacturing process by altering the alloy composition. The transformation temperature can be further altered through introducing a foreign alloy: an example is $Ni_{20}Pt_{30}Ti_{50}$ alloy which demonstrated transformation temperatures above 530°C [140].

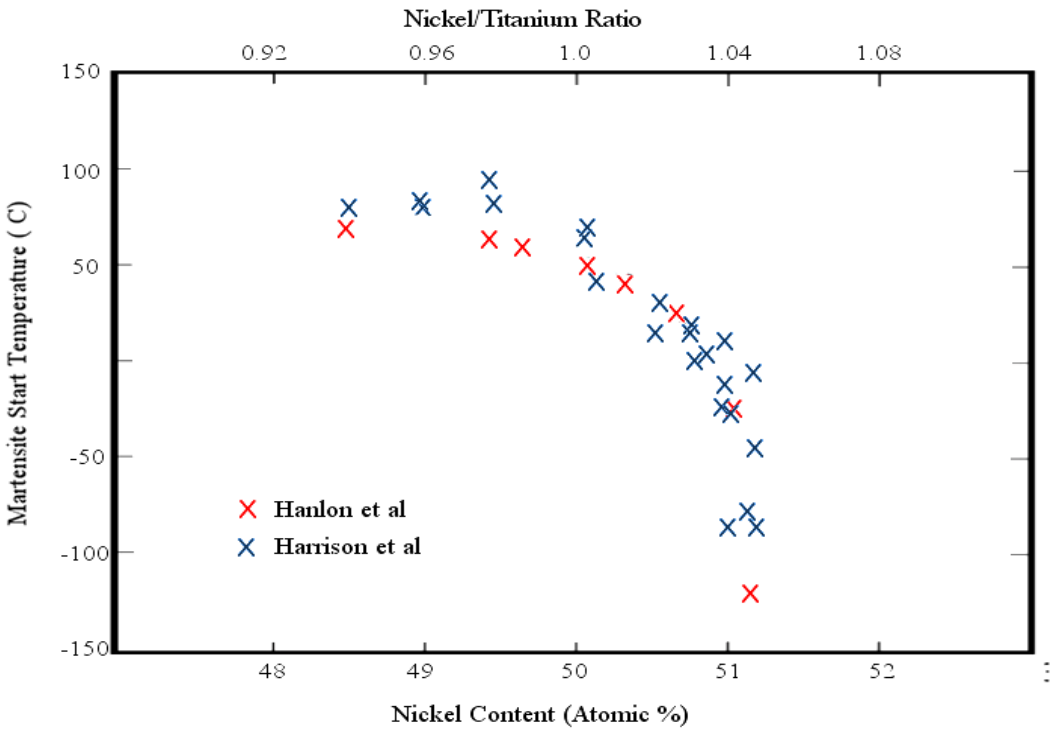

Figure 2.5: *Effect of NiTi alloy composition on Ms Temperature (Compiled with data from Duerig et al [19])*

2.2.4 The Shape Memory Effect

Shape Memory Effect (SME) can be explained macroscopically observing the material deformation as a function of stress and temperature schematically depicted in Figure 2.6 and at a micro level using 2D geometrical concept depicted in Figure 2.7 [19]. Cooling from austenite (point (a) in Figures 2.6 with lattice structure depicted in Figure 2.7) below M_f, the self-accommodating variants of martensite are formed without a macroscopic change in strain (a). During the application of stress beyond the start stress level (σ_s), the reorientation process is initiated. At this stage, the twin boundaries migrate resulting in a biased distribution of martensite variants (known as detwinning) and an observable macroscopic change in shape. The detwinning process is completed at a stress level, σ_f, and is characterised by the end of the plateau in the stress-strain diagram in Figure 2.6. The stress required to cause this movement is well below the permanent plastic yield stress of martensite.

Upon unloading to zero stress, the detwinned crystal form remains. Once this structure is heated above A_f, the detwinned structure transforms to BCC austenite form (a). Regardless of the distribution of martensite variants, there is only one possible austenitic structure. Consequently, it reverts back to its original un-deformed shape. This cycle can be repeated. This shape change

phenomenon is a single occurrence and is referred as the one-way SME. The SME in NiTi alloys allows the material to be used as actuators, taking advantage of the geometrical change observed through reverse transformation.

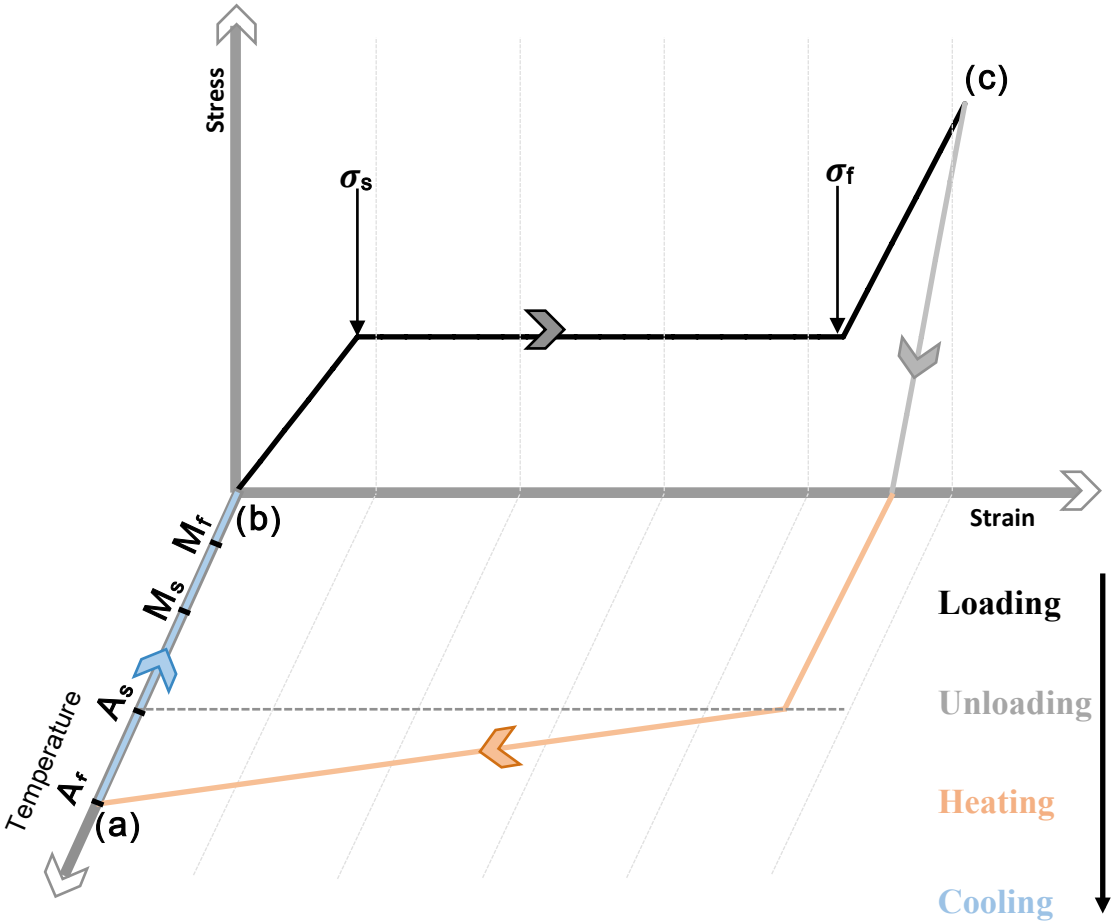

Figure 2.6: *The Shape Memory Effect shown macroscopically: austenite (a) is cooled below Mf (b) without undergoing a shape change, then is deformed through the detwinning process σs → σf to the onset of plastic deformation (c). Heating past Af the original austenitic shape is restored*

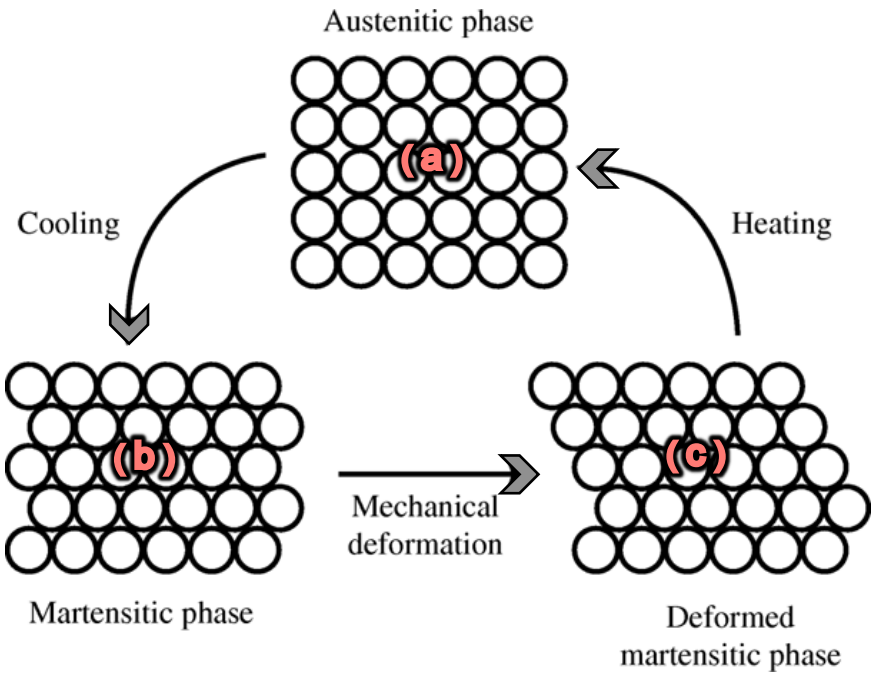

Figure 2.7: *The Shape Memory Effect shown microscopically [19]: austenite (a) is cooled to form twinned martensite (b), then is deformed to form detwinned martensite (c). Heating either state (b) or (c) will return the original austenitic structure.*

SMAs can also exhibit a phenomenon called two-way SME, which has two "memorized" configurations for each phase. This behaviour can be trained through repeated thermo mechanical cycling of martensite along a specific loading path past its thermally recoverable strain. This results in permanent changes in the microstructure, limiting the number of martensite variants, which inhibit self-accommodation and increase the internal strain [21]. Unlike one-way SME, only temperature must be varied to affect the change in shape. The amount of strain recovery through

phase transformation is, however, lower in comparison [12]. Figure 2.8 depicts the macroscopic mechanism for one-way and two-way SME.

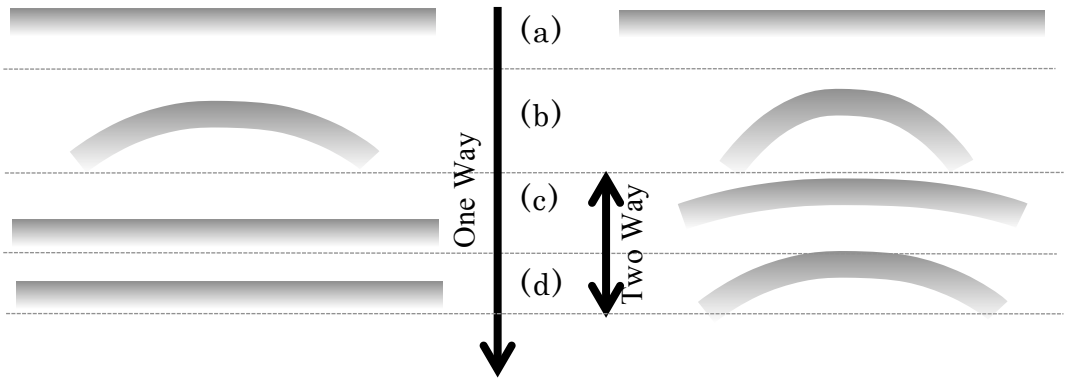

Figure 2.8: *Macroscopic mechanism of One Way and Two Way Shape Memory Effects: (a) martensite, (b) Loaded and Deformed in martensite phase, (c) Heated above Af (austenite), (d) Cooled below Mf (martensite)*

2.2.4b The Rhombohedral Phase

SME can be complicated due to the presence of a R-phase or "pre-martensitic" phase (rhombohedral form) between austenite to martensite transformation [10]. This results in a completely reversible two-step transformation from the parent phase to the R-phase and then to the monoclinic martensitic phase as depicted in Figure 2.9. The transformation to the R-phase consists only of

small changes in the original lattice parameters of the austenitic phase, distorting the original parent cubic phase [11]. According to Wayman & Airoldi [22] and Rivolta [23], the R-phase is always present in forward transformation but is often overlapped by the martensitic phase transformation. The R-phase is affected by factors such as aging [24], increased Ni content in alloying [25], thermo mechanical treatment [26], and thermal cycling [27].

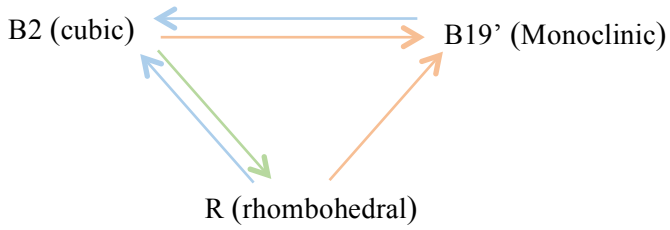

Figure 2.9: *Transformation paths in NiTi alloys: one stage phase transformation B2→B19', two stage phase transformation B2→R-phase→B19', reverse transformation: B19'→B2, R-phase→B2*

2.2.5 Pseudoelastic behaviour

Pseudoelasticity describes the mechanical behaviour of SMAs at temperatures above A_f. It is characterised by large apparent recoverable plastic deformations and encompasses both super elastic and rubberlike behaviour. Representing the SMAs pseudoelastic behaviour, three stages are observed on a stress-strain curve. This is illustrated on Figure 2.10.

For stresses below σ^{Ms} elastic behaviour is observed. When applying stress past critical value σ^{Ms}, the transformation of the parent BCC crystal to the detwinned martensitic crystal form - which is known as stress-induced martensite - is initiated. This is characterised by large transformation strains. The forward transformation is completed reaching σ^{Mf}, where the structure is fully martensitic. Further loading results in an elastic response. The reverse transformation initiates at σ^{As} and completes at σ^{Af} upon unloading. It demonstrates an overall hysteretic response.

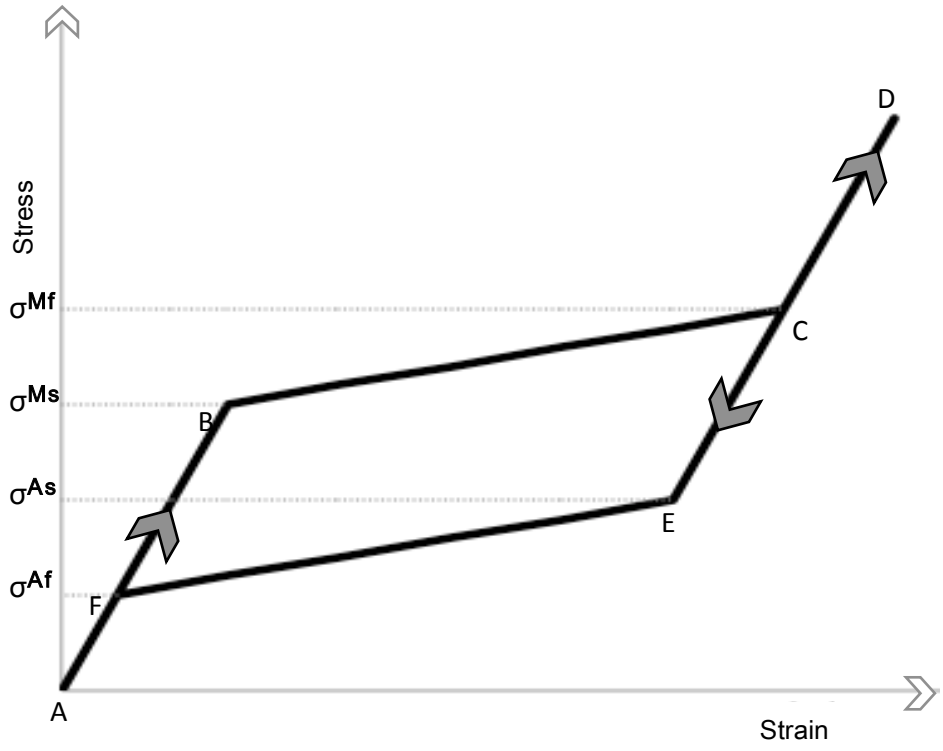

Figure 2.10: *Schematic of pseudoelastic loading cycle*

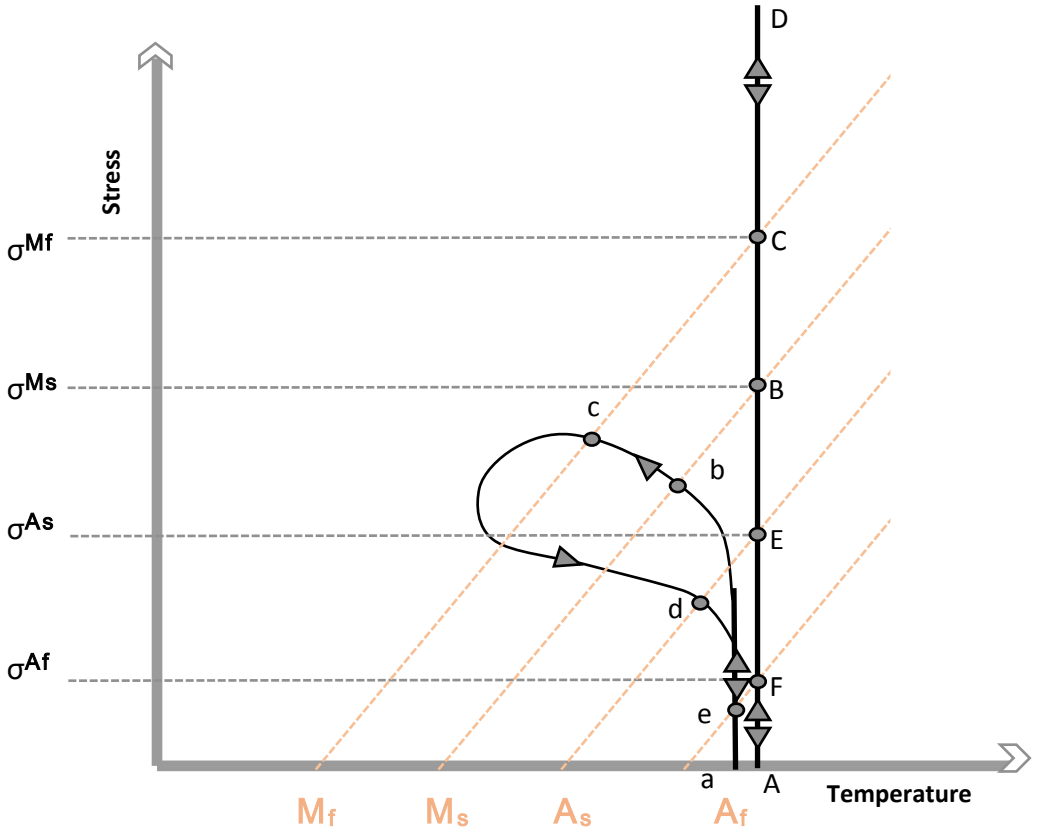

Figure 2.11: *Phase diagram and two possible pseudoelastic loading paths (adapted from Lagoudas 2008 [2])*

To illustrate pseudoelastic behaviour in greater detail, the thermo mechanical loading paths depicted in Figure 2.11, path 1 (A→B→C→D→E→F) – which corresponds to the stress-strain schematic Figure 2.10 - and path 2 (a→b→c→d→e) can be evaluated. The path generally starts at a temperature greater than

A_f (points A & a Figure 2.11), but is mechanically (path 1) or thermo mechanically (path 2) loaded to a stress and temperature where detwinned martensite is more stable (points B→C & b→c). When returned to zero stress state, the material returns to its austenitic phase as temperature is above A_f (points E→F & d→e). Due to the large recoverable strains observed during this process, its use in vibration control applications is popular [2].

2.2.6 Thermodynamic aspects of phase transformation

The phase transformations between the austenitic and martensitic phases are driven either by stress or temperature. This behaviour can be explained using Gibbs theory of thermodynamic stability for an alloy system in equilibrium.

In thermally induced transformations at constant pressure, the stable phase is determined by the entropy of the phases. A general scheme of the Gibbs free energy of the austenite and martensite phase as a function of temperature is reported in Figure 2.12.

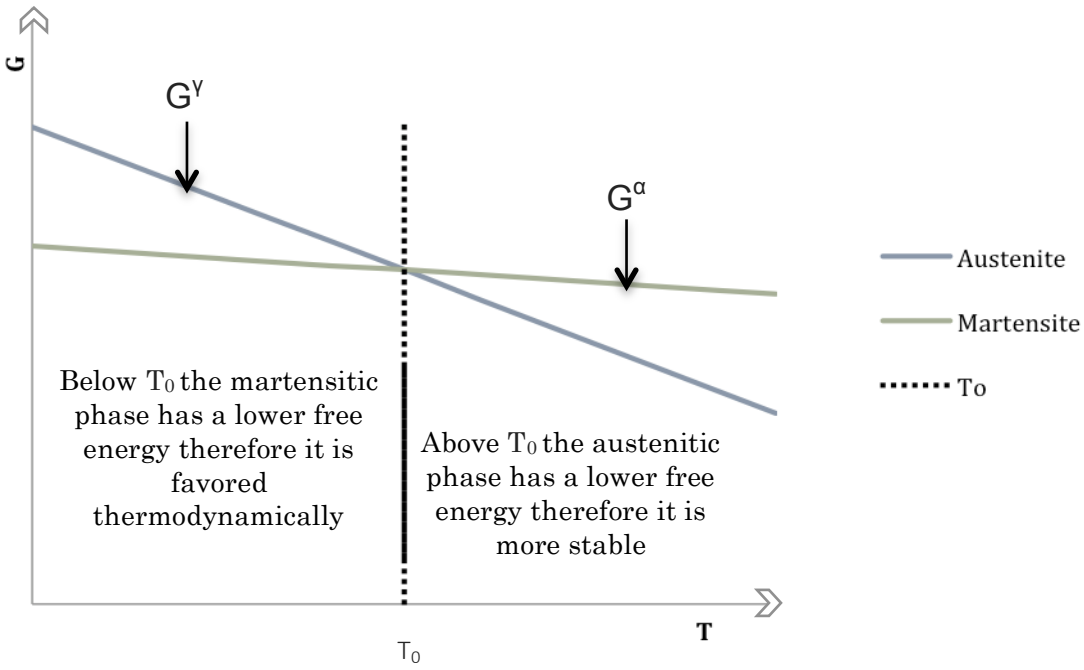

Figure 2.12: *The Variation of G with T for NiTi at a constant stress: below T0 martensite is the stable phase, above t0 austenite is the stable phase*

The stable phase usually has the lower free energy at that given temperature. The two phases have different enthalpies *H* and entropies *G* leading to an intersection of the curves. When this happens, at temperature T_0, the Gibbs free energies of the austenite, γ, and martensitic, α′, phases are equal, i.e.

$$G^{\gamma}(T_0) = G^{\alpha}(T_0) \qquad (1.1)$$

where G refers to the Gibbs free energy. Thus, at T_0 they are thermodynamically in (metastable) equilibrium.

For small intervals of the temperature T, G^{γ} and G^{α} can be

considered to be a constant, and the following relation between the enthalpy H, temperature T and entropy S can be written:

$$G^{\gamma} = H^{\gamma} - TS^{\gamma} \quad (1.2)$$

$$G^{\alpha} = H^{\alpha} - TS^{\alpha} \quad (1.3)$$

In stress induced transformations, where a single crystal SMA specimen is subjected to a uniaxial stress, the expressions for the Gibbs free energy for the parent and the martensitic phases can be written as:

$$(G^*)^{\gamma} = H^{\gamma} - S^{\gamma}T - V_0\varepsilon^{\gamma}\sigma \quad (1.4)$$

$$(G^*)^{\alpha} = H^{\alpha} - S^{\alpha}T - V_0\varepsilon^{\alpha}\sigma \quad (1.5)$$

where G* is the generalized form of the Gibbs free energy, V_0 is the volume of the crystal, σ is the applied stress, and ε is the incremental macroscopic strain.

The variation in stress required to produce stress induced transformations increases linearly with temperature. It obeys the Clausius-Clayperon equation, and is written as

$$\frac{d\sigma}{dM_s} = -\frac{\Delta H}{T\varepsilon_0} \quad (1.6)$$

where ΔH is the transformation latent heat, T is the temperature, σ is the applied stress, M_s is the shifted M_s temperature and ε_0 is the transformational strain resolved along the direction of the applied

stress.

The critical stress required for martensitic transformation increases with temperature until M_d. Above this temperature, the critical stress required to induce martensite is greater than the stress required to move the dislocations. Subsequently, the temperature range for stress-induced transformations is from M_s to M_d.

2.2.7 Damping behaviour

NiTi SMAs exhibit a hysteretic damping behaviour, where the damping force does not significantly depend on the frequency of oscillation. In such a system, the internal damping can be described as a force proportional to the displacement but in phase with the velocity. The following equations drawn from de Silva (2005) [28] describe generic hysteretic damping.

The stress-strain relationship in hysteretic damping is given by

$$\sigma = E\varepsilon_0 \cos\omega\iota - \tilde{E}\varepsilon_0 \sin\omega\iota = E\varepsilon \cos\omega\iota + \tilde{E}\varepsilon_0 \cos\left(\omega\iota + \frac{\pi}{2}\right) \qquad (2.1)$$

where σ is the applied stress, E is the Young's modulus, ε is the material strain and ω the frequency of oscillation.

The material stress has two components given by the RHS of Equation 2.1. The first component corresponds to the linear elastic

behaviour of the material and is in phase with the strain. The second stress component represents the hysteretic damping and is 90° out of phase.

Using the complex form of the response according to

$$\varepsilon = \varepsilon_0 e^{j\omega\iota} \tag{2.2}$$

Equation 2.1 becomes

$$\sigma = \left(E + j\tilde{E}\right)\varepsilon \tag{2.3}$$

This represents hysteretic damping by using a complex modulus of elasticity, which consists of a real part and imaginary part. These correspond to the usual linear storage modulus and the hysteretic loss modulus, respectively.

The energy dissipation per hysteresis loop of hysteretic damping, the damping capacity, is given as

$$\Delta U_h = \pi x_0^2 h \tag{2.4}$$

where ΔU_h is the damping capacity, x is the amplitude of the harmonic motion, h is the hysteretic damping constant which is independent on the frequency.

The specific damping capacity per unit angle of cycle in hysteretic damping is referred to as the loss factor. It indicates the efficiency at which the material loses the energy to molecular rearrangement and internal friction. The loss factor is calculated as the ratio of

the loss modulus to the storage modulus. It is given as

$$\eta = \frac{h}{k} \tag{2.5}$$

where the stiffness k, may be measured as the average slope of the displacement.

2.2.8 Thermo mechanical cycling

During the use as an actuator, an SMA structure is likely to be subjected to repeated temperature cycles through the transformation range under a constant variable load. This is referred to as thermo mechanical cycling (TMC). Studies have indicated that SMA properties such as transformation temperatures, transformation hysteresis, and strain response change continuously under TMC [29-34]. This behaviour is a result of the generation of defects in the microstructure during TMC [20, 29, 35-37]. NiTi SMAs response to TMC is largely dependent on the annealing history and the stress–strain regime of TMC. It is also related to the defects density in the material [33, 34, 38]. Nevertheless, this behaviour is reported to stabilize after a certain number of cycles. Once the material has cleared off TMC effects, the response is predictable and repeatable [32].

2.2.9 Fatigue

Current work on thermo mechanical fatigue of SMAs focuses on high-cycle and low-cycle performance under cyclic mechanical loading either to a constant strain amplitude [39, 42–49] or a constant stress [39–42]. Under mechanical cycling, at constant strain amplitudes within the elastic range (less than 1% strain), the fatigue life of NiTi has been shown to exceed 10^7 cycles. Further increase in the strain amplitude results in a reduction in fatigue life. For amplitudes that induce complete transformation (10-11% strain) NiTi exhibits a fatigue life of 10^3-10^4 cycles [39, 40, 42, 44]. Failure modes during mechanical cycling include catastrophic loss of function by fracture through initiation and propagation of cracks, and the loss of ability to undergo a reversible phase transition. Parameters that affect fatigue behaviour have found to be [2]: stress amplitude [39, 41, 43, 50], complete or partial transformation [42], alloy composition [39, 45, 46], heat treatment [48, 51], environment of testing [33] and surface finish of specimens [40, 50]. Typical recoverable strains for SME and pseudoelastic behaviour in NiTi range from 7-10% for low cycle and 1-2% for high cycle applications [2].

2.2.10 NiTi availability

As NiTi is a tough, complex material, cold machining of NiTi is extremely difficult, and the material is mainly available in either hot formed or simple cold-formed shapes [52]. In the past there have been concerns with the formulating, melting and processing of NiTi SMA, which can often lead to variations of composition at a local level. Such inconsistencies can lead to unpredictable and unrepeatable response, and substantially shorten fatigue life. Nowadays, NiTi specialists such as Memry GmbH are meticulous in balancing the effect of temperature on the material's chemistry against what each process needs to achieve. Such measures have enabled the industrial scale manufacturing of the material to a high consistency level.

NiTi material geometry has been primarily driven by the desired applications into which the NiTi SMAs are envisioned. Because of the promise it has in the lucrative medical market, small diameter SMA wire has received much interest. Wire structures, however, can be only operated in 1-dimension, limited the scope for use in many applications. In contrast, SMA in plate form can exhibit 2 dimensional morphing behaviour and pseudoelasticity. As a result, the application of SMA plates to other structures to either affect damping qualities or induce a SME, is simpler and more effective

compared to SMA wire systems. Further, SMA plates have the potential to be fully integrated as the structural part of a component. And, if large-area plates are employed, they can exhibit higher forces [53].

2.3 Gas turbine Development

There are a number of inherent inefficiencies in the gas turbines that, in theory, with the aid of smart materials such as NiTi, could be eradicated. Current gas turbine designs can be classified as open-loop devices because of the limited on-board computational capacity, the relatively poor sensor technology and an overriding concern for reliability. This favours a mechanically simple system that is unable to respond to changing conditions [54]. This inflexibility means their design is governed by the "worst case" deterioration and operating condition which leads to large safety margins. Presently, the potentially available performance of gas turbine components is not exploitable. This is due different limits and margins being taken into account during the design [55]. These limit the available design space, which could otherwise be used for design optimization.

As discussed previously, SMA plates open a wide range of

possibilities as they can be easily incorporated into other structures. This has given rise to the exiting possibility of incorporating SMA plates into blade structures of the gas turbine compressor. Figure 2.13 depicts these blade structures within a typical triple spool compressor. Triple spool turbofan designs have three compressor stages: (I) the low pressure (fan), (II) intermediate pressure, and (III) high-pressure compressors.

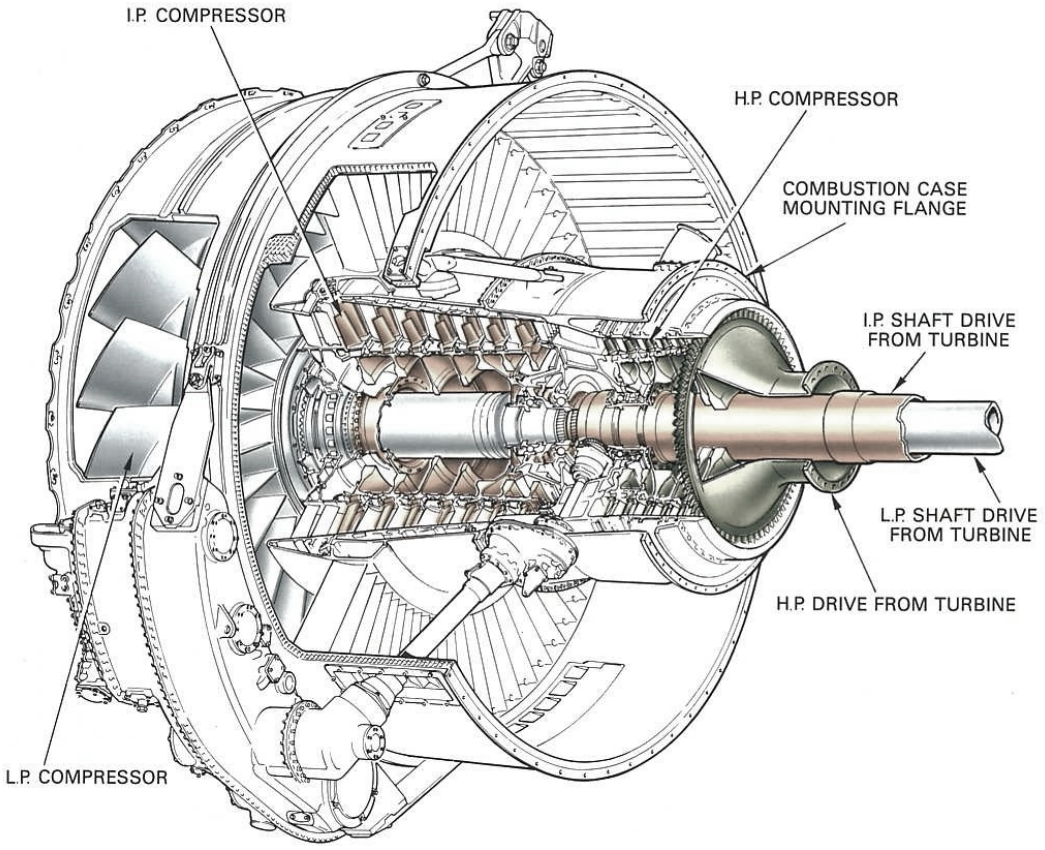

Figure 2.13: *A typical triple spool compressor (Source: Rolls Royce; Soares 2008 [64])*

2.3.1 Blade structures in the gas turbine compressor

The compressor typically consists of alternating rows of rotating and stationary blades called rotor blades and stator vanes, respectively, as shown in Figure 2.14 [64]. Together, these form the axial compressor. The first stationary row in the compressor intake, which comes in front of the first rotor, is known as the inlet guide vane (IGV).

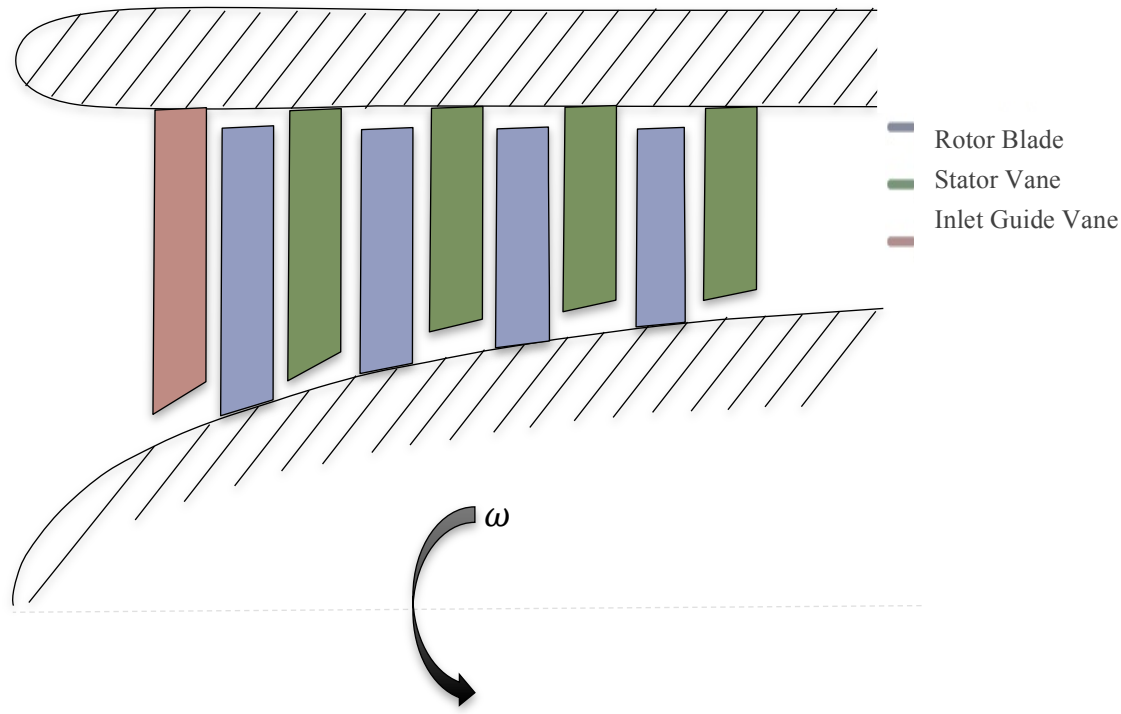

Figure 2.14: *Schematic representation of an axial flow compressor (adapted from Soares 2008 [64])*

The energy exchanges can be evaluated to understand how a compressor operates. The general function of the compressor is to supply large quantities of air at relatively high density for combustion and expansion in the gas turbine and the exhaust nozzle. The rotor blade adds swirl to the flow, increasing the angular momentum and the total energy carried in the flow. The stator removes swirl from the flow. As it is not a moving blade row, the stator cannot add any net energy to the flow. Rather, it converts the kinetic energy associated with swirl to internal energy, raising the static pressure of the flow. The IGV also adds no energy to the flow being a stationary component. It is designed to add swirl in the direction of rotor motion to lower the Mach number of the flow relative to the rotor blades and improve the aerodynamic performance of the rotor.

Additionally, airflow control can be introduced into compressor designs to allow high-pressure ratios on a single shaft. This may take the form of variable IGVs at the first stage, plus a number of stages incorporating variable stator vanes (VSVs) as the shaft pressure ratio is increased. They operate by progressively closing as the compressor speed is reduced from the original design value to maintain an acceptable air angle value into the following rotor blades. Figure 2.15 illustrates a typical variable stator vane system.

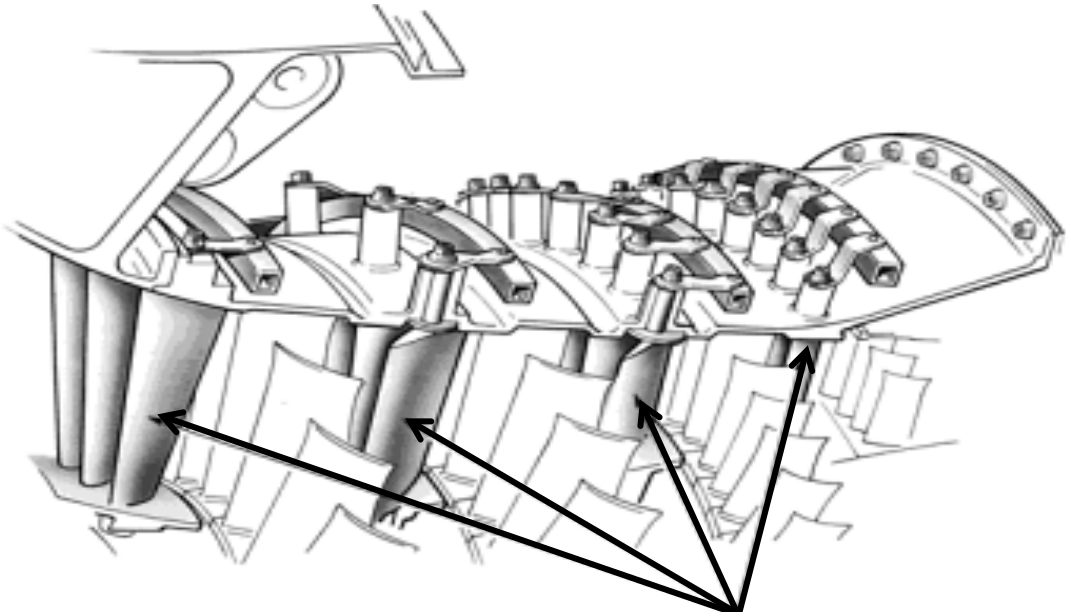

Figure 2.15: *Typical variable stator vanes (Source: Rolls Royce; Soares 2008 [64])*

The latest gas turbines have implemented integral bladed rotor (IBR) designs; Rolls-Royce Trent XWB uses IBRs from stages 1 through 3; GE GEnx also uses IBRs for some stages. IBRs are made from a single component consisting of a rotor disk and blades. They can be integrally cast, machined from a solid piece of material, or made by welding individual blades to the rotor disk. In addition to being lighter and stiffer, IBRs eliminate balancing problems experienced by hub and blade rotors, reduce vibration and remove air leakage paths that occur in hub and blade rotors,

increasing the propulsive efficiency of the engine [75]. Further, the removal of the dovetail attachments eliminates a common source for crack initiation and subsequent propagation [75]. However, any damage to IBR blade necessitates the full removal of the engine to replace the IBR or weld replacement blades. Fuel efficiency improvements of up to 8% have been observed in IBR designs [75].

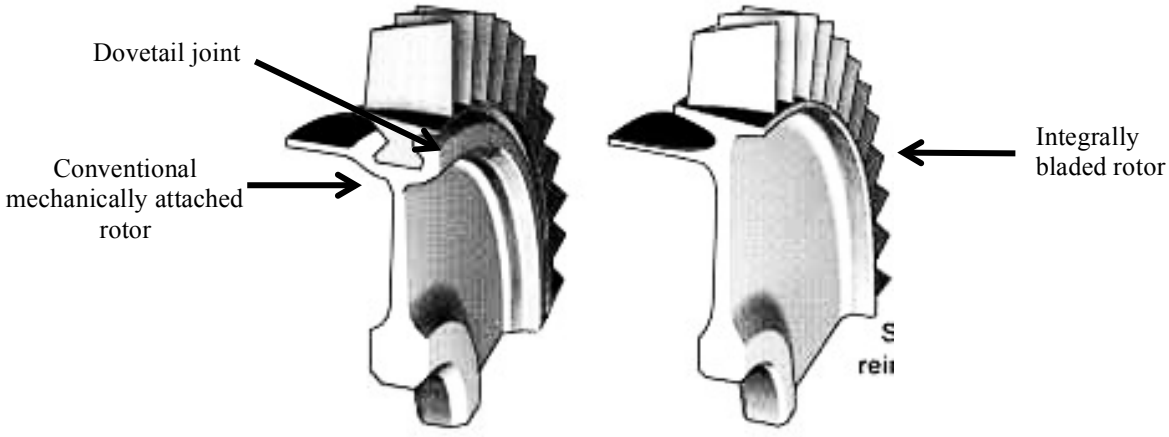

Figure 2.16: *Comparison between (a) Conventional mechanically attached rotor and (b) Integrally bladed rotor designs (source: Soares 2008 [64])*

The pressure and temperature environment through the Rolls Royce Trent 800 turbofan engine are depicted in Figure 2.17. The temperatures at the low-pressure compressor ranges from -50°C to 40°C, the intermediate compressor 50°C to 300°C and the high-pressure compressor 300 to 650°C [65]. Identifying operating

temperatures at each stage of the compressor is important due to the thermo mechanical nature of SMAs.

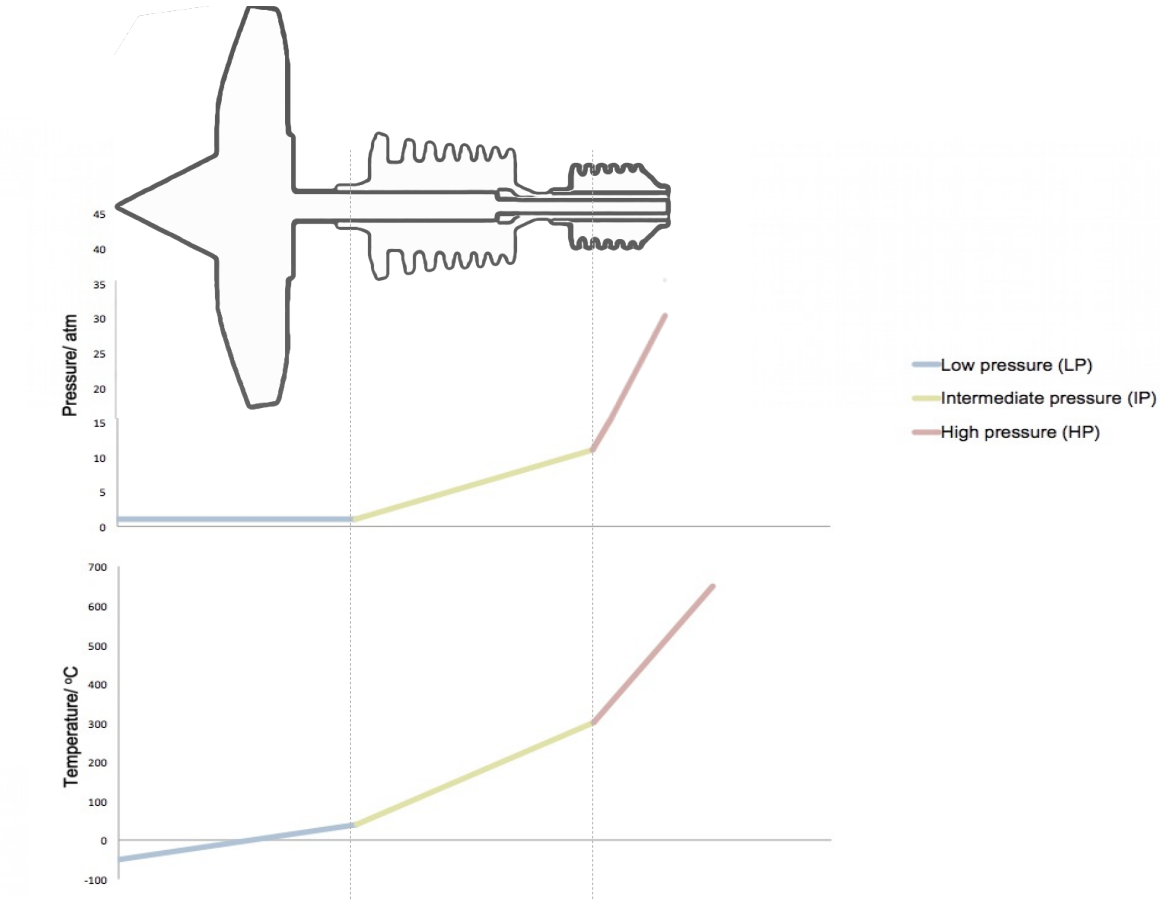

Figure 2.17: *Temperature and pressure profiles through gas turbine compressor stages (Adapted from Cervenka 2000 [65])*

2.3.2 Scope for NiTi SMAs in blade structures

The benefit of introducing NiTi to blade structures in the gas turbine compressor could be categorised by its purpose: (1)

vibration control or (2) actuation.

The ***pseudoelasticity*** of SMA can be utilized to damp these structures to stop high cycle fatigue failure from occurring. The resulting reduction in amplitude still allows the components to be designed with critical resonances in the operating range. This, in turn, lifts aerodynamic design restrictions and reduces the component weight and the noise signature developed by acoustic vibrations. Opportunities for vibration control using NiTi alloys in the blade assembly can be categorized by its role: material, aerodynamic or friction damping. Aerodynamic damping highly depends on geometry of the blades and may become negative and induce flutter. Friction damping has traditionally been an effective and feasible means of vibration control [66]. However, the introduction of integrally bladed rotor designs has negated opportunities for friction damping [75]. The possibilities for material damping are quite low employing existing methods. However, NiTi in plate form is an excellent candidate for material damping. It combines the qualities of pseudoelasticity such as large damping capacity, large recoverable plastic strains, high fatigue life (under small strains) and corrosion strength, and the inherent plate quality of effective integration into the blade structure. Damping these structures would allow designs within the critical resonances as vibration amplitudes are reduced.

Using the ***Shape Memory Effect*** the geometry of the blades

can be adapted according to the aerodynamic requirements during compressor operation. Here, the incidence/deviation angle of flow would increase/decrease as the compressor operates at different mass flow rates compared to design conditions. Such a system would dynamically alter the performance during flight allowing designers to create engines that are lighter, more fuel efficient along with smaller environmental footprints. The operation range of the engine could also extend yielding safer transportation systems. The use of NiTi SMAs as mechanical actuators brings the following advantages [67]:

1. High power/weight and stroke length/weight ratios: Maximum strain and stress limits up to 8% and 700MPa, respectively. SMA is frequently assessed as having one of the highest energy densities of materials that exhibit direct coupling, as depicted in the actuation density diagram (see Figure 2.18).

2. Integration of sensory and actuation functions: This eradicates the need for external electronic sensors and control to initiate actuation.

3. Function in a clean, debris-less and spark-free manner: SME, being an inherent material property, is not associated with moving parts that require lubrication or electrical signals with a potential to spark.

4. Integration of structure and SMA. Solid State SMA alloys

have the capability to be fabricated in a form allowing it to be embedded as a tension member within a structure.

5. Function in high to zero gravity environments: This is due to SME being predominantly thermally induced.

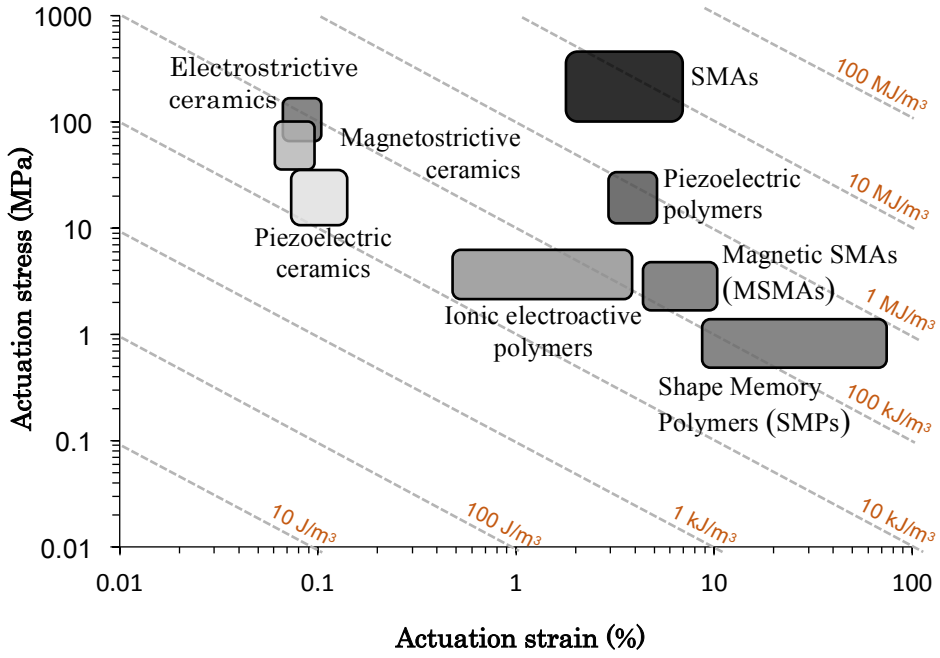

Figure 2.18: *Actuation density diagram indicating typical ranges for actuation stress, actuation strain, and the actuation densities of different active materials that exhibit direct coupling (adapted from Lagoudas 2008 [2])*

NiTi SMAs have many advantages over traditional actuation and damping mechanisms, but do suffer from a series of limitations that

may impede practical application.

1. Actuation frequency: SMAs exhibit a low frequency response as depicted in Figure 2.19. This restricts the use of the material in applications where quick activation times are demanded. However, actuation frequency is not a core factor in this application. Operating demands that call for blade actuation only change in extreme conditions such as take-off/landing.

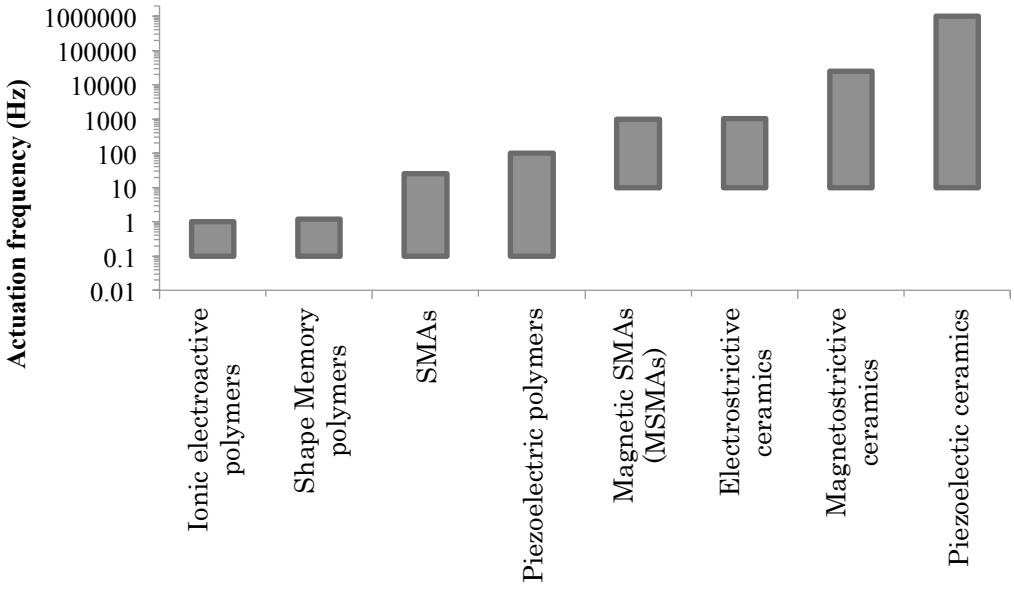

Figure 2.19: *Actuation frequency diagram comparing the actuation frequency ranges of different active materials that exhibit direct coupling (adapted from Lagoudas 2008 [2])*

2. Actuation symmetry: Actuation is typically induced electrically through Joule heating. Deactivation to the martensitic state occurs by free convective heat transfer to the ambient environment. As a

result, actuation is typically asymmetric, with relatively fast actuation times and slow de-actuation times. Several methods have been proposed to reduce the deactivation time and the asymmetry observed, including forced convection, and lagging NiTi with a conductive material in order to manipulate the heat transfer rate [73].

3. Fatigue: NiTi damping and actuation systems are subject to fatigue through cyclic deformations. This can result in the initiation and propagation of cracks that eventually lead to catastrophic loss of function by fracture. In addition to this failure mode, SMAs are also subject to functional fatigue, whereby it loses (to some degree) its ability to undergo a reversible phase transformation.

4. TMC effects: under TMC NiTi characteristics can change continuously (see section 2.2.8 for more detail). This behaviour only stabilises after a large number of cycles.

5. Unintended actuation: As the ambient temperature at the compressor blades can be affected by external conditions and operating requirements, unintentional actuation may occur. Such instances are magnified due to the high velocity airflows present that accelerate heat transfer rates. This can be negated by employing adequate insulation.

6. Operating temperature: SMA operates under a specified temperature envelope. As a result, SMA implementation is

limited in areas where the engine environment is too hot. However, some parts of the gas turbine engine, including the Variable Stator Vanes fall within acceptable temperatures for SMA actuation.

2.3.3 Prior uses of SMAs in gas turbines

Attempts have been previously made to incorporate SMA to gas turbines to improve operation. However, none of these solutions have yet made its way to current gas turbine operation. This section explores instances where SMAs were introduced to end world applications in the Aerospace industry and research in their potential use with a particular focus on actuator concepts and implementations to gas turbine engines. This latter study is further subcategorized in accordance to the configuration of the SMA and deformation/activation mechanism utilised.

Engine noise levels during take-off and landing are exceedingly regulated worldwide. To reduce this noise, an on-going attempt by Boeing USA implements SMA beams in a chevron nozzle for the outer nacelle of a General Electric GE115B engine, which withdraws the serrations at altitude [56-61]. This allows the chevron nozzle to be one shape for take-off - bending the chevrons into the flow, which increases mixing and reduces noise - and then once out of noise sensitive regions, it can be another, straightening

the chevrons for an aerodynamically efficient shape. A picture of this system in operation is depicted in Figure 2.20.

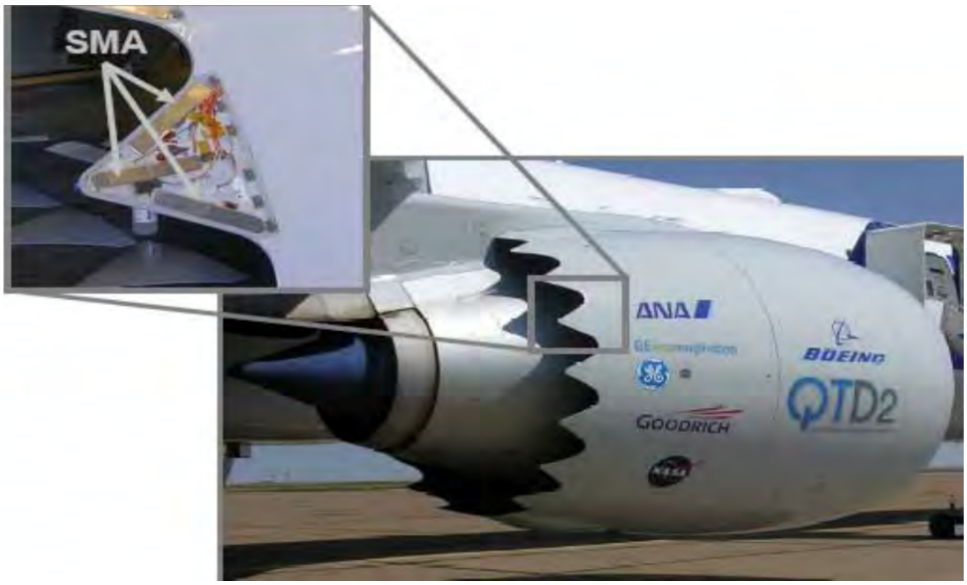

Figure 2.20: *Reconfigurable engine nozzle fan chevron using SMA (courtesy of Boeing)*

An alternative solution, the SMA hybrid composite chevron has been developed by NASA to address the active chevron challenge (as depicted in Figure 2.21). Morphing is established by alternate heating of SMA strips, which build up asymmetric stresses and create a bending moment. The SMA strips are installed on opposing sides of the chevron centroid during the fabrication process to induce this behaviour [2].

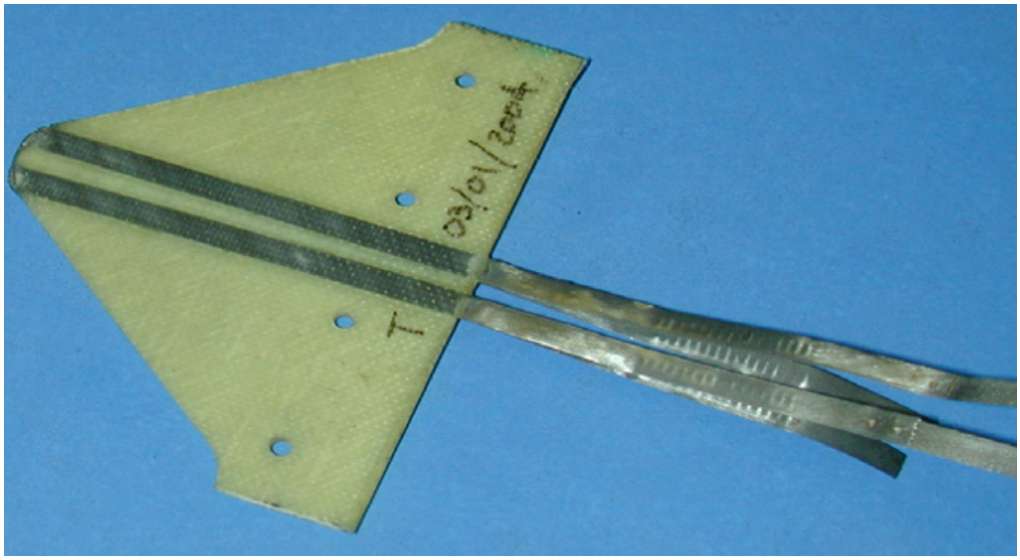

Figure 2.21: *SMA hybrid composite chevron concept (courtesy of NASA) demonstrating an opposed type actuator implication*

The 'Smart Wing' program through partnership with the Defense Advanced Research Projects Agency, the Air Force Research Laboratory, NASA and led by researchers at Northrop Grumman Corporation explored development of a new adaptive wing utilising SMA "tendon" and "torque tube" actuators for geometry modification of the trailing flap and wing twist respectively. Improvements of up to 30% for missile and bomb carriage and an aerodynamic drag reduction of 20% to 40% were forecast. At the time, the study assessed the technology readiness or maturity level for the smart wing at being around 5. Furthermore, their work discovered that torque requirements for a full-size fighter aircraft wing fell outside capability of any actuation material or method present at the time. The low bandwidth of the control surfaces also

prevent potential use for operational aircrafts. Figure 2.22 shows the layout of their Smart Wing concept.

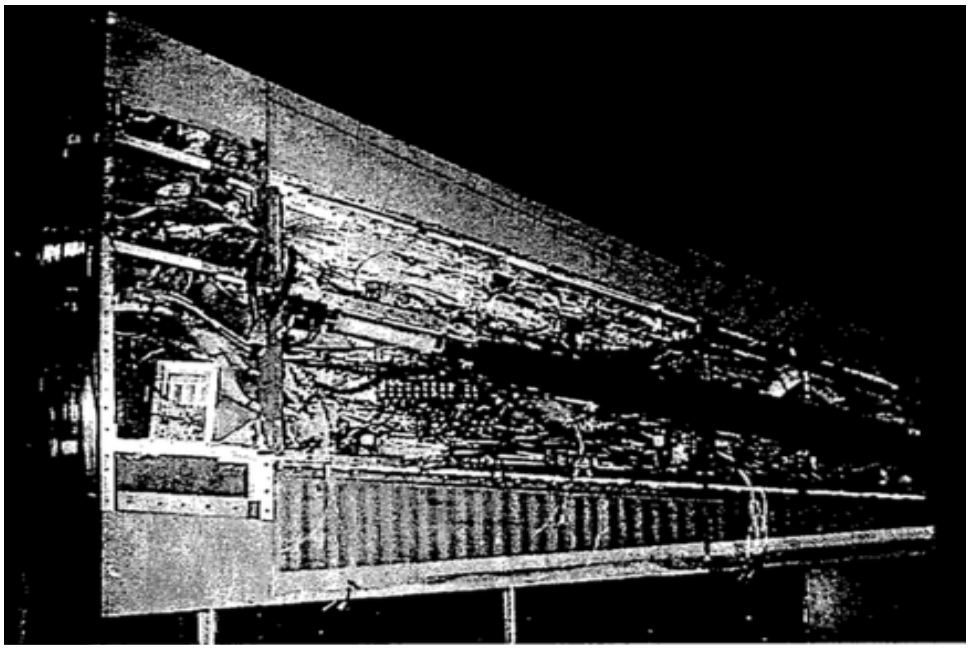

Figure 2.22: *Layout of the Smart Wing developed by Northrop Grumman (courtesy of Northrop Grumman)*

Another study was conducted in the US research programme 'Smart Aircraft and Marine Propulsion System Demonstration' (SAMPSON) with McDonnell Douglas, Lockheed Martin, Georgia Institute of Technology, NASA, the Naval research laboratory, General Dynamics- Electric Boat Division and Pennsylvania State University as partners [62]. The study projected gains of up to 20% in range, in addition to improved manoeuvrability, flutter and buffet control, and a reduced signature in terms of radar detection.

A full size wind tunnel demonstration of an SMA actuated F15 intake – as depicted in Figure 2.23 - with variable upper ramp and smooth shape changing lower lip was produced through the use of SMA bundles containing 34 wires/rods. This mechanism was able to achieve a total force of 26,700N and a rotation of 9°. Limitations were observed in the slow retraction time due to the cooling inefficiency of the low temperature SMA. Further, the availability of the SMA in wire form only necessitated an over complex chain driven mechanism.

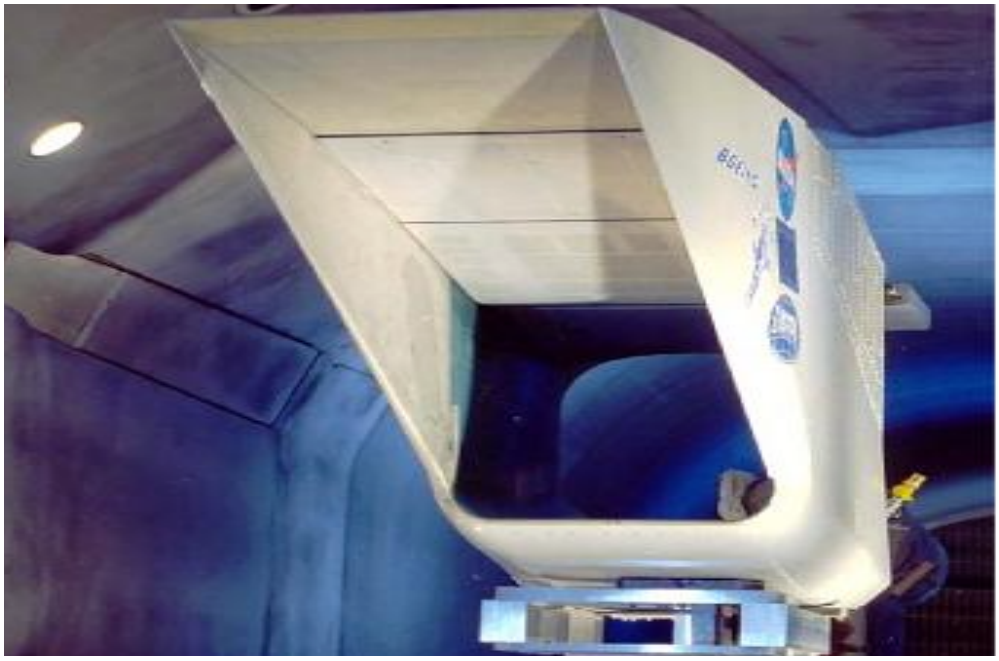

Figure 2.23: *The SAMPON F-15 inlet cowl (Installed in the NASA Langley transonic wind tunnel - courtesy of NASA)*

The European Program for Actuation Technology In Future Aero-

engine Control Systems (ADVACT) evaluates the possibilities of using NiTi SMA in the form of large sections with improved transformation temperatures (M_f > 50°C) for adaptive nozzles [72]. A working demonstration of a "wavy" variable area nozzle was developed giving control over the area of civil engine nozzles. Finite Element Method computational techniques were employed for modelling and validation of this concept. The concept developed by this team is shown in Figure 2.24.

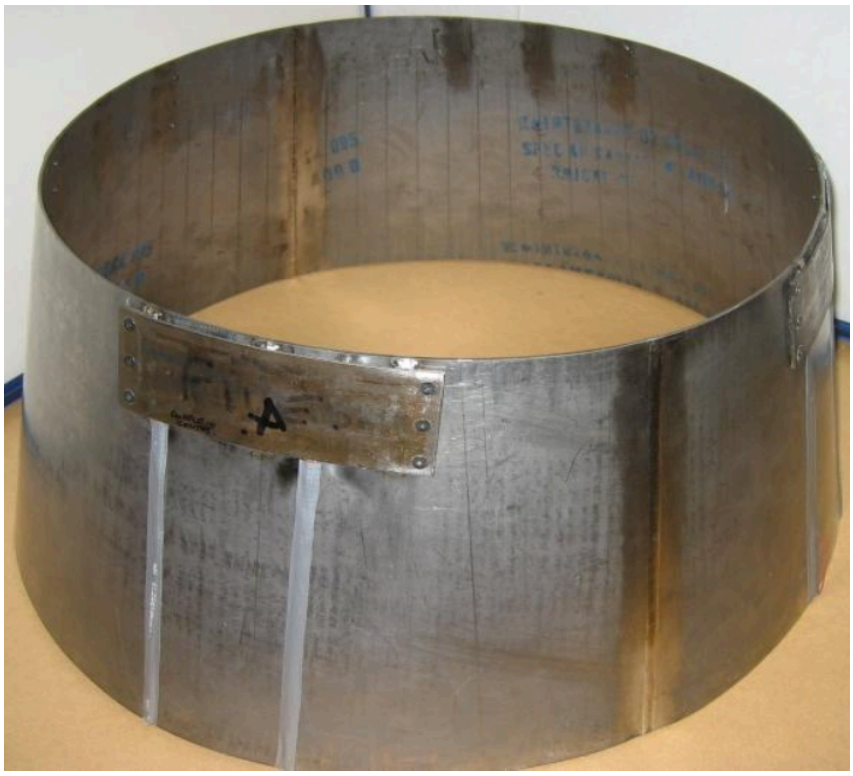

***Figure 2.24**: "Wavy" variable area nozzle (courtesy of ADVACT)*

A parallel study by ADVACT developed a single sector of a variable nozzle exploiting a lower risk interlocking slats approach – depicted in Figure 2.25. This solution has been tested in a wind tunnel with complete simulated flight cycles being achieved.

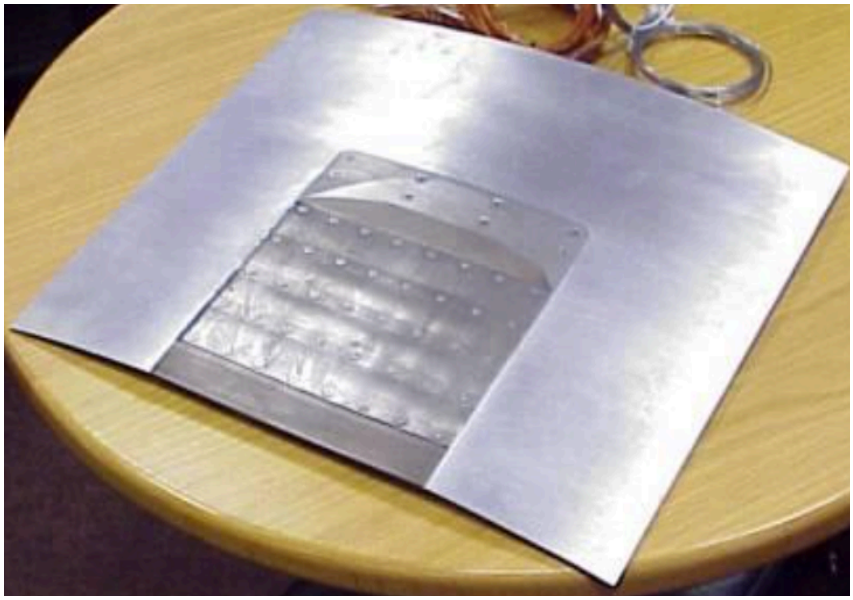

***Figure 2.25**: Variable nozzle "interlocking slats approach" (courtesy of ADVACT)*

Another active research area is SMA blade twist actuation [2]. SMAs with their high actuation density are ideally suited for applications where the available volume is limited. ADVACT has conducted a study for the actuation of titanium compressor blades [72]. The project reports development of large area NiTi actuator

coatings employing low-pressure plasma spraying techniques. It was noted that further work is required to operate this as an actuator. The NiTi coated compressor blade developed by ADVACT is shown in Figure 2.26.

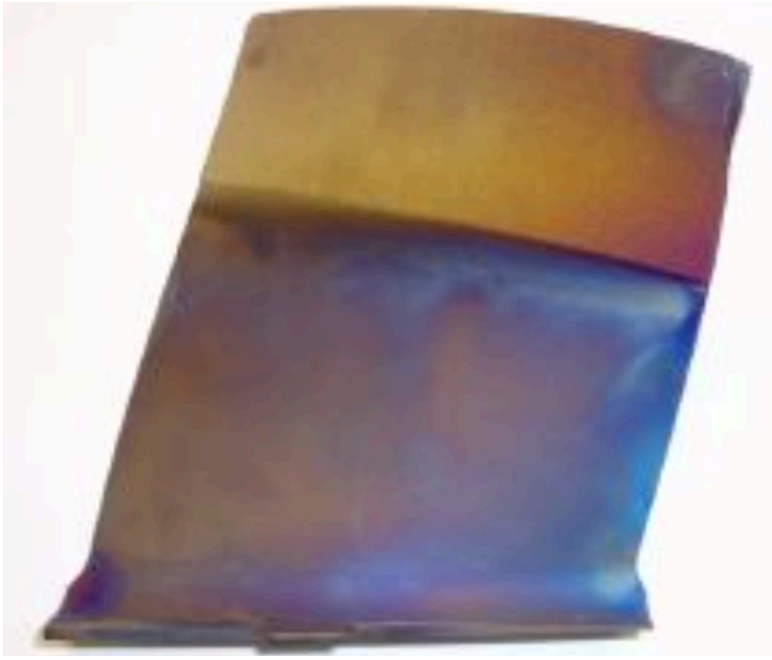

Figure 2.26: *Compressor blade coated with NiTi SMA (courtesy of ADVACT)*

There have also been numerous studies into utilizing the pseudoelastic qualities of SMA to control vibration characteristics in gas turbine structures. Rolls Royce has conducted such research and filed a patent for the use of SMA as a damper in a bearing assembly to damp vibrations of a rotatable shaft [63].

Research has also been carried out in the area of dynamic property optimization that takes advantage of the changing elastic stiffness via phase transformation [2, 74]. This behaviour, which is secondary in many applications, can be used to manipulate the dynamic response of a structure. One study reports the possibility of decreasing the thermally induced deflection of a structure by pre-straining [74]. Further, this changes the structural flutter response, as the natural frequencies for each mode of vibration are decreased due to the added weight and reduced stiffness.

2.4 Advances in research through experimental studies

This section explores previous studies related to this work. It is approached in two unique angles; (1) a review of previous studies that incorporate in-situ loading and microscopy to observe material behaviour, and (2) the academic progress made in understanding the constitutive response and properties of SMAs under tension-compression or bending. These two key areas have been recognised as been fundamental in identifying the void in the research whilst establishing the theoretical framework and methodological focus for the experimental fragment of this work.

2.4.1 In-situ observation of SMA behaviour: Light optical microscopy

Studies that employ a combination of in-situ loading and microscopy [4-12] are of a particular interest as they offer a rich understanding of SMA response that addresses both microstructural and macromechanical response simultaneously.

Using optical techniques to investigate binary NiTi has been found to be very challenging however, due to the fine martensite plates that characterise its microstructure. One effective method has been presented by Lee et al [99]; in their study, etching of the specimen surface was conducted through hydrofluoric acid. The presence of martensite was identified through presence of surface relief on the specimens. This procedure was very intensive however as constant polishing and optical examination was required to eliminate the oxidation layer present on the surface (without the eradication of this layer it was not possible to successfully etch the surface). Additionally, the presence of hydrofluoric acid introduces a host of health and safety hazards to this study.

Escher et al [100] avoids the use of concentrated hydrofluoric acid in their proposed etching technique, which allows light optical microscopic observation of both austenite and martensite phases of NiTi SMAs. They employ traditional grinding and polishing methods initially – grinding is accomplished using silicon carbide

paper with up to a 1000 grit coarseness, which is lubricated using water. This is followed by the use of a 6 micron diamond slurry to polish the specimen surface. Due to the ineffectiveness of etching on the mechanically polished surface however – attributed to the build up of deformed layers – a further electro-polishing step was introduced. This was conducted using a Stues electrolyte A2 at 20 Volts for a duration of 25 seconds. The specimen is dipped into an etchant consisting distilled water, hydrochloric acid, sodium metabisulfite, potassium metabisulfite, and ammonium hydrogen fluoride for 20 seconds for etching to occur.

There have been several studies that have conducted in-situ microstructural analysis utilising the aforementioned etching treatment techniques. Of particular note is work conducted by Miyazaki et al. Through optical microscopy, they observed the phenomena of martensite variants coalescing to form the most favourable variant according to the loading direction. Additionally, thermo mechanical cycling of specimens revealed build up of residual martensite near grain boundaries.

Optical microscopy has also been employed to observe NiTi SMA behaviour at a macroscopic level. One such study was performed by Shaw et al in 1995 [102] and 1997 [103]; they acquired the macro level transformation and thermal signature of the specimen using a standard camera and a thermal camera respectively. Ingeniously,

they employed the naturally occuring oxide layer already present, which, through loading revealed striking macroscopic transformation bands. This occurrence was also synchronised with the release of latent heat detected through the thermal camera.

Brinson et al present a similar study with simultaneous in-situ loading and optical observation. This study is differentiated through the investigation of both microstructural and macroscopic regimes coupled with stress-strain data. A digital camera is used to capture macroscopic photographs, whilst a microscope equipped with an surface relief contour enhancing interference filter and fitted with a digital video camera, allows observation at a microstructural level without the prerequisite of elaborate etching treatments. These lenses enable martensite variants to be easily tracked through changes in the surface angle.

Using this methodological framework, Brinson et al clarified several aspects of the transformation behaviour under loading at different strain rates and fatigue. This included observations of low-cycle localized plastic deformation, correlations between latent heat release and stress relaxation, and a refined definition of "full transformation" for polycrystalline materials [12].

2.4.2 Constitutive response of NiTi: Bend studies (tension-compression)

A thorough understanding of the flexural performance of NiTi plate is required for the implementation of a NiTi based actuator system. Previous studies have primarily evaluated material behaviour under tension employing mostly uni-axial loads. To this date, only four experimental studies have addressed SMA behaviour under compression or bending, despite the prevalence of these deformation modes in applications.

Most bend studies have restrained from using traditional point-bending fixture tests; instead, they have opted for custom-built pure-bending apparatus. Studies on small diameter NiTi wire naturally restrict point-bending fixtures as a result of small radii of curvature and large displacements - conditions where undesirable axial loads can develop due to the support constraints.

The studies conducted by Berg [13] and Bundara et al. [14] have employed moment-controlled experiments to assess the constitutive relationship between applied pure bending moments and the resulting curvatures. These studies, however, suffer a major limitation due to their lack of control over strain rate, leading to a significant impact on the stress/strain response during phase transformations [12]. More recent work by Rejzner et al. [15] and

Reedlunn et al. [16] avoid this problem by using displacement-controlled, custom pure bending fixtures integrated into the load frame.

The study by Reedlunn et al. [16] is particularly interesting as they used larger diameter NiTi tube instead of wire, which negates the requirement of a small radius of curvature to incur strain. Additionally, the resulting smaller deformations and larger specimen dimensions allow the use of in-situ imaging techniques in the guise of Digital Image Correlation for strain measurement. Their experimental tests were able to discover a significant asymmetry between the compressive and tensile deformation modes. This resulted in a shift of the neutral axis towards the compressive side to equalise the distribution of tensile and compressive stresses in the cross section. One limitation that was noted, however, was the appearance of the Brazier effect [101], the tendency of thin walled tubes to ovalise in bending due to longitudinal tension and compression [17]. Ovalisation is particularly undesirable if it leads to variant re-orientation along this new deformation path at a granular level as it questions the homogeneity over compressive and tensile responses in their bend tests.

This could also result in accelerated development of stress localisations under fatigue, which could lead to premature failure

[12]. Another limitation encountered by Reedlunn et al. was through undertaking tests in at room temperature without direct measurement of the specimen temperature. This procedure is not ideal because of the high temperature sensitivity of NiTi.

A common theme to most bending studies is the exclusive focus on SMA behaviour in its Superelastic phase – stress induced transformations at the outer fibre of the beam are not typically induced. This can be attributed to the myriad of applications that already employ Superelastic SMAs in this deformation mode, making it a more lucrative research area. Moreover, most studies on bending have followed a macro level approach to exploring material behaviour. This has left the investigation of its microstructural behaviour largely unexplored, under this deformation mode.

2.5 Modelling NiTi Shape Memory Alloy

One of the main objectives of this research is to utilise a model to accurately simulate the non-linear behaviour of SMAs. The constitutive modelling of SMAs is necessary for a variety of purposes (Khandaval [86]). In particular, they:

1. Explain observed phenomena: by understanding the underlying physics and mechanisms that cause the observed

effects

2. Aid material development: by identifying the material properties or processing parameters that can yield the desired effects in terms of the material's five main characteristics (As listed on section 2.2).

3. Aid application development: by predicting the material response in conjunction with a smart device or the system under investigation.

This chapter is dedicated to the identification of a SMA model that best addresses the requirements presented in this research. The chapter is structured as follows. Sections 2.5.1 and 2.5.2 are an evaluation of current ecology of constitutive modelling approaches and narrates the path undertaken to narrow down the selection to the most suitable for this study.

2.5.1 Modelling approaches Part 1: Scales of continuum

The implementation of constitutive models for SMAs have been challenging due to the highly non-linear, history dependent, thermomechanical behaviour of SMAs. This section is dedicated to the review of the main constitutive models that have been developed to successfully map SMAs. Such reviews have been

previously conducted by Birman [87], Bernardini and Pence [88] and Paiva and Savi [89], Smith [90] and Lagoudas [91] Khandeval [86] and Arghavani [92].

Fuelled by the increasing number of applications, this area of constitutive modelling has been a topic of many research publications and has seen significant developments in the past four decades. In spite of this, there is yet to be a model accounting for all five of the aforementioned phenomena of SMAs- giving plenty of scope for further advancements. The majority of the resulting constitutive models reported in literature can be formally classified into these three major categories by scale of the continuum:

1. Macro: Macroscopic phenomenological models
2. Micro-macro: Micro mechanics based macroscopic models,
3. Micro: Microscopic thermodynamics models.

The section below evaluates these categories of models, relating their suitability for our application.

2.5.1.1 Macroscopic phenomenological models *(macro-models)*

Macro models use macroscopic variables to describe average material behaviour. They are built on phenomenological

thermodynamics and/or directly curve fitting experimental data. As a result they can only describe the global mechanical response while details on a microstructural level are ignored. These kinds of models are generally more suitable for engineering applications as a result of their simplicity and fast computations – effective behaviour can be simulated efficiently with numerical methods such as FEM [86]). Table 2.1 summarises Macro Models developed for SMAs in chronological order.

Table 2.1: Summary of phenomenological models developed for Shape Memory Alloys

Model	Year	Description
Leclercq & Lexcellent	1996	Modelling of detwinned and self-accommodated martensite utilising two internal variables
Auricchio & Sacco	1997	One-Dimensional Model for Superelastic Shape Memory Alloys with Different Elastic Properties Between austenite and martensite
Auricchio & Taylor	1997	Modelling of finite strain Superelastic behaviour
Auricchio, Taylor & Lubliner	1997	Macromodelling of the Superelastic behaviour
Bekker & Brinson	1997	Temperature-induced phase transformation in a shape memory alloy:

		phase diagram based kinetics approach
Raniecki & Lexcellent	1998	Thermodynamics of isotropic pseudoelasticity in shape memory alloys
Souza, Mamiya & Zouain	1998	Three dimensional model for solids undergoing stress-induced phase transformations
Brocca, Brinson & Bazant	2002	Three-dimensional constitutive model for shape memory alloys based on microplane model
Helm & Haupt	2003	Phenomenological model for the multiaxial material behaviour of shape memory alloys
Auricchio, Marfia & Sacco	2003	Modelling of SMA materials: training and two-way memory effects.
Bouvet, Calloch & Lexcellent	2004	Phenomenological model for pseudoelasticity of shape memory alloys under multiaxial proportional and non-proportional loadings
Lagoudas & Entchev	2004	Constitutive Modelling of Transformation-induced Plasticity and its Effect on the Behaviour of Porous Shape Memory Alloys
Muller & Bruhns	2006	Thermodynamic finite-strain model for pseudoelastic shape memory alloys
Auricchio, Reali & Stefanelli	2007	Three-dimensional model describing stress-induced solid phase transformation with permanent inelasticity
Panico & Brinson	2007	Three-dimensional phenomenological model for martensite reorientation in shape memory alloys

Popov & Lagoudas	2007	Three-dimensional Constitutive Model for Shape Memory Alloys Incorporating Pseudoelasticity and Detwinning of Self-Accommodated martensite
Thiebaud, Collet, Foltete & Lexcellent	2007	Multi-axial pseudoelastic model to predict the dynamic behaviour of shape memory alloys
Reese & Christ	2008	Thermomechanically coupled modelling of shape memory alloys in the framework of large strains
Moumni, Zaki & Nguyen	2008	Theoretical and numerical modelling of solid-solid phase change of shape memory alloys
Christ & Reese	2009	Finite element model for shape memory alloys considering thermomechanical couplings at large strains

2.5.1.2 Micro-mechanics based macroscopic models *(micro-macro models)*

Micro-macro models combine macroscopic continuum mechanics and micromechanics to derive constitutive laws of the material. SMA response is derived through the crystallographic modelling of a single grain, which is averaged over a representative volume element (RVE). A major strength of this modelling approach is the ability to predict the material response using only the crystallographical parameters. This provides a valuable insight on

the phase transformation on the crystal level, successfully reproducing reorientation and de-twinning of martensite variants. The downside to this approach is in the large number of internal variables utilised which necessitate a large number of numerical computations. This computer intensive process renders models of this approach difficult to implement for engineering purposes. Table 2.2 summarises Micro Macro Models developed for SMAs in chronological order.

Table 2.2: Summary of micro-mechanics based macroscopic models developed for Shape Memory Alloys

Model	Year	Description
Fischer & Tanaka	1992	Micromechanical Model for the Kinetics of martensitic Transformation
Sun & Hwang	1993	Micromechanics modelling for the constitutive behaviour of polycrystalline shape memory alloys
Sun, Lexcellent & Goo	1996	Micromechanics modelling of reorientation process of single-crystal shape memory alloys
Huang & Brinson	1998	Multi-variant model for single crystal shape memory alloy behaviour
Govindjee & Miehe	2001	Multi-Variant martensitic Phase Transformation Model
Thamburaja & Anand	2002	Superelastic model for tension-torsion of Ti-Ni shape-memory alloy

Thamburaja	2005	Constitutive model for martensitic reorientation and de-twinning in shape-memory alloys
Patoor, Lagoudas, Entchev, Brinson & Gao	2006	Micromechanical modelling of Polycrystallne SMAs- Averaging Micromechanics methods based on the self-consistant approximation
Pan, Thamburaja & Chau	2007	Multi-axial modelling of shape-memory alloys undergoing martensitic reorientation and de-twinning
Thamburaja, Pan & Chau	2009	Evolution of microstructure during twinning: constitutive equations

2.5.1.3 Microscopic thermodynamics models *(micro models)*

Micro models focus on microstructural features such as nucleation, interface motion and twin growth. These models interpret phase volume fractions as a consequence of interface movements instead of directly employing them as internal variables. Micro models can be particularly effective for explaining fundamental phenomena occurring at a microscopic level. However, this consequences in an approach that is not easily applicable at a structural/device scale, making them unsuitable for most engineering applications. Table 2.3 summarises Micro Macro Models developed for SMAs in chronological order.

Table 2.3: Summary of Micro-mechanics based macroscopic models developed for Shape Memory Alloys

Model	Year	Description
Ball & James	1987	Micromechanical model using Fine Phase Mixtures as Minimizers of Energy
Abeyaratne & Knowles	1990	Continuum mechanical model for solid-solid phase transitions
Levitas & Stein	1997	Simple Micromechanical Model of Thermoelastic martensitic Transformations
Bhattacharya	2003	SMA material modelling- Microstructure of martensite
Idesman, Levitas, Preston & Cho	2005	Finite element simulations of martensitic phase transitions and microstructures based on a strain-softening model
Levitas & Ozsoy	2009	Micromechanical modeling of stress-induced phase transformations

2.5.2 Modelling approaches Part 2: Phenomenological constitutive models

The above review details how each of the modelling approaches aim to describe SMA behaviour from differing viewpoints and continuum scales. However, Humbeek and Cederstrom, 1994 [105] observe "... in spite of all these efforts and qualitatively very interesting results, no single model exists that is able to describe

quantitatively the shape memory performance of a real material. The reason for this is related to the very strong influence of micro-structure and processing on the mechanical properties described in the (σ, ε, T) space."

From an engineering application point of view, the most practical and productive approach is to employ a model, which produces the macroscopic global response without attempting to capture detailed underlying thermomechanical behaviour. Such models are innately frugal on computational resources whilst at the same time being capable of processing complex 3-dimensional problems. To fully understand the unique response of SMAs from a theoretical point of view, however, micro and micro-macro models that take into account the micro structural change that occurs during phase transformation are necessitated.

In this work, a phenomenological modelling approach is selected. This choice was persuaded by two major factors. Firstly, there is a wealth of literature concerning macro approaches with the inclusion of an extensive volume of models. Secondly, as this research would eventually lead to the modelling of complex structures under magnitude of variables; the inclusion of micromechanical phenomena would result in an overcomplicated model.

Macroscopic phenomenological modelling can be further categorised as depicted in Figure 2,27 (This classification has been adopted from Arghavani, [92]). The following section is dedicated to the review of the various streams of this modelling approach.

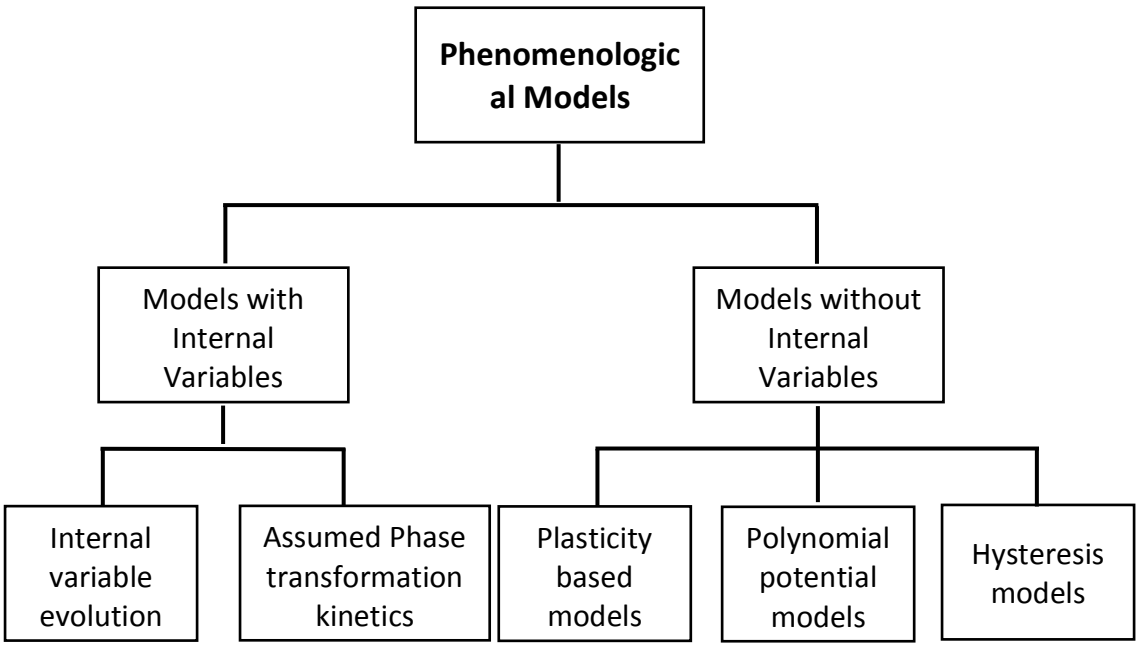

Figure 2.27: *Ecosystem of phenomenological constitutive models (Adopted from Arghavani [92])*

2.5.2.1 Models without Internal Variables

Material behaviour is described by strain, stress, temperature and entropy, whilst quantities representing phase mixture are not introduced in this modelling approach. Models of this type can be further categorised as (1) Hysteresis models, (2) Polynomial potential models and (3) Plasticity based models.

2.5.2.1.1 Hysteresis models

Models of this category seek to replicate experimentally observed

curves that encompass high nonlinearity and complex looping. Their underlying constitutive equations are proposed directly on the basis of mathematical properties, often without a clear focus on their relationship with fundamental physical phenomena. This modelling approach boasts a superior reliability and robustness that favourably match experiments, whilst encompassing the ability to treat complex driving. In the context of simulating SMA response through hysteresis models, two main algorithm classes exist.

In the first approach, sub-domain conversion/reversion is tracked to obtain integral based algorithms. The Preisach algorithm is the most prevalent of first class algorithms. This was employed to describe uniaxial isothermal pseudoelastic stress–strain SMA response (Huo [106]; Ortin [107]). Limitations of this approach have been pointed out by Bekker and Brinson [108], who argue that the Preisach model is unable to represent dead zones of transformation or drift of hysteresis loops with cyclic loading during partial transformation. Moreover, this approach necessitates the calculation of a weighting function for every point in the hysteresis region, leading to an overly intensive computational process.

The second algorithm class is built on the fundamentals of differential equations with separate forms for driving input increase/decrease. An example of this category, the Duhem-Madelung form differential equations, allow reproducing phase fraction sub- loops for temperature histories. Likhacev and Koval

[109] and Ivshin and Pence [110] use this approach to model the SMA phase fraction evolution during thermally induced transformation. A drawback of this method is in the relaying of the fading influence of the initial phase fraction towards subsequent shakedown behaviour. Exposing this algorithm to sustained thermal cycles consequence in the sub-loops collapsing onto a final limiting sub-loop.

2.5.2.1.2 Polynomial potential models

Models of this approach are based on constitutive equations for stress/strain and entropy which are acquired through the partial derivatives of the polynomial free energy function. The polynomial potential model was initially proposed by Falk in 1980 [111] and subsequent models by Falk [112] and Falk and Konopka [113] can be categorised as models in this group.

Polynomial potential models are based on the Devonshire theory for temperature induced first order phase transition combined with hysteresis. They produce non-monotone stress-strain curves and interpret unstable negative gradients as events of phase transformation. The response tracked during such transitions are assumed to occur over a constant stress. Moreover, the Landau-Devonshire free energy accounts for the temperature dependence of isothermal stress–strain behaviour in SMAs.

The key strength of the polynomial potential modelling approach lies in its underlying simplicity. As a consequence, however, they

are incapable of simulating complex material response or at describing the evolutive nature of the processes accurately. Muller and Xu [114] describe these models as a "one-dimensional model that defines a polynomial free energy which describes pseudoelasticity and shape memory in a very simple way".

2.5.2.1.3 Plasticity models

Plasticity models aim to describe constitutive response employing the well-established principles of the theory of elastoplasticity. This modelling approach was first adapted to describe SMA behaviour by Bertran in 1982 [115] using kinematics and isotropic hardening concepts. Subsequent efforts based on fundamental plasticity concepts lead to models capable of simulating both Superelastic and Shape Memory effects. Models presented by Maimiya and co-workers in 1995 [116], Souza and co-workers in 1998 [117] and Motta and co-workers in 1999 [118] all fall into this category. A one-dimensional model proposed by Auricchio and co-workers, capable of describing these SMA specific phenomena (Auricchio and Lubliner , 1997 [119]), was later extended to a three-dimensional context (Auricchio et al. 1997 [94]; Auricchio and Sacco, 1997 [120]). Brandon and co-workers (Brandon et al 1992 [121]) model accounts for both plastic and elastic forms within the hysteresis loop based on Muller and Xu's experimental study of single crystal SMA. This approach captures a wider range of physical phenomena compared to traditional plasticity theory. It

calculates elastic-plastic phase transformation through a dependence on the time history of the strain and phase fractions. The model is particularly suitable for single crystal SMA applications to yield a smooth elastic-plastic mode transition process. Other models of note that employ plasticity concepts include models proposed by Govindjee and Kasper in 1997 [122] and Leclercq and co-workers in 1995 [123].

2.5.2.2 Models with internal variables

In this approach, internal variables in the form of phase fractions and/or macroscopic transformation strains are employed to describe material structure. The internal variables are paired with mechanical control variables (stress/strain) and thermodynamic control variables (temperature/entropy) to form an array of state variables. The subsequent use of a general thermodynamic consistent approach allows derivation of evolution equations for these state variables. Models based on this approach can be further categorized into two groups: (1) Models with assumed phase transformation kinetics and (2) Models with internal variable evolution equation.

2.5.2.2.1 Models with assumed phase transformation kinetics

Models of this category utilise the martensitic volumetric function

– determined through the current values of stress and temperature – as an internal variable. This formulation has been adopted in some of the most prominent SMA concentrated modelling efforts, with numerous functions been proposed to express the volumetric fraction evolution.

Research lead by Tanaka can be credited for the pioneering work in this stream of SMA modelling (Tanaka & Nagaki, 1982 [124]; Tanaka, 1986 [125]; Tanaka & Hayashi, 1992 [126]; Tanaka & Nishimura, 1994 [127]; Tanaka & Nishimura, 1995 [128]). Their proposed model was initially conceptualised to process three-dimensional problems involving SMAs, however, its implementation was restricted to a one-dimensional context. The resulting model utilises exponential functions to calculate phase transformations – thus necessitating extra consideration towards the phase transformation final bounds. This original model was subsequently expanded to a three-dimensional context by Boyd and Lagoudas [129] using the same framework describing phase transformation evolution.

The model proposed by Brinson in 1993 [130] adopts an alternative approach to the phase transformation kinetics. The evolution law based on the cosine function employs different elastic moduli for austenite and martensite states. A novel feature of this model is the differentiation between twinned and de-twinned martensite, obtained by splitting the martensite fraction as temperature-induced or stress-induced martensite. Liang & Rogers [131] also utilise the cosine function in their proposed three-dimensional

model, based on the principles of associated distortion energy driving phase transformations in SMAs.

2.5.2.2.2 Models with internal variable evolution equation

Models fitting into this basic framework are characterised by their more intensive thermo-dynamical approach. The accompanying physical laws are composed of the constitutive equations that describe the material features and the material behaviour requirements that enforce thermo-dynamical process restrictions. These models specify the underlying constitutive information through (1) *State laws* for the entities conjugate to their control variables, and (2) *Kinetic laws* for the internal variables.

The State laws are either formulated directly or obtained as partial derivatives of the appropriate free energy function by imposing the Clausius-Duhem inequality for each process. A Fourier equation, which relates temperature gradient and heat flux is generally implemented if heat conduction is incorporated. The kinetic laws generally rely on the phase fraction history of the material to describe phase transformation hysteresis. The typical convention is to specify this dependence through equations that link the rates of the internal variables to the current state and its time derivatives. The resulting solution of differential equations in time presents the internal state.

Historically, models proposed utilising this framework have been

constrained to a one-dimensional context. However, in the last decade, fuelled by available experimental data and ever-increasing engineering applications, attention has shifted towards developing three-dimensional constitutive models. Collectively, the current group of three-dimensional phenomenological models capture a wide array of SMA phenomena, including [92]:

- Asymmetric behaviour under tension-compression
- Different material behaviour in high and low temperature
- Finite deformations and nonlinear geometric effects
- Permanent transformation-induced plastic strains in cyclic loadings
- Phase dependent mechanical properties
- Plasticity due to dislocation motions
- Sub loops and return point memory effect
- Thermo-mechanical coupled and pseudo-rate dependent behaviour
- Variant reorientation under non-proportional loadings

This approach suffers from a lack of numerical implementation, especially in comparison to the corresponding efforts made in constitutive modelling. This can be in part attributed to the general unavailability of constitutive models with a suitable form for numerical implementation. The complicated structure of these models - compared to plasticity models – coupled with the materials inherent high non-linearity form further obstacles to its numerical implementation.

2.6 Implications of literature review on study

1. There are clear benefits in implementing a NiTi SMA solid-state actuator to replace the dated pneumatic based variable stator vane system. This proposed system could have the capability to cater for a much larger operating condition requirement.

2. SMA studies are heavily skewed towards the study of SMA primarily in the pseudoelastic form due to the demand in applications in the biomedical field. The study of actuation response on the other hand necessitates analysis of both austenite and martensite phases along with phase transformational behaviour. The introduction of temperature control is necessary to enable such a study.

3. The flexural deformation mode combines both compressive and tensile strains. As NiTi SMAs have reported asymmetry between compression and tension, the flexural response is highly nonlinear and complex. The study of SMA flexural deformation has been limited to several studies, and a comprehensive analysis on NiTi plate has not yet been undertaken. Such a study could have implications towards the scientific knowledge of SMA response, and the operation of SMA as an actuator.

4. In-situ studies have explored material behaviour in either austenite or martensite phases due to the difficulty in integrating temperature control and in-situ simultaneously. This has limited these studies to the study of stress-induced transformation only. The introduction of temperature control would allow both regimes

to be analysed simultaneously and enable the study of temperature-induced transformation.

5. The most suitable model approach to replicate SMA behaviour for this application is one that is based on generalised plasticity theory capable of simulating both pseudoelasticity and Shape Memory Effects. Plasticity models are inherently efficient with computational resources, a paramount consideration in the modelling of complex SMA forms.

CHAPTER 3
EXPERIMENTAL METHODS

3.1 Introduction

Inspired by the above stream of research, the present study aims to characterise the coupled thermomechanical response of NiTi SMA plate in the flexural deformation mode. Four-point bend tests are employed as the base for conducting this study. What distinguishes this research is the analysis of both thermal and stress induced transformation behaviour of NiTi in plate form. Additionally, in-situ techniques allows simultaneous observation at a granular level. The inclusion of these different aspects, however, presents the study with a new series of challenges.

This experimental study forms an integral step to the design of a NiTi SMA actuator exploiting the flexural deformation mode. Data collected from the tests would stream into the subsequent studies that are dedicated to FEM simulation of the material and actuator response.

The body of the experimental investigation is arranged into two

chapters. The methodology and experimental techniques that have been utilised in the study are detailed in in Chapter 3 - Please note that some parts of this methodology have been previously presented by the author [76]. The consequent results, findings and contributions generated by the study are presented in Chapter 4.

3.2 Testing Stage

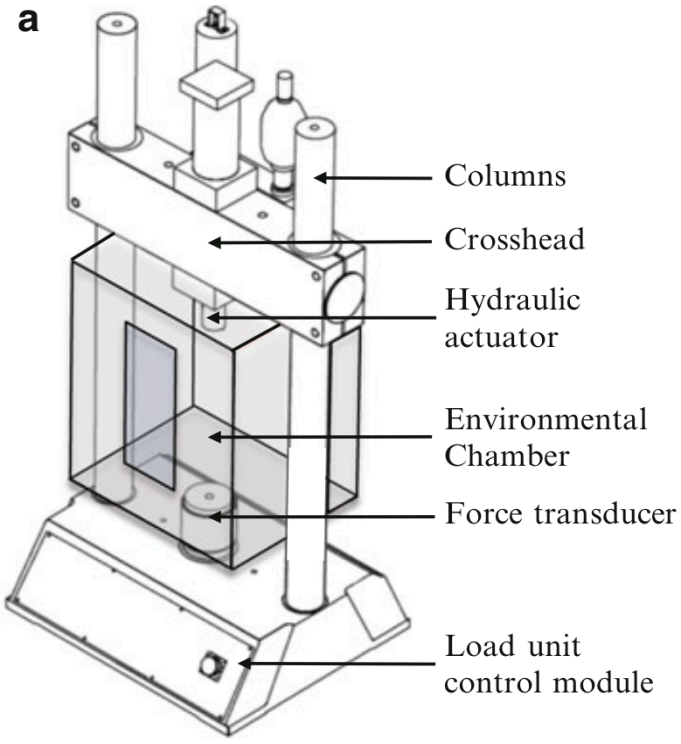

Figure 3.1: *Testing stage: MTS 858 servo-hydraulic test system, Thermcraft LB-series Box Laboratory*

Figure 3.1 illustrates the general set up. The load frame - a Tabletop MTS 858 servo-hydraulic test system - uses a cross-head assembly, which includes a single moving upper grip, a stationary lower grip and a LVDT position sensor with an accuracy of ±2.5 x 10^{-5}m. The loads are measured through a load cell with an accuracy of 0.0227N. The system is designed to function in a closed-loop configuration under computer control. The specimen sits within a temperature controlled environmental chamber - a Thermcraft LB-series Box Laboratory oven.

A custom four-point bend fixture is built and integrated into the uniaxial load frame to perform the flexural tests, as depicted in Figure 3.2. The external and internal supports are inverted to limit the deflection of the optically investigated central section of the specimen. The fixture is designed with adequate spatial clearances in mind, allowing upper support deflection of up to 12.5 mm (equivalent to a 4 % strain at the outer fibre with the specimens used).

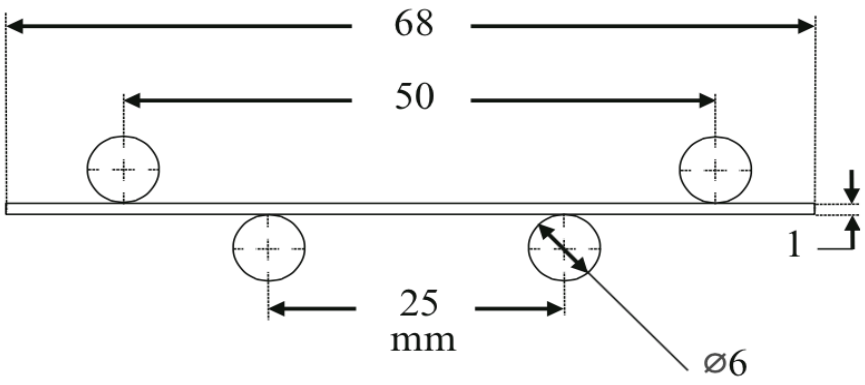

Figure 3.2: *Custom four-point bend fixture*

The distance between the supporting pins coupled with the vertical displacement at the centre of the plate is used in the calculation of the global flexural stresses, strains and modulus. The equations followed to obtain these values are:

Calculation of the flexural stress σ_f

$$\sigma_f = \frac{3FL}{2bd^2} \quad (3.1)$$

where, σ_f is the stress in outer fibres at midpoint (MPa), F is the load at a given point on the load deflection curve (N), L is the support span between the outer pins (50mm), b is the width of the NiTi plate (8mm), and d is the thickness of the NiTi plate (1mm).

Calculation of the flexural strain $\in_f$

$$\varepsilon_f = \frac{6dl^2}{8RL^2} \quad (3.2)$$

where ε_f is the strain at the outer surface (mm/mm), l is the support span between the inner pins (25mm), and R is the radius of curvature of the NiTi plate (mm).

Calculation of the flexural modulus E_f

$$E_f = \frac{L^3m}{4bd^3} \quad (3.3)$$

where E_f is the flexural modulus of elasticity (MPa), and m is the

gradient of the elastic portion of the load deflection.

3.3 Optical microscopy

A single-camera setup is used to observe changes in the surface transformation characteristics at a macroscopic and fine-scale microstructural level as a function of loading parameters. The camera used is a 12.76 mega pixel IP-58 rated Panasonic HX-A500 (as depicted in Figure 3.3) with a custom wide-angled macro lens installed and paired with a 1000X magnification lens.

The camera and lens combination were primarily chosen for their compactness – as space inside the environmental chamber was restricted. The split camera/operation module design was valuable as it allowed in-situ remote operation of the camera system whilst inside the environmental chamber. Although this study did not necessitate, as the experimental temperatures fell within the operational temperatures of the camera, a liquid cooled enclosure could have been commissioned to isolate the waterproof camera console from ambient temperature.

This setup is capable of taking stills at 5376x3024 pixels and video at resolutions of 3840x2160 at 30FPS, 1920x1080 at 60FPS, 1280x720 at 120FPS and 840x480 at 240FPS. The wide angled lens provides a adjustable field of view of 44^{o} or 30^{o}. The minimum focused area is approximately 0.55mmx1mm (height x width), giving a theoretical pixel dimension of 0.2 microns at 4k video capture (3840x2160). An LED based illumination setup, with a

lower heat emission output is employed due to the elevated temperature sensitivity of the tests.

Figure 3.3: *Panasonic Hx-A500 used for in-situ optical observation*

Digital Image Correlation (DIC) is employed to obtain local strain measurement without the need to rely solely on grip displacements. DIC starts with a reference image and followed by subsequent images recorded during the deformation process. A strain distribution map is created by calculating the correlation between the reference and deformed patterns. While traditional DIC methods comprise the creation of a unique pattern through etching or application of a high contrast media onto the specimen, this study substitutes this by using the fine granular detail and scratches on the specimen as its pattern.

The microstructural changes are observed from the finely polished surface of the specimen. A higher detection sensitivity of fine topological details is achieved through the use of a circular polarizing filter - this increases colour saturation and reduce reflections. A matte black painted aluminium back plate sits behind the specimen to further reduce any reflections. A maximum

zoom, which focuses on a surface area approximately 500µm², is utilised to investigate observation of the material at a variant level. This allows the simultaneous viewing of both compressive and tensile deformation modes. All images are taken during static holds of constant temperature and strain. Figure 3.4 depicts the field of view the four-point bend study optically investigates.

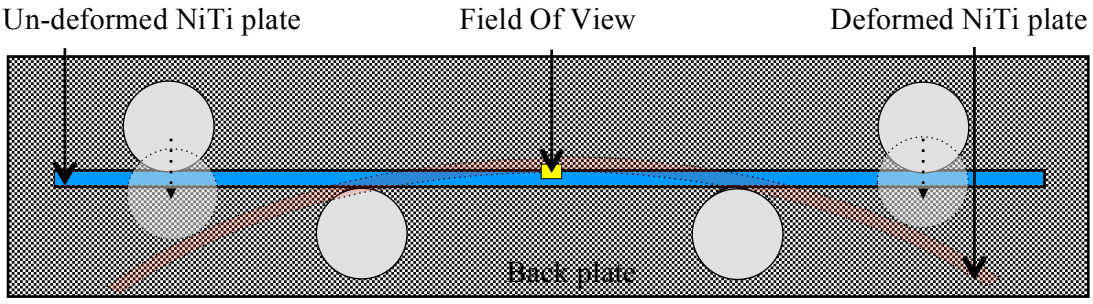

Figure 3.4: *Optically investigated area through in the in-situ study*

3.4 Specimen Preparation

Proper specimen preparation is a very important aspect of any NiTi SMA study. Traditionally, such measures are undertaken to stabilise the complex response of the material, but due to the added requirement of light optical observation, the importance on specimen preparation is amplified. The steps undertaken to realise this are described below.

3.4.1 Machining

Near-equiatomic 1 mm thick NiTi plate was obtained from Memry Metalle GmbH with manufacturer specified austenite finish (A_f) temperature of 65^0C. The plate is machined to dimensions of 66 mm x 8 mm using a wire cut electrical discharge machining process. This minimizes heat distortion and cold work induced on the cutting surface. As the tests optically investigate the specimen's surface and relate it to the material behaviour as a whole, the homogeneity over their behaviours is important. A schematic of the EDM process is depicted in Figure 3.5.

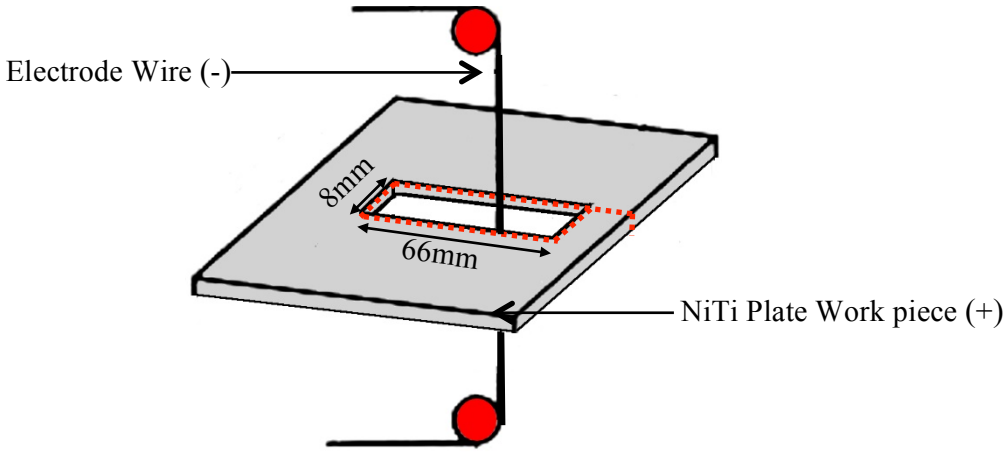

Figure 3.5: *Wire Cut EDM process employed for machining NiTi specimens*

3.4.2 Thermal conditioning

Thermomechanical treatment is one of the most effective methods adopted for manipulating the transformation properties of NiTi

SMA. It is particular useful for applications where cyclic consistency is important, as the stability of phase transformation has been found to depend upon the thermomechanical treatments, such as heat-treatment and thermal cycling. The thermal conditioning procedure implemented in this study is detailed below.

The specimens are heat treated in an oven at 450°C for 1 hour followed by water quench. This annealing condition ensures a large grain size – at this temperature the amorphous bands start to crystallize without completely annealing the structural defects in the material, as crystallite nucleation is suppressed [77]. This step is essential for the material to recover from any previous cold work or damage it has sustained and to stabilize transformation characteristics [77].

The specimens are thermally cycled through martensite and austenite phases using a water bath. Miyazaki et al. [78] indicate that M_f and M_s temperatures decrease with increasing number of thermal cycles. The decrease is rapid at first but more gradual with increasing cycles as values stabilize. Their TEM observations reveal the introduction of dislocations from the first thermal cycle onwards, which act as obstacles to dislocation movement and stabilises behaviour through further thermal cycles. However, their thermal cycling had also shown to activate R-Phase transformation in NiTi SMAs that had a previously suppressed R-Phase. In this study, the specimens are subjected to 30 thermal cycles despite possible R-Phase activation, as it is paramount to obtain stable and repeatable transformation characteristics

throughout.

3.4.3 Micro preparation

The thermally prepared specimens are then subjected to several steps of grinding and polishing using the Bueler Automet 250, to allow observation of variant microstructure at the specimen surface. The specimens are attached to a piece of bakelite in preparation for the subsequent grinding and polishing steps. Dimensional constraints necessitated manual hand polishing as the specimens could not be mounted onto the polishing. The multi-step process commences using coarse P800 and then P1200 abrasive discs to grind all sides of the initially rough specimen surface. The observational side of the specimen is then sequentially polished using 3µm MetaDi Supreme Diamond abrasive for coarse polishing and then finally using 0.02–0.06µm MasterMet Silica for fine polishing. Routine examinations after each grinding/polishing cycle using a light optical microscope ensured each step was executed properly – essential due to the manual hand polishing technique employed.

3.5 Specimen Characterisation

Differential Scanning Calorimetry (DSC) is used to identify phase transformation temperatures of the NiTi plates. This is a thermo analytical method commonly used in NiTi SMA studies that determines absolute phase transformation temperatures. It

measures the difference between the amount of heat required to increase the temperature of a sample and reference, as a function of temperature. The phase transformations are captured as a result of the large amounts of heat absorbed (or emitted) during this process, with a relatively small change in temperature.

The DSC tests adopt a temperature profile of 15°C to 100°C with a constant scanning rate of 10 K/min. This is considered the most efficient temperature rate to measure the intrinsic transition quantities and also a common value within published literature. This heating rate represents a quasi-static value, and is preferable to higher heating rates that struggle to maintain a constant temperature throughout the sample and produce inconsistent results. Characterisation of the transformation temperatures is essential in establishing temperature ranges for the experimental study.

NiTi plate specimens in the following conditions are presented: (1) as received, (2) annealed, and (3) thermally cycled. For DSC scanning, $1mm^3$ samples from these specimens are fabricated through wire cut electrical discharge machining process. This minimises disparity of behaviour between the sample and specimen, which would otherwise occur due to heat distortion and cold work.

The DSC thermograms of each of these aforementioned states under heating (M → A) and cooling (A → M) are overlaid and depicted in Figure 3.6 and Figure 3.7 respectively. The corresponding

transformation temperatures that have been determined through the intersections of a base line and the tangents to a thermal peak from the thermograms are recorded in Table 3.1. The hysteresis is calculated by finding the difference between the average forward and reverse transformation temperatures.

The thermograms from the "As received" specimens (grey) reveal shallow and strongly flattened endothermic and exothermic peaks making it very difficult to determine the transformation temperatures with any accuracy. However, it is evident that a wide temperature band is present for both forward and reverse transformations. Certain previous studies have suggested that cold worked NiTi, without training, can be observed to be shape memory effect "dead" as they exhibit no phase transformations. This suggests that these pre-annealed specimens may have had a minor degree of thermo mechanical cycling imposed before the DSC tests were undertaken. A possible hypothesis is that the heat distortion induced onto the cutting surface during machining might have activated phase transformations.

After annealing, the material assumes a very different characteristic, as the differences between M_s/M_f and A_s/Af shrink markedly. Moreover, the temperatures recorded at the onset of forward transformation (Ms) and completion of reverse transformation (Af) reduces significantly in comparison to the "as received" specimen. The narrow single-stage endothermic and exothermic phase transformation bands are accompanied by sharp peaks - particularly evident during forward transformation (A→M). These observations fall in line with common understanding of

microstructural changes under annealing. Ni-rich precipitates are formed during the heat treatment, which alters the Ni-Ti ratio in the specimen. This small change in NiTi composition results in the change in phase transformation temperatures.

Calorimetric observation of the thermally cycled specimen indicates similar transformation temperatures and behaviour to the annealed specimen. One notable exception is the exaggerated peak observed during reverse transformation – indicating a higher latent heat. According to Brailovski [79], this increase is attributed to the increase of the austenite ←→ martensite phase transformation reversibility.

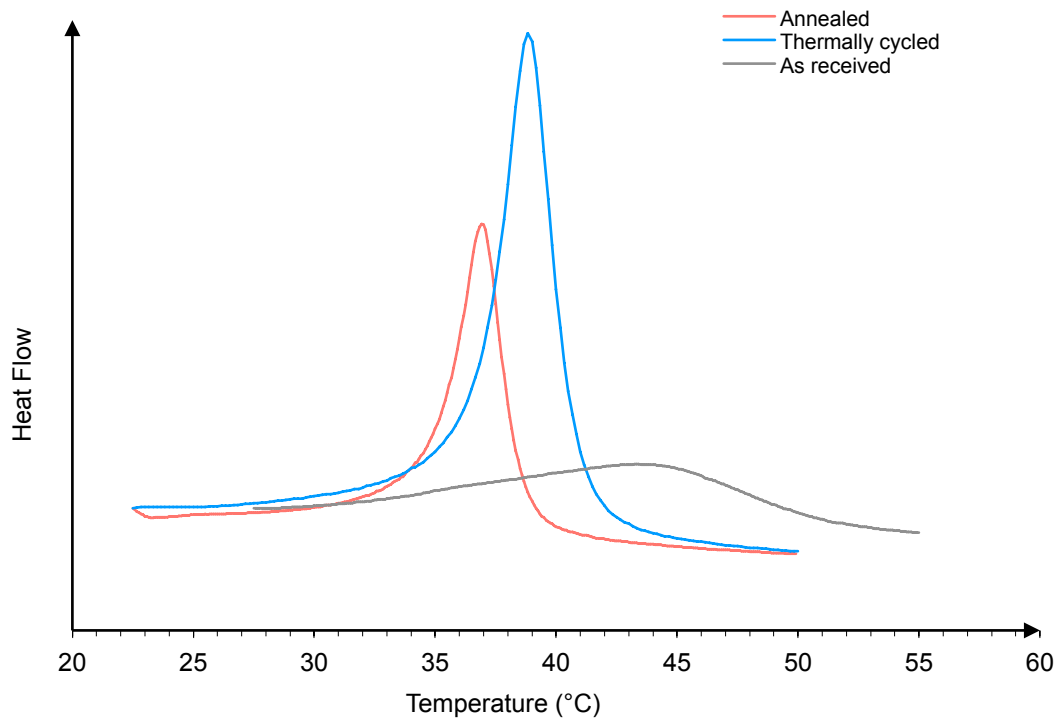

Figure 3.6: *DSC Thermogram for heating (M→A)*

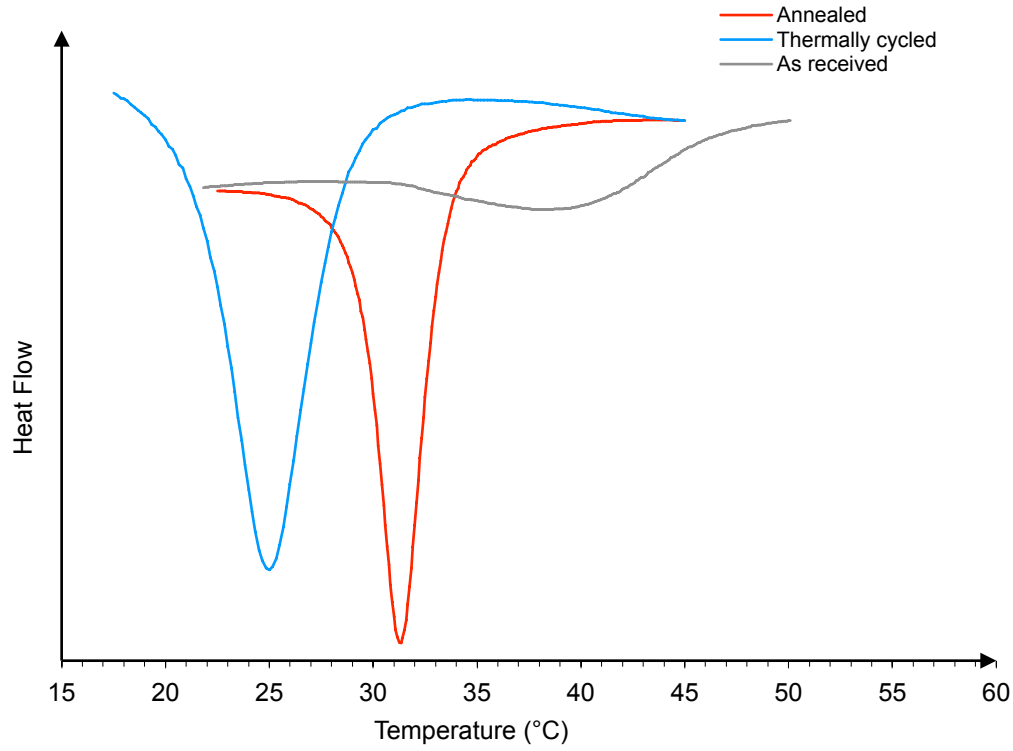

Figure 3.7: *DSC Thermogram for cooling (A→M)*

Table 3.1: *Phase transformation temperatures determined from the DSC Thermograms*

Specimen	M_S (°C)	M_f (°C)	$M_S \rightarrow M_f$ (°C)	A_S (°C)	A_f (°C)	$A_s \rightarrow A_f$ (°C)	Hysteresis (°C)
As received	47.8	30.7	17.1	28.5	50.9	22.4	0.45
Annealed	34.9	30.6	4.3	33.1	37.4	4.3	4.3
Thermally cycled	35.6	31.3	4.3	33.5	38.2	4.7	4.7

3.6 Test overview

The experimental test study can be subcategorized into three sections: (1) constant temperature strain sweep tests, (2) constant strain tests with temperature increments and (3) thermomechanical cycling tests. The tests employ a temperature range between A_f-10°C→A_f+10°C (28.2°C→48.2°C) and a peak global flexural strain of 1%. Using these load parameters, the study performs a comprehensive evaluation of the material behaviour within the operating envelope of the planned NiTi SMA actuator.

The extremities of these parameters are established due to the requirement of the maximum strain falling within the de-twinning phase at the lowest temperature, A_f-10°C. However, it must be noted that due to the non-linear response of the material, localised strains could be considerably more, especially during the de-twinning phase where large heterogeneities can exist between grain boundaries. An adequate safety margin is thus kept from the end of the strain plateau observed from previous data from tensile tests on this material: ~4 % at room temperature. This strain magnitude range ensures that thermo-mechanical cycling effects are minimised and life span of each specimen is improved. Furthermore, the lower strains reflect the behaviour of a high cycle element such as the variable stator vane where uniformity of performance must be established throughout the life cycle.

Three NiTi plate specimens are used in this study. The thermal and fatigue history of each of the specimens is recorded and carefully balanced to enhance comparability between results. In

each of the constant strain tests, the temperature loading is temporarily paused at planned intervals, while photographs are taken of the observational surface.

3.7 Reliability and validity of acquired data

Several measures were taken to optimize the reliability and validity of the data.

(I) Each analysis adopted a very high data capture rate. A macro programme is then used to condense the results by finding the average between a set of data points. This allowed to diminish erroneous data points and to improve overall validity of the data.

(II) The MTS 858 servo-hydraulic test system is subjected to annual calibration checks of temperature and force by MTS personnel. The results were obtained immediately after such a calibration was performed.

(III) After each test, the specimen was placed inside a temperature oven and heated past the A_f temperature. This ensured that the specimen was restored to its original condition and formation of stress-induced martensite was reversed.

(IV) Different heating/cooling rates were experimented to evaluate their effects, i.e. if the cooling rate was too high, the specimen would not cool down quickly enough.

(V) A procedure to run the tests was introduced. This optimized uniformity, which in turn, improved the quality of the results obtained.

CHAPTER 4
EXPERIMENTAL FINDINGS

4.1 Introduction

This chapter presents the findings and contributions brought by the experimental study. The results are subcategorised into the main types of investigations conducted, namely; cyclic tests that observe material response upon mechanical and thermal cycling (Section 4.2), Constant Strain Temperature sweep Tests that evaluate the effects that strain variation has on the material response as it is subjected to a thermal load cycle (Section 4.3), Constant Temperature Strain sweep tests that evaluate the effects temperature change has on the material response as it is subjected to a mechanical load cycle (Section 4.4) and finally microscopic strain field analysis using in-situ DIC (Section 4.5). Observed parameters include time, temperature, deflection and load from the MTS test-system. The primary objective of this chapter is to identify material parameters for the subsequent computational study. SMA behaviour is examined at both a macroscopic level

and granular level through in-situ observation.

4.2 Thermo-mechanical cycling

Implementation of radically new technology in the civil aerospace sector stipulates exhaustive checks to satisfy the required technology readiness level. One major consideration in such measures is to ensure consistency of component operation and performance over a prescribed operational period. In applications that require such cyclic consistency, widespread utilisation of SMAs has not occurred due to perceived instabilities during thermal and mechanical cycling. In the case of NiTi SMAs, these instabilities manifest as changes in its thermo-mechanical response. This can lead to the accumulation of irrecoverable strain, changes in transformation temperatures, transformation strains and transformation hysteresis [2]. The objective of this study is to map the macroscopic response of NiTi plate specimens over a specified thermo-mechanical load cycle. It is designed to acquire the operation parameters for the proposed SMA actuator in a bid to minimise thermo-cycling effects.

The four-point flexural study is performed without any temperature control: the ambient temperature ranged from 21^0C to 23^0C. As a result, this study is constrained to the evaluation of the response at a martensitic phase. The specimens are mechanically deformed

isothermally to strains between 0→2% in strain control at a rate of $10^{-3}s^{-1}$. At the completion of each mechanical cycle the specimens are heated past the A_f temperature to recover any retained deformation. An identical testing procedure is applied on (1) As-received and (2) Annealed NiTi plate specimens, permitting a direct comparison between the two states and the impact of the thermal conditioning.

Table 4.1 indicates the experimental parameters. The macroscopic isothermal stress-strain response obtained through this thermo-mechanical loading cycle is presented in Figure 4.1 for the as-received and Figure 4.3 for annealed specimen condition. The corresponding data tracking the change in the global tangent modulus as a function of strain is presented in Figure 4.2 and Figure 4.4 respectively.

Table 4.1: *Experimental test conditions for specimens subjected to thermo-mechanical cycling*

Strain Min/Max	Strain rate	Temperature Min/Max	Total tests
0.1% → 2% (20 steps)	1 x $10^{-3}s^{-1}$	Ambient 21^0C→23^0C	40

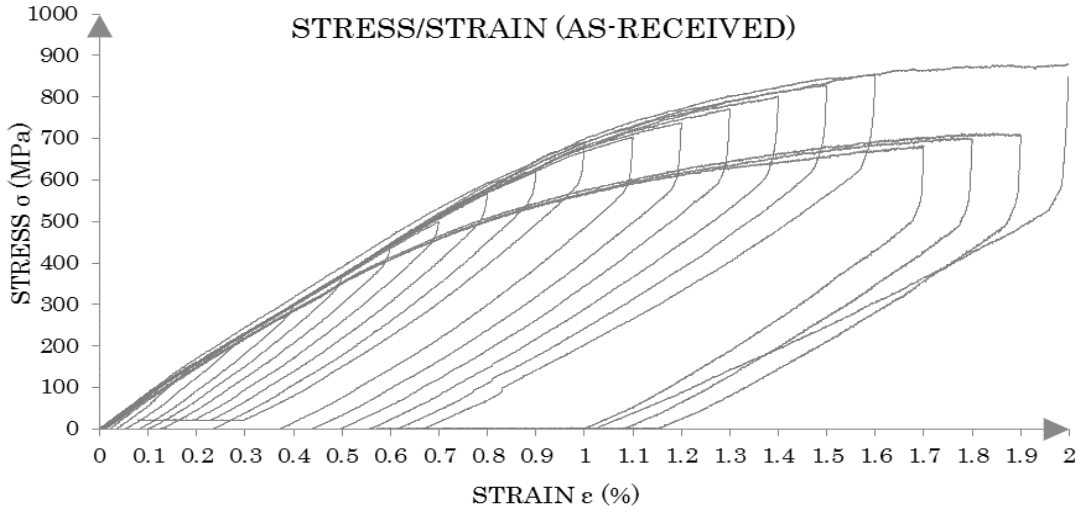

Figure 4.1: *Stress-Strain response for As-Received NiTi Specimens: Cycles 1-20*

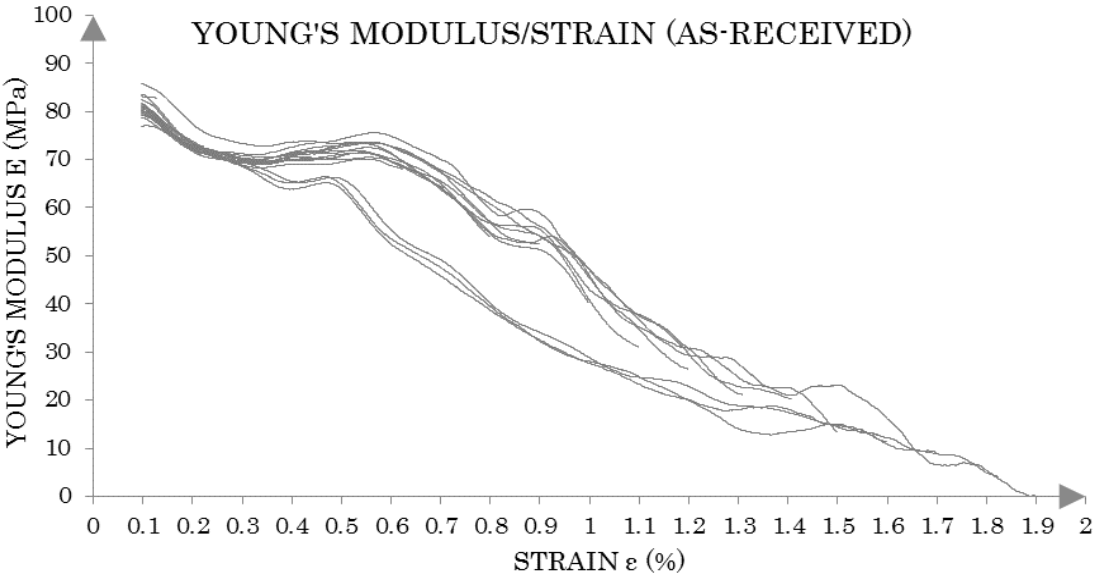

Figure 4.2: *Tangent Modulus-Strain for As-Received NiTi Specimens: Cycles 1-20 Loading*

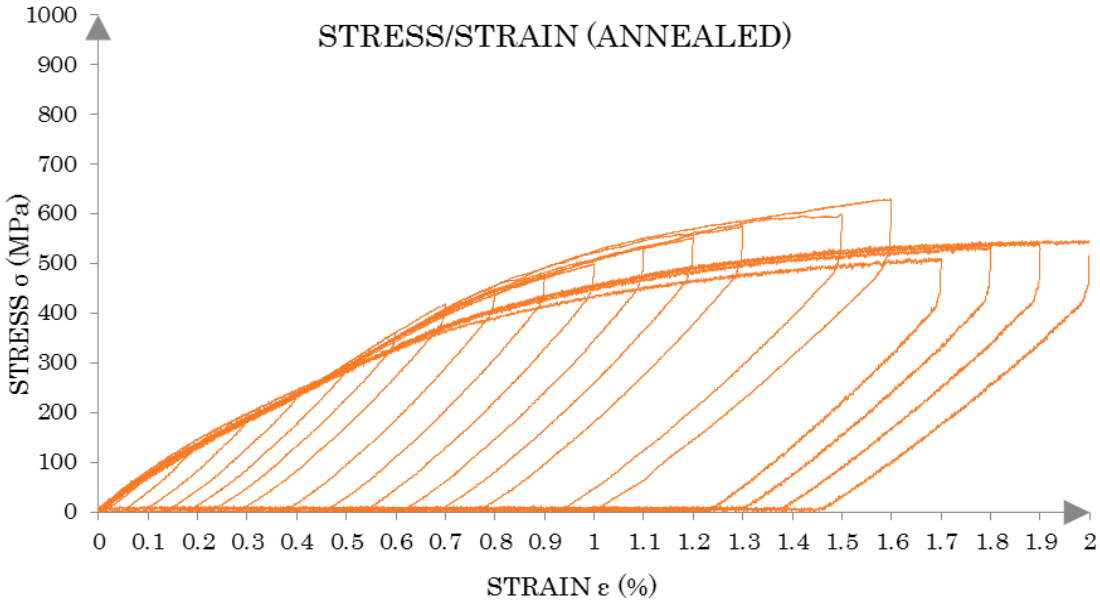

Figure 4.3: *Stress-Strain response for Annealed NiTi Specimens: Cycles 1-20*

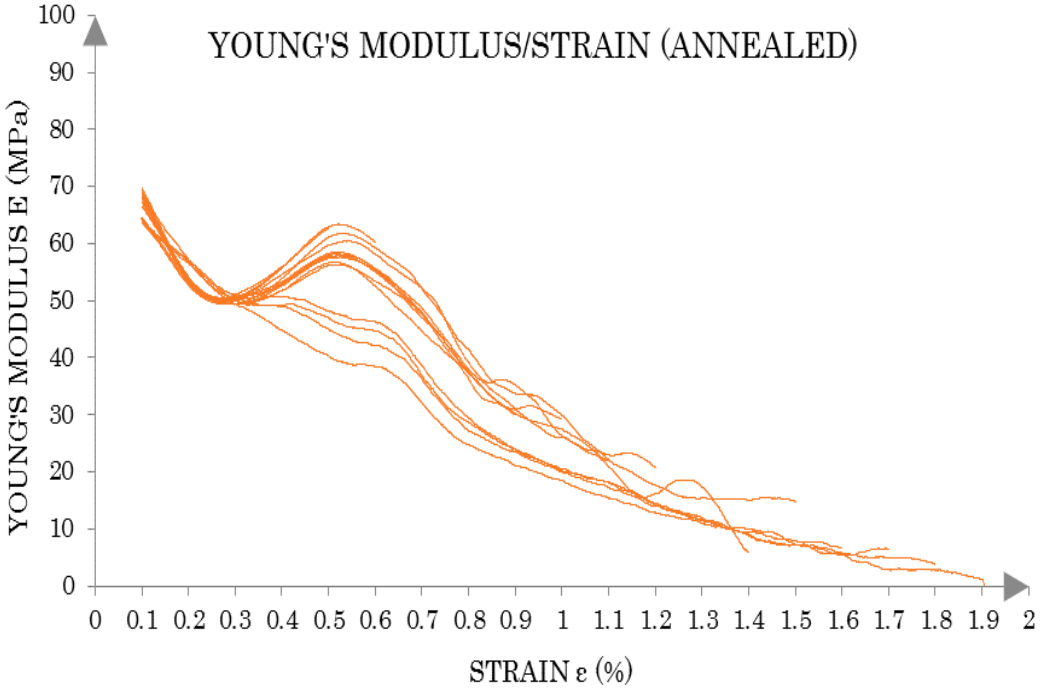

Figure 4.4: *Tangent Modulus-Strain for Annealed NiTi Specimens: Cycles 1→20 Loading*

It is clear that these results do not follow the traditional stress-strain response obtained from a NiTi tensile test. This is because the global flexural response is determined by both tensile and compressive forces, which comparatively exhibit a substantial heterogeneity: [16] observed a higher transformation strain value coupled with a lower transformation stress value for tension compared to that for compression, and an emergence of localised strain only under tension in their comparative study. Moreover, this asymmetry affects the flexural strain distribution profile resulting in a complex mechanical response under flexural deformation.

The mechanical response has distinct regimes consistent over the differing specimen states. This portion concentrates on the evaluation of the global response observed through cycles 1-16. Under loading, the initial region between 0→0.25% strain launches with tangent modulus that ranges from 75-85MPa for as-received condition and 65-70 MPa for the annealed condition. This gradually reduces to 70 – 75MPa and 50-55 MPa respectively at 0.25% strain. Following this the global tangent modulus undergoes an increase up to a strain value of approximately 0.5% and a modulus of 70-80 MPa and 55-56 MPa respectively. The final segment, 0.5% → 2% strain, comprises a gradual reduction of the tangent modulus as it approaches a more compliant "plateau" region ending with small positive tangent modulus.

The response through unloading can be defined through two distinct phases. Initial unloading is characterised by a steep vertical segment with minimum change in strain magnitude. An abrupt change in the response occurs at the end of this segment as strain recovery commences. Thereafter the response decreases in a monotonic manner with a shallowing tangent modulus. As these tests are conducted at a temperature range, which falls within the specimen's martensitic phase, at the end of unloading there is a retained deformation.

Through advancing thermo-mechanical cycles (17→20), however, there is a change to the characteristics of this response. While the loading sequence commences in a near-identical manner, differences are observable past 0.25% strain magnitude. The abrupt increase that was previously observed in the tangent modulus between 0.25→0.5% strain magnitude is now supressed, and instead the tangent modulus decreases in a linear manner until the completion of the loading cycle. This ultimately results in an earlier but more gradual transition towards the "plateau" point on the stress-strain response. The change in the material response is carried through to unloading: while the material still follows two distinct phases through this process, the tangent modulus in the secondary strain recovery phase is markedly higher. This results in a greater percentage of unrecovered strain at zero stress.

This phenomenon can be attributed to the stabilisation of the R-Phase after the critical thermo-mechanical cycle is reached. On a crystallographic level, dislocations are introduced by the thermo-mechanical cycling, with the density of the dislocations increasing with further cycles. The higher dislocation density hinders martensitic transformation resulting in a gradual reduction in M_s, which in turn activates and promotes the continued existence of the R-Phase [83]. Beyond the critical number of thermal cycles, these effects lead to a saturation point where the R-phase gets stabilised. This can be very advantageous for any application utilising the Shape Memory Effect as it improves the cyclic constancy by controlling the decay of strain recovery, which would otherwise occur.

4.3 Constant temperature strain sweep

The main objective of this study is to replicate deflection behaviour of a NiTi plate actuator concept over a range of static temperatures with increments of strain. Table 4.2 highlights the experimental parameters followed to obtain this result. The typical loading path of the specimen is depicted in Figure 4.5, which corresponds to a strain sweep type test. The crossing of phase transformation boundaries between A→B represents the reverse transformation and C→D the forward transformation.

Table 4.2: *Constant Temperature Tests*

Strain	Strain rate	Temperature Min/Max	Total tests
1%	$1 \times 10^{-4} s^{-1} \rightarrow 1 \times 10^{-2} s^{-1}$ (3 steps)	$-13°C\ A_f \rightarrow +12°C\ A_f$ (6 steps + 6 steps reverse)	36

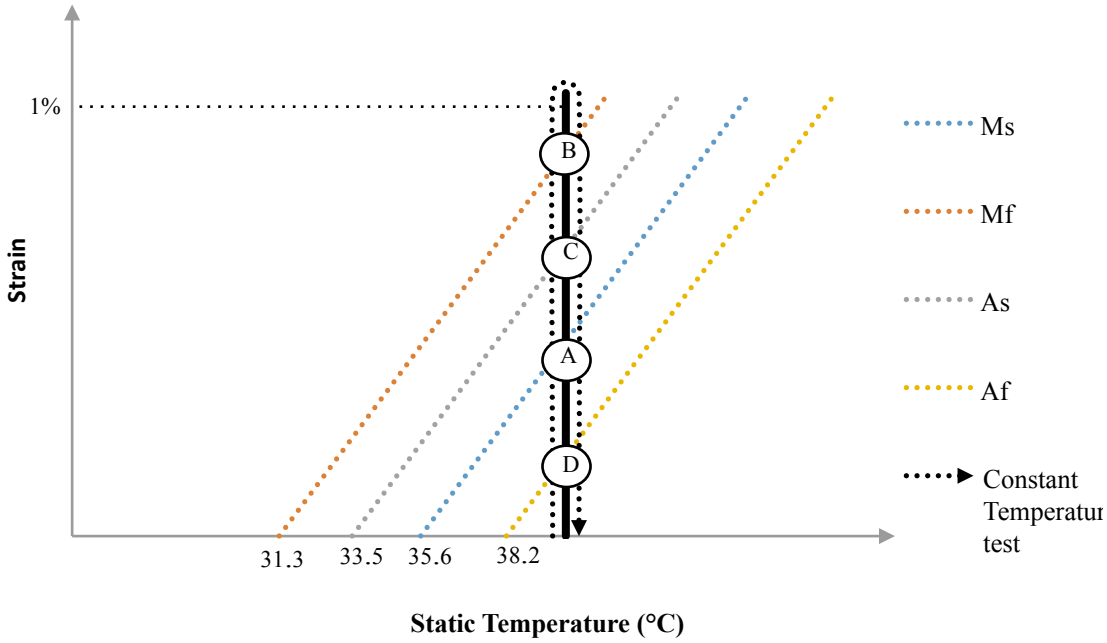

Figure 4.5: *Schematic of loading path followed in the constant temperature tests and the points at which they cross the phase transformation boundaries*

The tests are sequenced so that strain is always recovered after a cycle that is loaded from the martensitic phase: the subsequent

cycle runs above A_f and activates the SMA. In addition to this, a "dwelling" period of 30 minutes is given for the specimen temperature to equalise with the ambient temperature prior to each test. Loading sequences for each of the initial 18 tests are repeated in reverse order to account for the temperature history sensitivity of the material. The strain is regulated by a displacement input, which restricts strain relaxation, which would otherwise occur due to phase transformation.

The sampling rate, 100/1µm, is set as a function of deflection rather than time, ensuring a degree of uniformity between the three strain rates. A consequence of this high sampling rate is the accumulation of an excessive volume of data (40,000 data points from each test). To condense the data into a more manageable size, a macro programme that calculates the mean value between every 100 data points is deployed. This method is favoured over the use of a lower sample rate as it lessens the weightiness of erroneous data.

Stress-strain data obtained from the forward temperature scan of 25°C → 50°C at strain rates of 1 x $10^{-4}s^{-1}$, 1 x $10^{-3}s^{-1}$ and 1 x $10^{-2}s^{-1}$ are depicted in Figures 4.6, 4.8 and 4.10 respectively. In principle, the slower strain rates ensure quasi-static loading conditions to be satisfied. In these conditions the inertia force is insignificant and can be ignored. On the other hand, the higher dynamic -type strain rate loading has the potential to induce a temperature rise that alters the pseudoelastic response of the material.

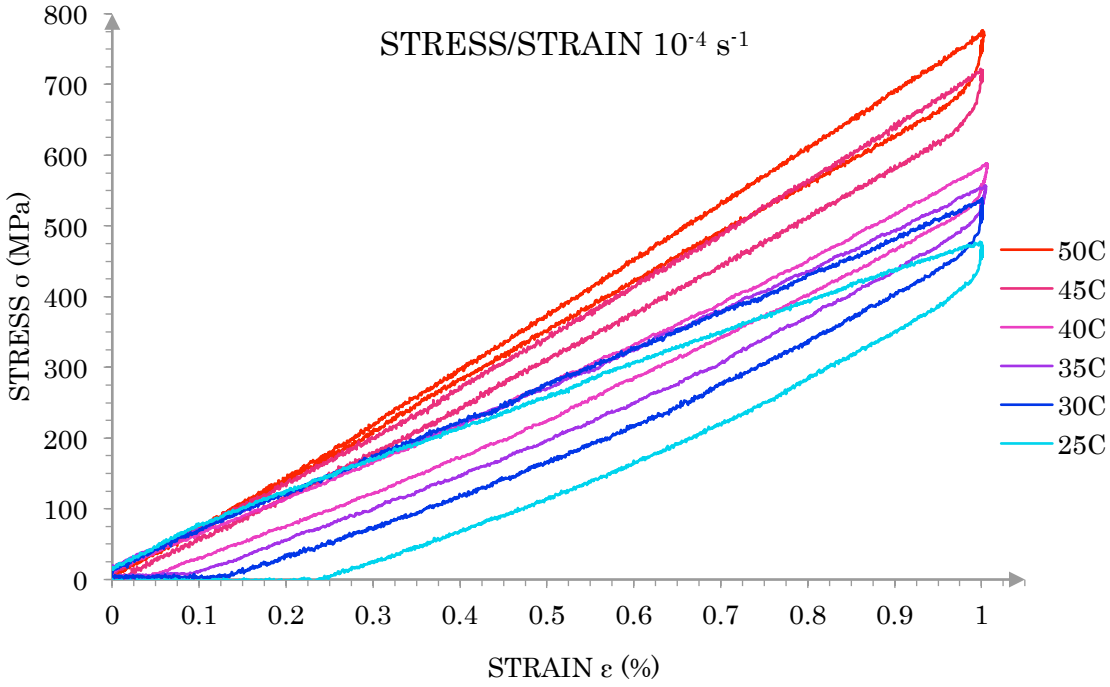

Figure 4.6: *Stress-Strain curves obtained with loading rate of $10^{-4}s^{-1}$ at different temperature magnitudes*

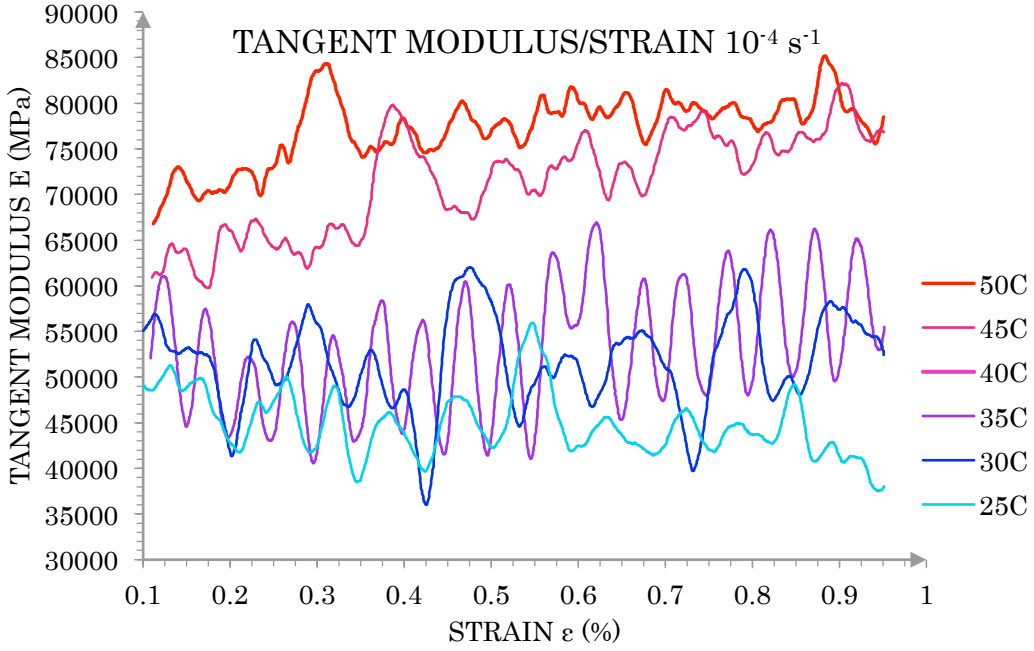

Figure 4.7: *Tangent Modulus-Strain curves obtained with loading rate of $10^{-4}s^{-1}$ at different temperature magnitudes*

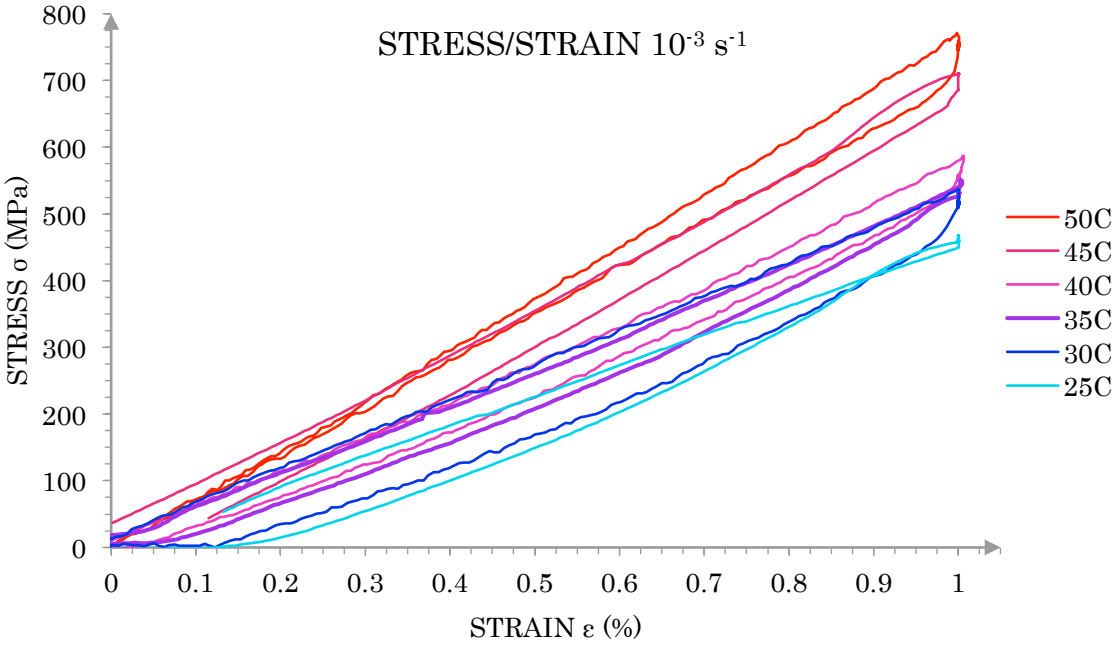

Figure 4.8: *Stress-Strain curves obtained with loading rate of $10^{-3}s^{-1}$ at different temperature magnitudes*

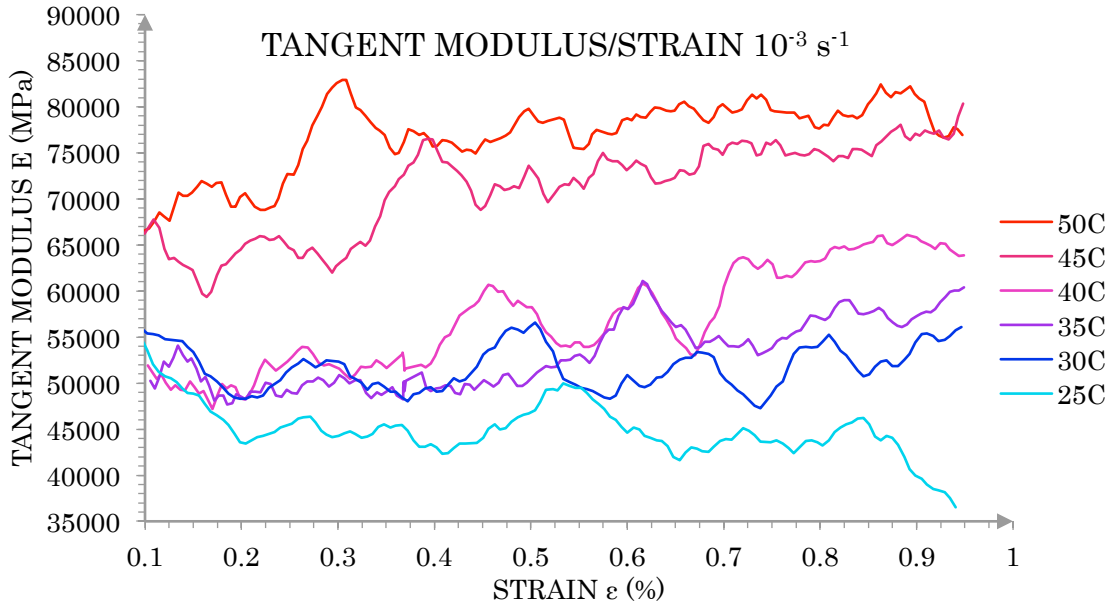

Figure 4.9: *Tangent Modulus-Strain curves obtained with loading rate of $10^{-3}s^{-1}$ at different temperature magnitudes*

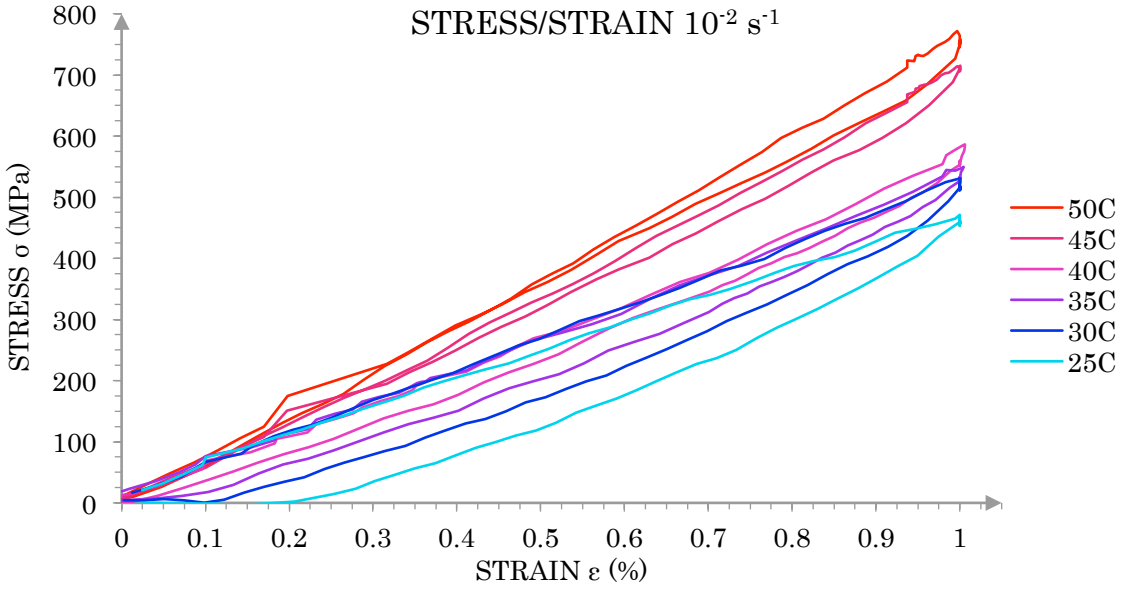

Figure 4.10: *Stress-Strain curves obtained with loading rate of $10^{-2}s^{-1}$ at different temperature magnitudes*

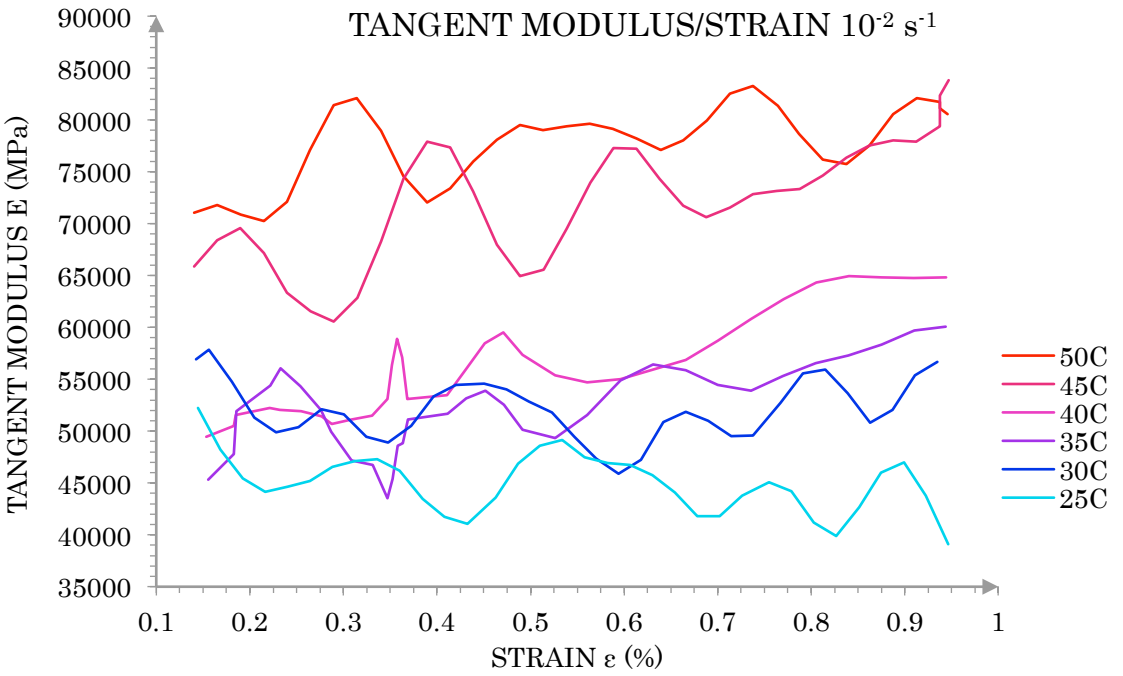

Figure 4.11: *Tangent Modulus-Strain curves obtained with loading rate of $10^{-2}s^{-1}$ at different temperature magnitudes*

Typical of NiTi SMA response, the material observes a reverse correlation to temperature change to what is the norm with other materials– NiTi stiffness increases with temperature. This relationship is further illustrated in Figures 4.7, 4.9 and 4.11, which tracks variation in the tangent modulus as a function of strain. The tangent modulus ratio is estimated from the gradient of the material response and calculated through increments of 0.1% strain.

Temperatures below the A_s temperature corresponds to the tangent modulus of pure martensite, and above Af, the tangent modulus of pure austenite. At intermediate temperatures, this value is governed by the volume fractions of martensite and austenite present. While this is true in theory, due to the presence of a complex mix of tensile and compressive forces in our tests, the material does not follow a linear response in any of its stages.

There is a distinct "jump" observed in the Tangent Modulus from 40°C → 45°C. While this indicates the materials transformation from martensite to austenite at zero stress, the DSC data suggests this step should have occurred between 35°C→40°C as the materials A_f temperature is 38°C. One possible hypothesis is that the "Dwell" time was insufficient for the specimen to equalise with the ambient temperature. On the other hand, this could be a result of a small discrepancy in response between the DSC samples and the specimen, likely attributed to machining affects.

Following the material response, it is evident that the point of

apparent yield - marked by a change in gradient - occurs at an earlier time-point at lower, sub-austenitic temperatures. This signifies the initial stages of stress induced martensitic transformation. Prior to this, deformation is governed by dislocation generation and movement from the multiple variants of martensite present. In contrast, the stress-induced martensitic structure, which subsequently present, deforms by moving twin boundaries.

The comparison of the material response between the different loading rates suggests a minimal variance. This is consistent with observations from Liu et al [84], who studied behaviour over a broader range of strain rates – 3x10-4 → 3000/s, and hypothesised that the deformation mechanism does not change with strain rate. These findings differ from Tobushi et al. 1998 [104]. In their dynamic tensile tests, they detected an increase in the stress and temperature required for martensitic transformation with strain rates above 1.67/s. This study was not able to replicate such high strain rates as they were outside the operating envelope of the test-stage.

One minor pattern emerging from these results is an apparent decrease in the stress hysteresis loop formed between the loading/unloading phases with higher strain rates. The strain rate dependence of the stress hysteresis is governed by the rate of heat release/absorption (controlled by the loading rate) and the rate of heat transfer to the environment. Increases in the strain rate

shorten the loading time and result in a faster latent-heat release and enhanced heat accumulation in the specimen. Theoretically, this would result a higher specimen temperature during forward transition (loading) increasing the transformation stress. Adversely, faster cooling of the specimen during reverse transformation would result in a lower transformation stress. However, at dynamic strain rates (as observed in this study with the strain rate of $1 \times 10^{-2} s^{-1}$), the heat release through loading does not have enough time to transfer out completely and is carried to the unloading phase, increasing the specimen temperature at the onset of the unloading phase. This would in turn increase the transformation stress and widen the stress hysteresis loop. This occurrence could have been avoided by implementing longer "dwell" periods between the loading and unloading phases to lower the interference between the two processes.

4.4 Constant Strain Temperature Sweep

The main objective of this study is to replicate the actuation behaviour of the NiTi plate actuator concept over a range of static strains with increments of temperature. The deformation recovery characteristics of the NiTi plate specimens at different load magnitudes are analysed to accomplish this. Table 4.3 highlights the parameters used in this study, which allows the evaluation of macroscopically observable material characteristics and microstructural changes over the stated temperature range.

Table 4.3: *Constant Strain Tests*

Strain Min/Max	Temperature Min/Max	Temperature ramp rate	Optical Imaging	Total tests
0.25% → 1% (At -10°C A_f/ 4 steps)	-10°C A_f → +10°C A_f → -10°C A_f	1 x 10^{-1} °CS^{-1}	Static temperature holds (21 steps/every 2 °C)	4

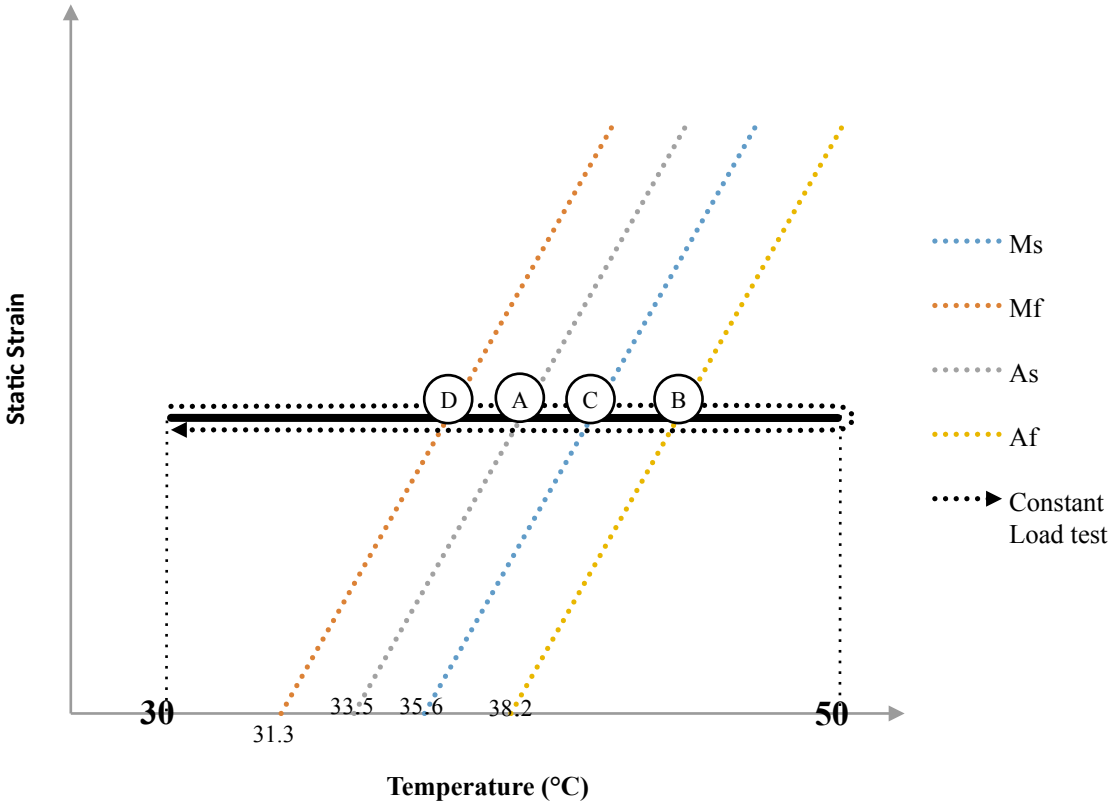

Figure 4.12: *Schematic of loading path followed in the constant strain tests and the points at which they cross the phase transformation boundaries*

The loading cycle is depicted in Figure 4.12 and corresponds to a temperature sweep test. A→B represents the reverse transformation and C→D the forward transformation. A pre-strain (0.25%→1%) is applied on the specimen before the start of the temperature sweep cycle. The implementation of a static load parameter, while mimicking the operation of an actuator utilising the shape memory effect, would have hindered the effectiveness of the in-situ study, which necessitated a static observational area. As a result, these tests are regulated by a displacement input instead, which constrains strain recovery during the temperature sweep cycle.

Consequently, the main macroscopic observable parameter obtained through the MTS test system is the recovery stress. Figure 4.13 and Figure 4.14 illustrate the changes in recovery stress as a result of the temperature sweep cycle for tests conducted with strain magnitudes of 0.25%, 0.5%, 0.75% and 1%. The corresponding changes in the tangent modulus are illustrated in Figure 4.15 and Figure 4.16.

Similar to all other tests in this study, the specimen is heated past its austenite finish (Af) temperature prior to each subsequent test to eradicate the presence of stress-induced martensite and ensure that strains are not carried over between tests. This is executed at zero strain, using an identical temperature ramp rate.

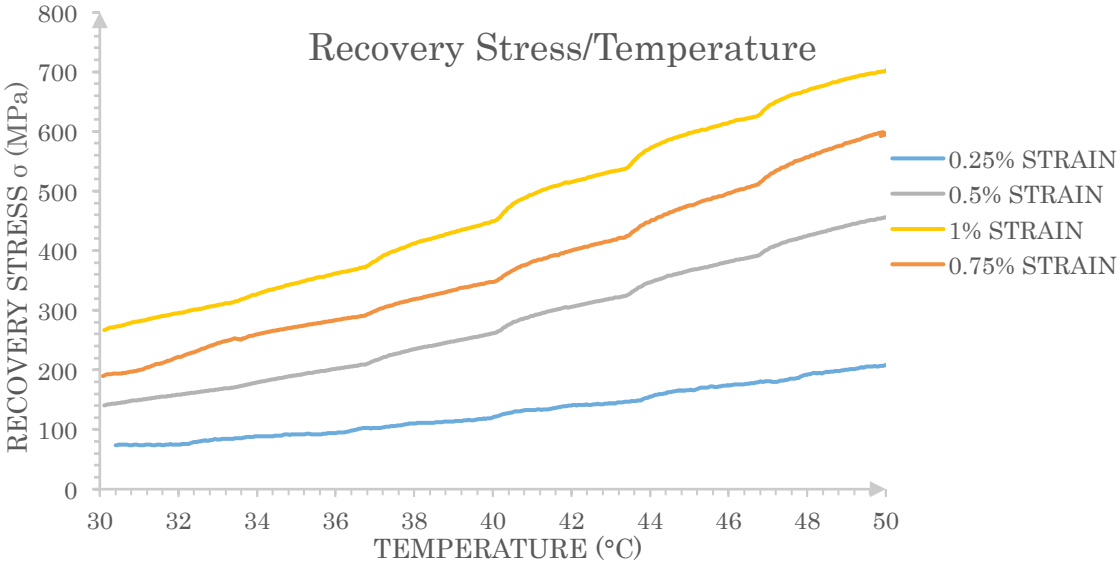

Figure 4.13: *Recovery Stress as a function of temperature for the forward temperature scan of 30°C→50°C at different strain magnitudes*

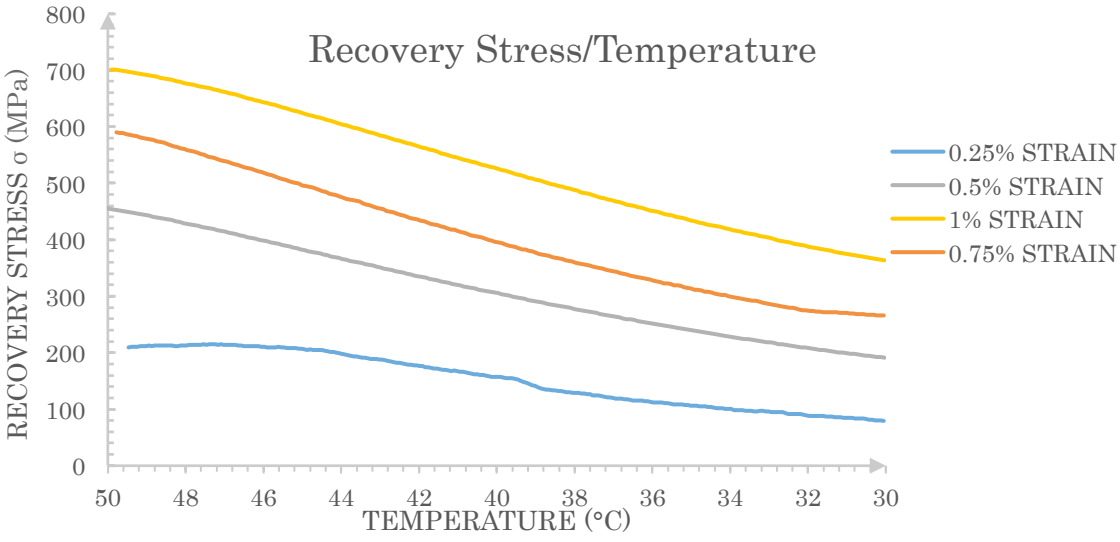

Figure 4.14: *Recovery Stress as a function of temperature for the reverse temperature scan of 50°C→30°C at different strain magnitudes*

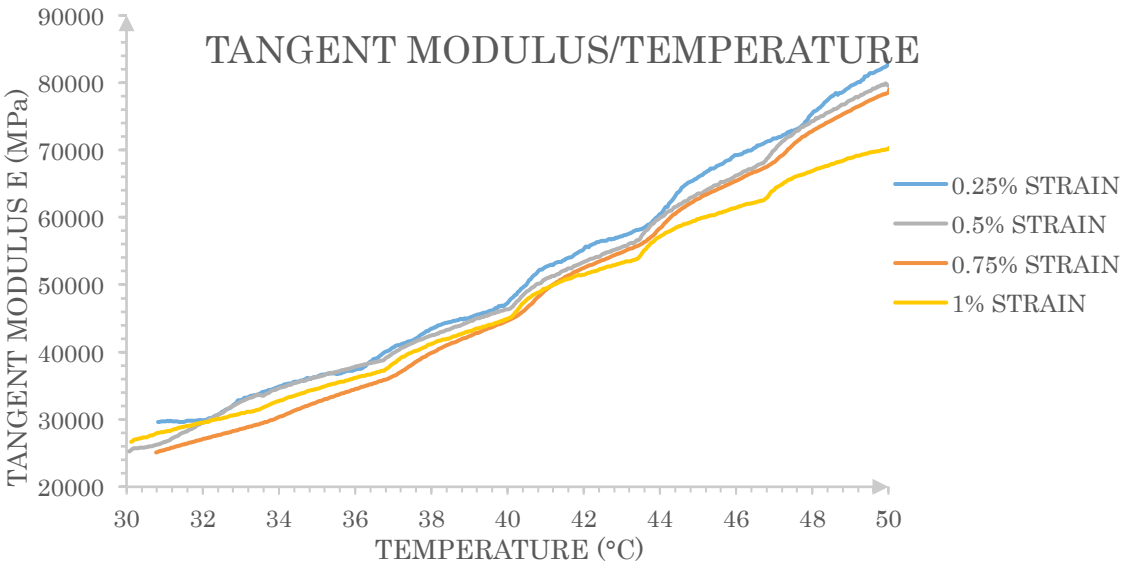

Figure 4.15: *Tangent Modulus as a function of temperature for the forward temperature scan of 30°C→50°C at different strain magnitudes*

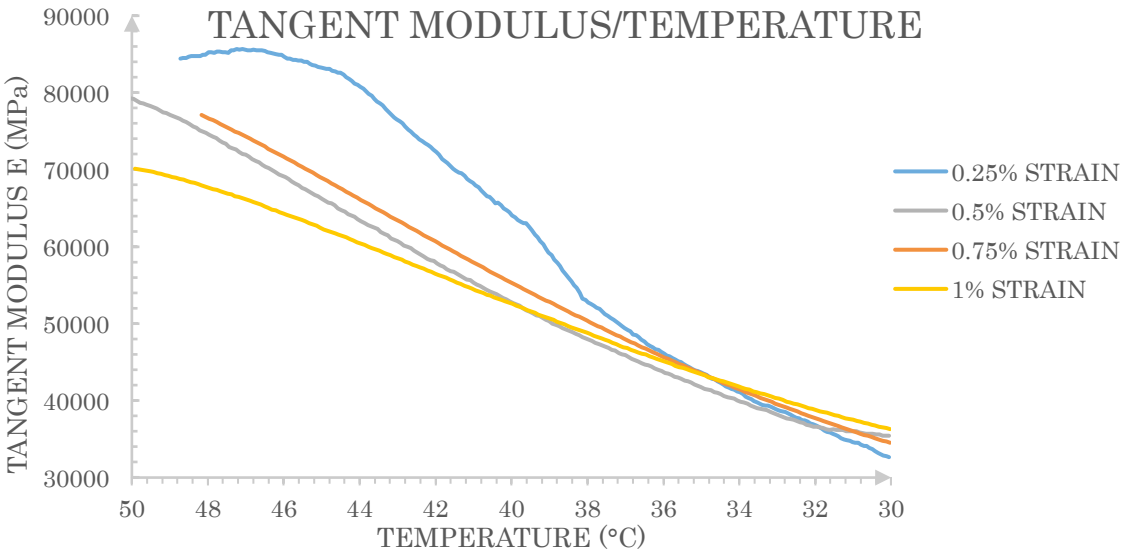

Figure 4.16: *Tangent Modulus as a function of temperature for the reverse temperature scan of 50°C→30°C at different strain magnitudes*

The global macroscopic response of the NiTi plate specimen under this test condition can be summarised as follows. During heating, recovery stresses are generated from the onset temperature (30°C). The stress increases with temperature until the maximum temperature of 50°C is attained. An almost linear increase to the tangent modulus during this segment suggests a parallel increase in the rate of recovery stress increase at the top of the temperature cycle.

Analysing this response in more detail, a "stepped" increment is observed in the increase of recovery stress. This occurrence is a direct result of application of temperature control by the MTS test system and is not indicative of material behaviour. The temperature regulation system on the MTS test system is equipped with high capacity heating elements which are designed to operate in unison with active cooling. As these tests are conducted at temperatures very close to the ambient without using active cooling, the system struggles to maintain a smooth temperature increment.

The cooling segment of the temperature sweep results in decreasing recovery stresses. There is no evidence of a "stepped" incremental response as the material cooling undertaken naturally with no interference from the MTS temperature control element. A hysteresis can be observed between the heating/cooling responses: decreasing temperatures correspond to higher recovery stresses

than increasing temperature. This can be attributed to differences between the forward and reverse phase transformations temperatures. Moreover, increase in recovery stresses under cooling suggests that the austenite→martensite transformation occurs at a lower temperature point than the martensite→austenite transformation. This behaviour is indicative of the loading history dependence on NiTi response, in this instance as a result of the temperature history.

While the above describes the general global response observed through the temperature sweep study, there are noteworthy changes to the response characteristics for the cycle conducted at the lowest strain magnitude (0.25%). Tracking the response under cooling, there is no initial reduction in the tangent modulus, which commences with a positive gradient that eventually "plateaus" (50°C→47°C). The tangent modulus then sharply decreases to a point where it approaches the response from other strain magnitudes (47°C →38°C). At this point, an abrupt change in the tangent modulus occurs as it merges with responses obtained from higher pre-strains (38°C →30°C). These three distinct phases can be explained at a crystallographic level through phase specific behaviour. The material is mainly Austenitic in the initial phase between 50°C→47°C as there is no discernible change in the tangent modulus of the material. The sudden drop in the tangent in the period between 47°C →38°C indicates the material is in a

transitional phase consisting of an austenite and martensite formulation. The final segment under cooling, 38°C →30°C, at which point the tangent modulus closely matches other tests, the material assumes martensite-rich phase.

4.5 Digital Image Correlation

Load, Displacement and Temperature are measured by the MTS test system throughout every four-point bend test. With these three variables, it is possible to map NiTi behaviour at a macroscopic level in the flexural deformation regime. However, to identify the cause behind any given macroscopically observed phenomena, it is necessary to delve deeper and analyse at a granular level.

This study utilises optical in-situ techniques to capture micrographs of the specimen edge during four-point flexural tests. The micrographs are processed using Digital Image Correlation analysis to obtain two-dimensional local displacement and strain field maps. The analysis of such strain distributions can potentially shed light towards corresponding global responses. It is particularly informative in the case of NiTi due to its inhomogeneous, complex behaviour, which promotes localised strain concentrations.

Ncorr v1.2 is used for DIC image processing to obtain the

displacement and strain fields from deformed micrographs. Ncorr is an open source 2-D digital image correlation programme, which sits within the MATLAB environment. Its DIC analysis algorithms are based on the Reliability Guided DIC framework developed by Pan [132], using circular and contiguous subsets. The RG-DIC method eliminates repeating redundant calculations involved in conventional Newton-Raphson algorithm-based DIC method. This equates to computational times 120-200 times faster than of traditional methods, without any loss of measurement accuracy [133].

4.5.1 Digital Image Correlation Parameters

Ncorr produces 2-D axial strain field measurements of the specimen edge as it is subjected to the constant strain temperature sweep tests as presented in section 4.4. These tests consist of forward and reverse temperature scan of -10°C A_f → +10°C A_f → -10°C A_f at a rate of 1 x 10^{-1} °CS^{-1}, whilst the specimen is subjected to a fixed global strain. During each temperature sweep test, 21 in-situ optical micrographs are captured within static temperature holds at 2°C intervals.

This study utilises 4 individual RG-DIC analysis sets, each representing a different global strain value: 0.25%, 0.5%, 0.75% and 1% global strain. One RG-DIC analysis is comprised of 10 micrographs, a reference image captured at zero strain, followed by

9 deformed micrographs captured at 4°C temperature intervals within the temperature sweep 32 °C → 48 °C → 32 °C (-8°C A_f → +8°C A_f → -8°C A_f).

The micrographs are cropped to ensure the horizontal and vertical centrelines of the NiTi plate cross at the centre of each micrograph, and further cropped to compensate for plate movement due to the changes in temperature. This results in an analysed region of interest with dimensions of 0.9mmx0.5mm; 90% of the size of the original micrograph. The processed micrographs have a resolution of 3,456x1,944 pixels and a pixel resolution of 14.7ppμm^2.

For the forward RG-DIC analysis, a subset radius of 25pixels and a subset spacing of 1 was chosen. This was the smallest subset that did not result in noisy displacement data, whilst still providing sharp displacement and strain fields and being computationally efficient. Multithreading was enabled utilising 8 logical cores in the system to further speed computational time. The correlation coefficient cut-off which formats displacements to remove erroneous data points was set to default and a strain radius of 15pixels was selected. These settings were uniformly applied across all global strain magnitude DIC sets.

4.5.2 Digital Image Correlation Results

Previous studies that have been conducted in the area of in-situ

DIC analysis of NiTi specimens have focused on strain field analysis of NiTi under changes in load. This study attempts to extend the understanding of NiTi behaviour by tracking strain distribution under changes of temperature whilst maintaining a fixed global strain. This evaluated criteria is particularly significant in the field of actuation as it shows the changes in strain distribution as a result of the shape memory effect.

These prior DIC enabled studies can shed light towards what phenomena to expect, and how they would likely manifest in the strain field maps. One key criteria to evaluate is the location of the neutral strain axis where there is zero axial strain. In conventional materials that demonstrate a homogeneous response, the neutral axis runs through the centroid of the cross section. However, deviations to the neutral axis location can be triggered by asymmetry in the tension-compression response and further exaggerated due to phase transformations. Such phenomena would affirm that NiTi does not follow classical Euler-Bernoulli beam theory, which assumes that plane sections remain plane and normal to the longitudinal axis. The results may instead reveal localisations, which are present only in certain conditions.

The RG-DIC produced data sets are presented in Figures 4.17, 4.18, 4.19 and 4.20; representing global strain magnitudes of 0.25%, 0.5%, 0.75% and 1% respectively. Each figure is formed of 9 deformed micrographs captured at predetermined temperature values, with the strain field maps superimposed.

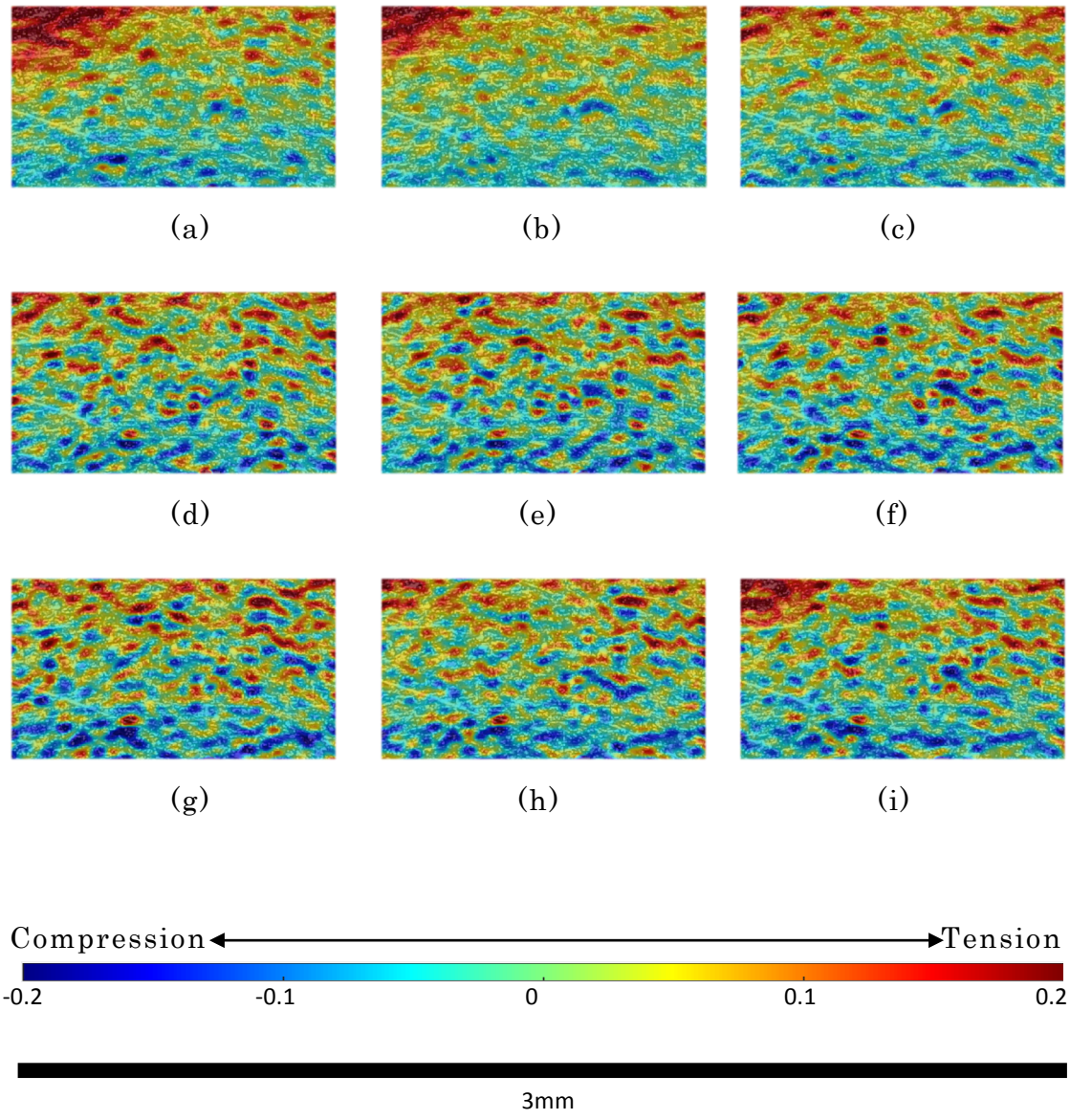

FIGURE 4.17: *In-situ DIC strain distribution superimposed onto deformed micrographs from temperature sweep at a global strain magnitude of 0.25%. Heating cycle (a) 32* °C*, (b) 36* °C*, (c) 40* °C*, (d) 44* °C, (e) 48 °C, and cooling cycle (f) 44 °C, (g) 40 °C, (h) 36 °C and (i) 32 °C.

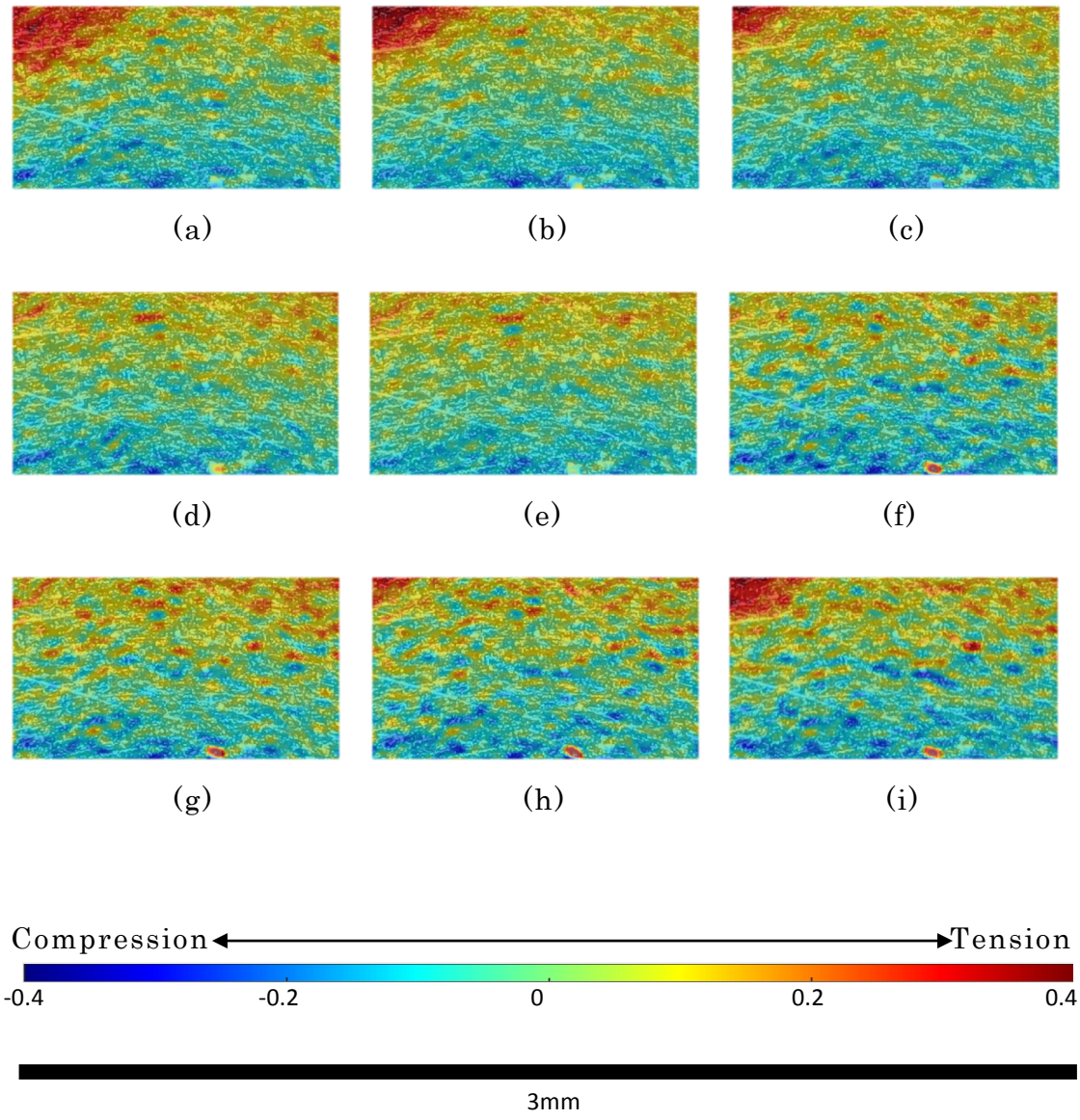

FIGURE 4.18: *In-situ DIC strain distribution superimposed onto deformed micrographs from temperature sweep at a global strain magnitude of 0.5%. Heating cycle (a) 32* °C*, (b) 36* °C*, (c) 40* °C*, (d) 44* °C, (e) 48 °C, and cooling cycle (f) 44 °C, (g) 40 °C, (h) 36 °C and (i) 32 °C.

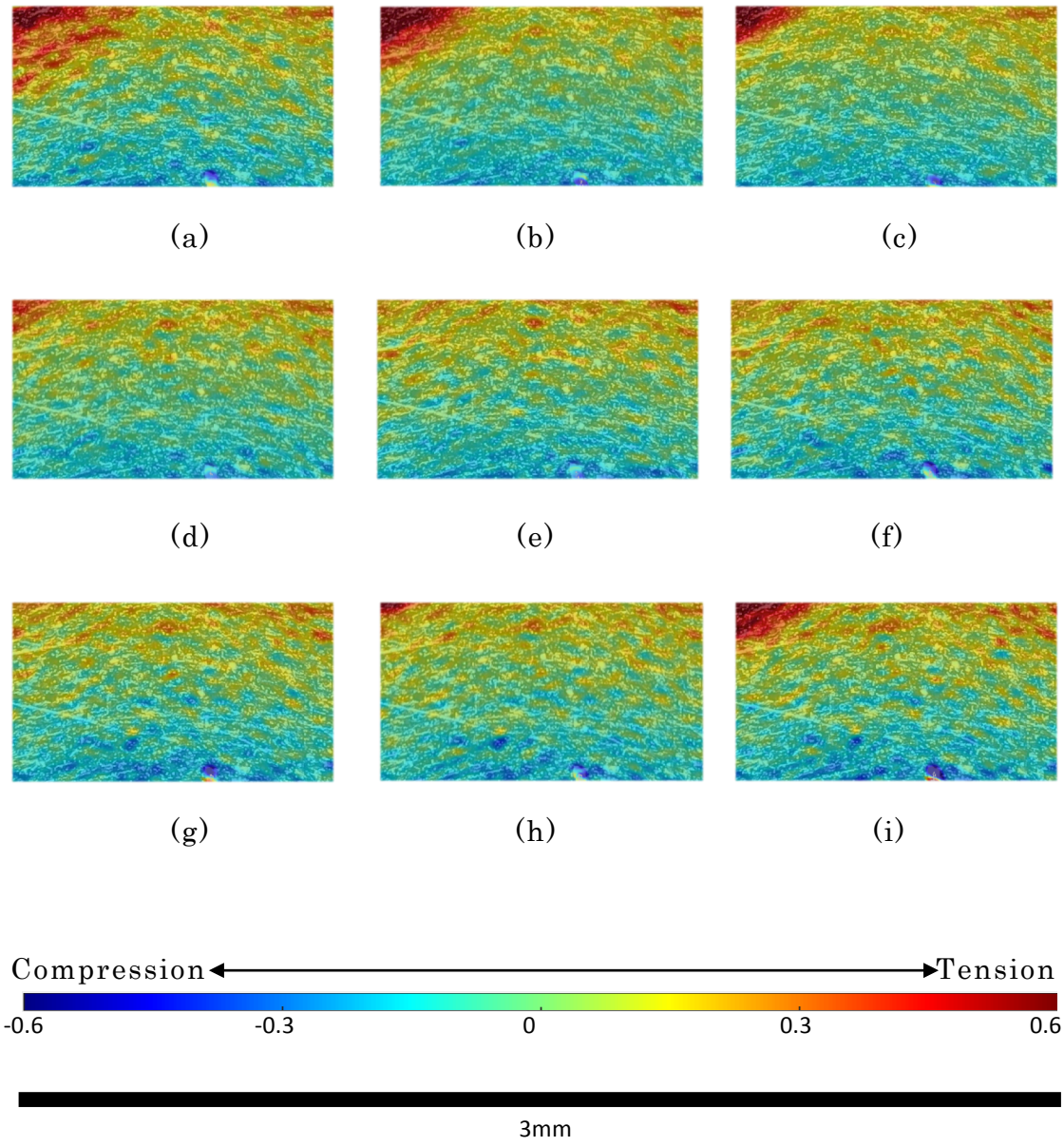

FIGURE 4.19: *In-situ DIC strain distribution superimposed onto deformed micrographs from temperature sweep at a global strain magnitude of 0.75%. Heating cycle (a) 32* °C, *(b) 36* °C, *(c) 40* °C, *(d) 44* °C, (e) 48 °C, and cooling cycle (f) 44 °C, (g) 40 °C, (h) 36 °C and (i) 32 °C.

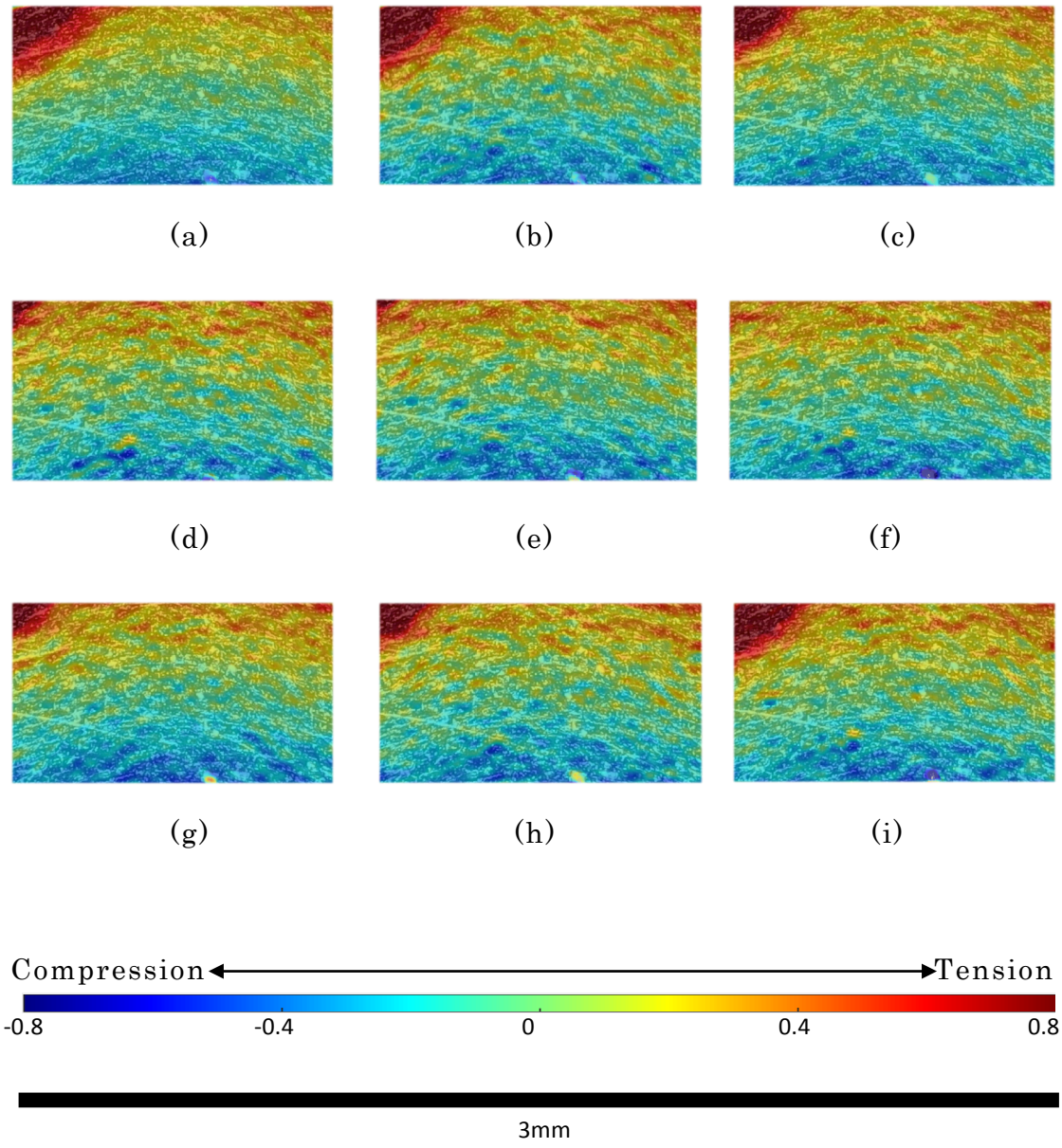

FIGURE 4.20: *In-situ DIC strain distribution superimposed onto deformed micrographs from temperature sweep at a global strain magnitude of 1%. Heating cycle (a) 32* °C*, (b) 36* °C*, (c) 40* °C*, (d) 44* °C, (e) 48 °C, and cooling cycle (f) 44 °C, (g) 40 °C, (h) 36 °C and (i) 32 °C.

The DIC processed strain field maps reveal strain profiles that are

characteristic of flexural deformation: tensile strains on the outermost (top) layer and compressive strains on the innermost (bottom) layer. Beyond this common trait, several distinguishing characteristics can be identified that differ from that of homogenous materials subjected to flexural deformation. There is one erroneous occurrence visible on some strain field maps due to a speck of dust on the camera lens (situated at the bottom centre). This can be ignored.

The most noticeable phenomenon is the localisation of axial tensile strain recorded towards the top left corner on many of the strain field maps. This is likely related to the diagonal "band" deformation pattern observed under tensile loads by Reedlunn et al [80] in their full field macroscopic DIC analysis. Thus, the triangular strain concentration witnessed may be an edge or tip of one of these band formations (this micro-scale analysis only focuses on 50% of the thickness of the specimen edge). The strain field maps indicate that this occurrence is largely independent of strain magnitude. On the other hand, temperature and temperature loading history are likely triggers for this behaviour. It is most pronounced at the beginning of the reverse temperature scan (heating cycle) and decays with increasing temperature. At temperatures over 44C substantial strain localisations are no longer visible. On the forward temperature scan (cooling cycle), tensile strain localisations are first noticeable on strain field maps at 36C. These localisations grow in size with decreasing temperatures. A clear pattern can be made in relation to this

occurrence and the parent phase at the temperature. Tensile deformation in band formations is preferred by NiTi in martensite form. On instances where phase variant mix is predominately austenite, a more homogenous deformation pattern is observed.

The neutral axis of the specimen shifts from the classical euler-beumer theory assumed central location with the application of flexural deformation. The point of zero strain lies approximately between 100 to 250 microns below the cross sectional centre on the strain field maps. This deviation is a by-product of the differentiating behaviours of NiTi under tension and compression. Moreover, this suggests that compression has a marginally higher stiffness modulus to that of tension. Another contributing factor to this asymmetrical response could be that the localisations observed in tension, accelerate tensile deformation. There is no discernible changes to the neutral axis location across the strain field maps, indicating that this behaviour occurs independently of strain magnitude or temperature changes.

Plietsch et al [135] in their study of asymmetrical behaviour in NiTi, report compressive transformation strains that were 50% of the magnitude of the corresponding strains under tension. The study terms this asymmetrical response phenomenon as the Strength Differential Effect (SDE). A similar study conducted by Orgeas et al [136], hypothesise that this behaviour is an intrinsic property of the stress induced martensite transformation. Liu et al [134] support this theory in their study of NiTi microstructure using TEM. They report dislocation mechanisms are dominant in

compression, while tension deformation commences with the detwinning of Martensite variants.

The step change in global strain magnitude incurs changes to the strain distribution. Strain field maps at the lowest global strain (0.25%) reveal that localisations occur at a granular level. As strains are enclosed within grain boundaries, they are largely unaffected by neighbouring grains. This results in many instances where both compressive and tensile strains often fall on the same axial plane. At the test's maximum strain value (1%), grain specific strain localisation is significantly reduced. Neighbouring grains on the same axial plane often share the same strain magnitude. This implies that as strain magnitude is increased, strain distributions that are initially controlled at a microstructural level, shift to a more homogeneic macroscopic distribution pattern.

CHAPTER 5
FEM: MODELLING AND ANALYSIS

5.1 Introduction

The Finite Element Method (FEM) is a computer simulation technique widely used by engineers and scientists to mathematically model and numerically solve very complex structural, fluid, and multi-physics problems. In the FEM, the shape of the design is modelled by a set of appropriate finite elements interconnected at points called nodes. These elements contain the material and structural properties that define the model behavioural characteristics.

This chapter presents the conceptualisation, development and analysis of the NiTi SMA plate derived VSV Actuator system. This is accomplished in a completely virtual environment via FEM driven modelling and analysis techniques, eliminating the need for any physical prototyping or testing. The initial step in this process was the exploration of modelling approaches in the literature review (Section 2.4), which identified that internal variable driven modelling techniques are the most suitable for this application. This chapter begins with a through analysis of the chosen

modelling approach – the Auriccio Model for Superelasticity and Plasticity of Shape Memory Alloys (Section 5.2). The next section is dedicated to the Verification and Validation of the ABAQUS SMA model against data obtained from the experimental study (5.3). After this is satisfied, FEM is utilised to demonstrate the design and operation of two actuator concepts, each exploiting differing strain recovery mechanisms (Section 5.4). This follows a comparative study that explores the pros and cons of each approach (Section 5.5). These efforts culminate at the presentation of the NiTi SMA derived VSV concept (Section 5.6).

5.2 Auruccio Model for Superelasticity and Plasticity of Shape Memory Alloys

The Finite Element Modelling and Analysis software suite ABAQUS (Dassault Systèmes, Providence, RI, USA) incorporates user defined material subroutine libraries that replicate SMA superelastic and plastic behaviour. The underlying algorithms, which this is built upon, were proposed by Auricchio and Taylor, 1997 [93], Aurichio, Taylor and Lubliner, 1997 [94] with extensive extensions by Rebelo, Walker and Foadian, 2001 [95]. Gong and Pelton, 2002 [96], Rebelo et al, 2000 [97] and Rebelo et al, 2003 [98] all commend this approach for its aptness at simulating the mechanical response and aiding development, fabrication and deployment of SMA-led devices.

The constitutive model describes material response through a

linear elastic component and a stress-induced transformation component. As the transformation component follows generalised plasticity theory, the resulting strain increment can be derived from a plastic potential [16-17]. The ABAQUS implementation allows for various material and control parameters to be established. One of such is the employment of temperature dependent transformation stress surfaces for tensile and compressive loading to determine the occurrence of forward and reverse martensitic phase transformation. The elastic properties for Austenitic and martensitic states can also be defined. The model responds to either mechanical or thermal loading.

A "NAME" parameter starting with "ABQ_SUPER_ELASTIC_N3D" in the material properties Dialog-box activates this material library within ABAQUS for 3-dimensional problems. The Superelastic-Plastic model necessitates the selection of 31 "DEPVAR" and 15 + 2NP "CONSTANTS". The material parameters that define the SMA behaviour are detailed in Table 5.1. As the Model operates through a logical process, it will unquestioningly process erroneous material data (input) to produce an undesired Model response (output) (Garbage in – Garbage out Philosophy). Therefore, the quality of the material parameters is paramount.

This study utilises values from stress-strain data obtained in the experimental study as a baseline for the forthcoming verification/validation study. The stress induced onset of austenitic and martensitic phases, their respective Young's Modulus, and the transformation strain magnitudes at which

phase transformations occur are imported from the results from the constant temperature tests. The changes in transformation stress due to changes in temperature are imported from results from the constant strain tests. The Poisson's ratio is imported from previous studies with a parallel set of specimens. Plasticity behaviour past the strain plateau is omitted, due to these extremities not been explored under actuation. As the flexural tests captured a combined compression-tension macro scale response, there is no specific data for the deformation regimes individually. As a result, the compression and tension parameters are mirrored, representing a simplified behaviour under the assumption that there is symmetry between their responses.

These parameters are input into ABAQUS to derive the Transformation stresses and strains. The resulting Stress-Strain and Stress-Temperature graphs that characterise the material response are depicted in Figure 5.1 and 5.2.

Using this framework, a typical mechanical loading sequence can be deconstructed as follows:

(1) Austenitic loading: Onset of loading → σ_{tL}^{S}. The material has an Elastic Moduli of E_A.

(2) martensitic loading: σ_{tL}^{S} → σ_{tL}^{E}. Corresponding strains $E_A * \sigma_{tL}^{S}$ → $((E_M * \sigma_{tL}^{E}) + \varepsilon^{L}$. This section is characterised by a Stress Plateau.

(3) Plastic Deformation: Defined through stress strain pairs σ_1^P, ε_1 … σ_{NP}^P, ε_{NP}.

(4) martensitic unloading: $\sigma_{tL}^{E} \rightarrow \sigma_{tU}^{S}$. The material has an Elastic Moduli of E_M.

(5) martensitic unloading plateau: $\sigma_{tU}^{S} \rightarrow \sigma_{tU}^{E}$. Corresponding strains $(E_M * \sigma_{tL}^{E}) + \varepsilon^{L} \rightarrow E_A * \sigma_{tU}^{E}$.

(6) Austenitic unloading: $\sigma_{tU}^{E} \rightarrow 0\sigma$. The material has an Elastic Moduli of E_A.

Table 5.1: Material parameters to describe SMA response

ρ	Density (tonne/mm^3)	6.5 x10^{-9}
T_0	Reference temperature	25
$\left(\frac{\delta\sigma}{\delta t}\right)_L$	Change in transformation stress / change in temperature during loading	5
E_A	Austenite elasticity (Mpa)	50000
ν_A	Austenite Poisson's Ratio	0.3
E_M	Martensite elasticity (Mpa)	50000
ν_M	Martensite Poisson's ratio	0.3
ε^L	Transformation strain	0.1
σ_{tL}^{S}	Start of transformation loading (Mpa)	100
σ_{tL}^{E}	End of transformation loading (Mpa)	1100
N_P	Number of Stress-Strain pairs to define yield curve	0
σ_1^P, ε_1 … $\sigma_{NP}^P, \varepsilon_{NP}$	Stress-Strain points in the yield curve	N/A
$\left(\frac{\delta\sigma}{\delta t}\right)_U$	Change in transformation stress/ change in temperature during unloading	5

σ_{tU}^{S}	Start of transformation unloading (Mpa)	0
σ_{tU}^{E}	End of transformation unloading (Mpa)	0
σ_{CL}^{S}	Start of transformation stress during loading in Compression (Mpa)	100
ε_{V}^{L}	Volumetric transformation strain	0.1

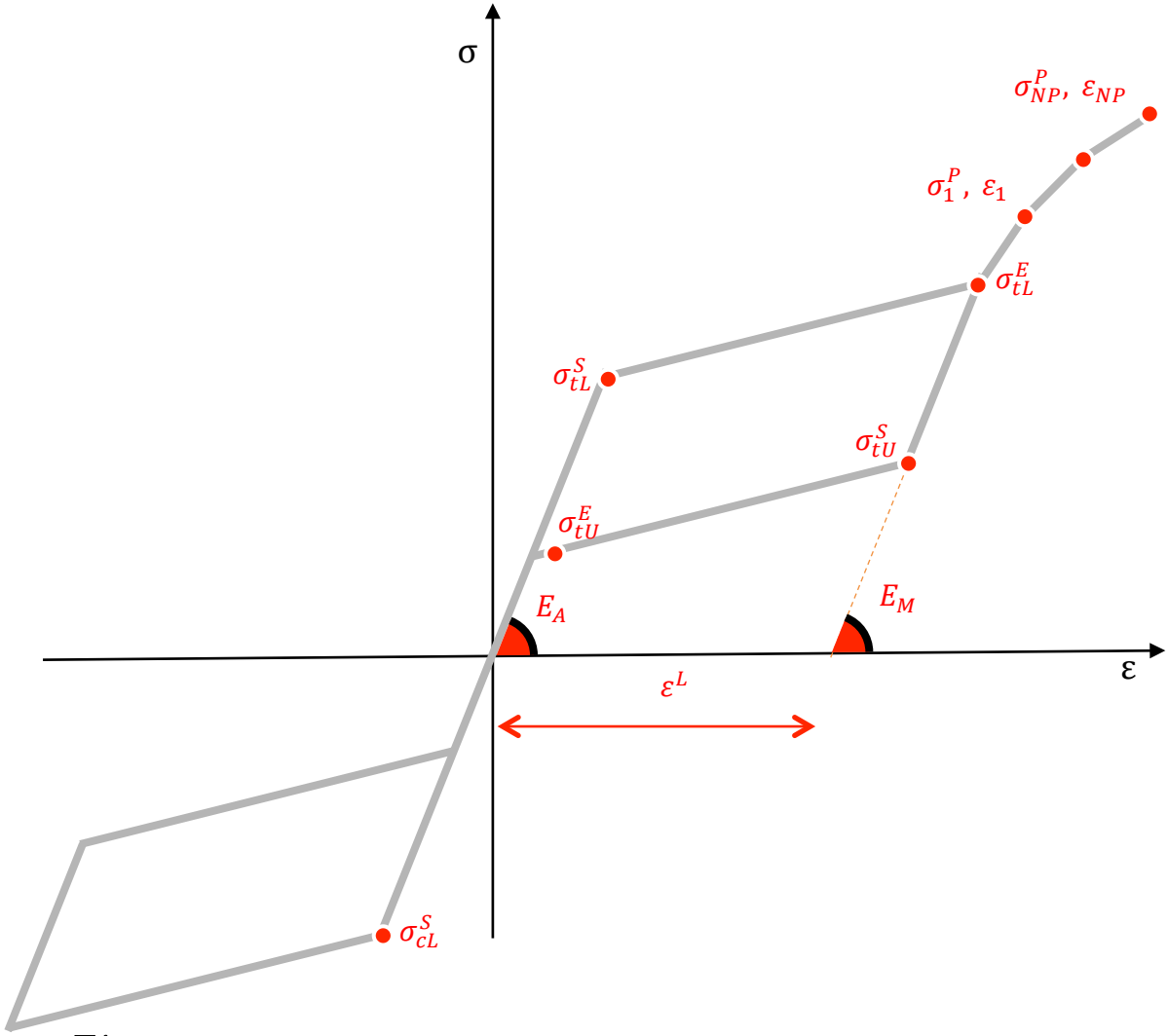

Figure 5.1: *Theoretical interpretation of NiTi Stress-Strain response*

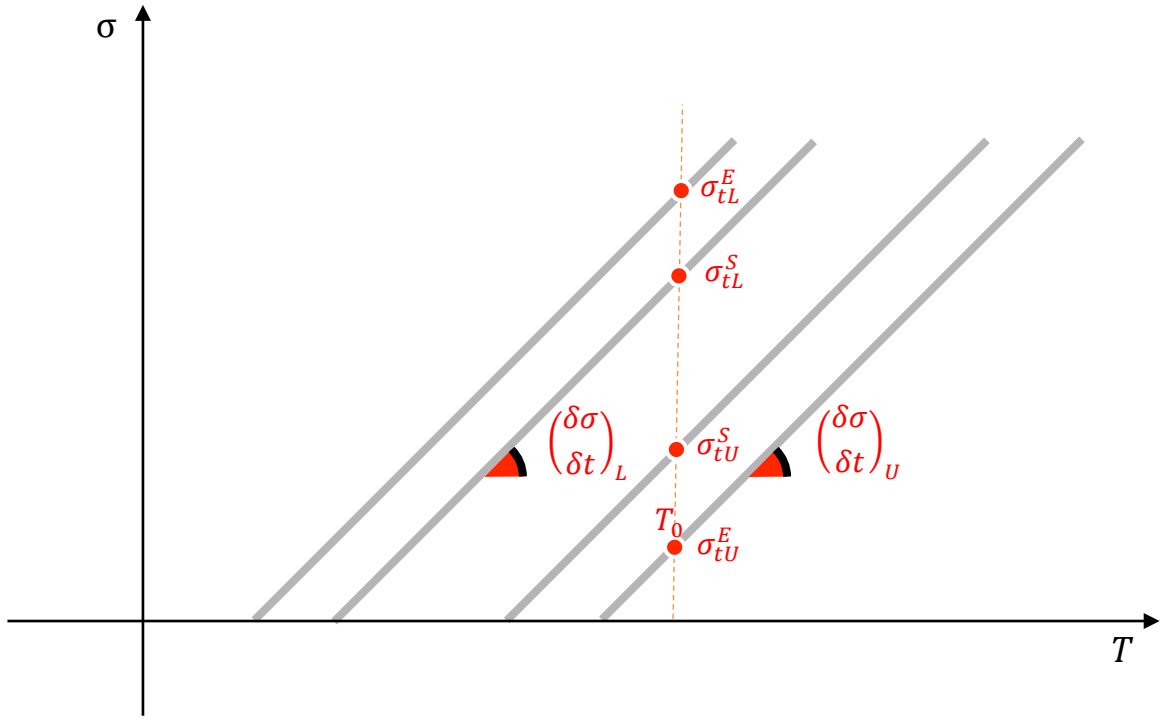

Figure 5.2: *Theoretical interpretation of NiTi Stress-Temperature response*

5.3 FEM Verification and Validation

Theoretically, the FEM model, once input with material parameters from the experimental study, should exhibit comparable behaviour to real world structure and environment. To ensure this is satisfied, the model is subjected to steps of verification and validation. Verification involves a mechanistic set of checks on the FEA model, which determine whether it accurately represents the underlying mathematical model and its solution. Validation on the

other hand quantifies the accuracy of the FEM model by comparing numerical solutions to the experimental data. Table 5.2 summarises the various questions posed through Verification and Validation.

Table 5.2: Verification and Validation gauges

Verification	Validation
Does it work?	Does it do what it is supposed to do?
Are the mathematics correct?	Are the physics correct?
Does it provide an accurate FE analysis?	Does FEA data compare favourably against experimental data?

5.3.1 Overview of FEM model

The aim of this FEM model is to recreate the four-point flexural tests presented in the experimental study. The bearings that form the flexural test fixture are represented in ABAQUS/explicit by four simple cylinders meshed with C3D8R *3D Stress* elements and assigned with aluminium material properties for elastic-only deformation (Table 5.3). The NiTi plate is assigned with parameters enabling the ABAQUS user material subroutine for Shape memory alloys (See section 5.2), and meshed with C3D8T *Coupled-Temperature-Displacement* elements.

The NiTi plate mesh is specified with a thickness of 3 elements (in the Y-Plane) to capture compressive and tensile stresses and strains in the outer, inner and neutral planes. While all the parts are created under a three-dimensional space, they are limited to 1 element in the Z-plane and constrained with *Z-axis symmetry* to optimise computational resources. Other boundary conditions enforced include *Pinned* for the lower bearings that restrict any movement or deformation, *X-Axis Symmetry* that ensures movement is constrained to the vertical plane, *Y-Axis Displacement Vector* for the upper bearings that controls displacement, and *Temperature* for the NiTi plate that simulates the effect of the temperature chamber. A *Penalty* type surface interaction is specified with a Coefficient of Friction of 0.1 to dampen any instabilities in the Model response. The *Vertical Reaction Force* at each of the two lower bearings is recorded, replicating the measurement at the load cell in the experimental study. The meshed Model Assembly is illustrated in Figure 5.3.

Table 5.3: Material Properties assigned for four-point flexure bearings.

Material Name	Density Tonne/mm^3	Young's Modulus Mpa	Poisson's ratio
Aluminium	2.8 x 10^{-9}	71,700	0.33

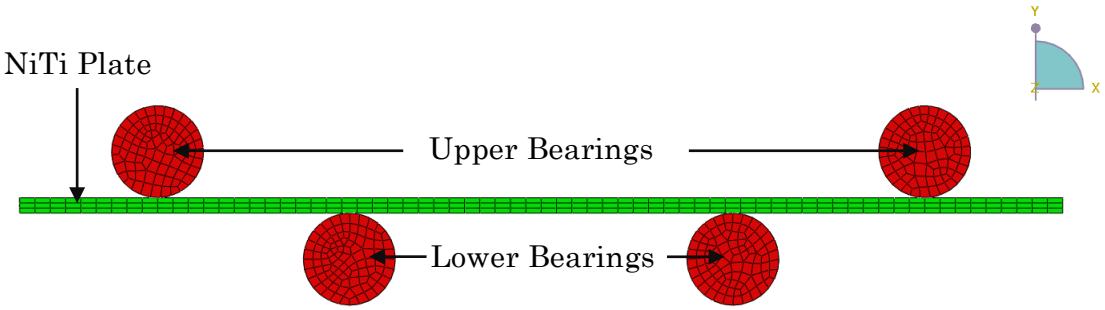

Figure 5.3: *ABAQUS Model Assembly replicating four-point flexural test fixture*

5.3.2 FEM study

A similar test schedule to the experimental study is employed with an aim of replicating the observed phenomena. Consequently, the model is run under the same three key experimental approaches: (1) Thermo-mechanical cycling, (2) constant strain temperature sweep and (3) constant temperature strain sweep.

Observed variables through ABAQUS include: (1) reaction force at the lower bearings, (2) displacement at upper bearings and (3) temperature inside environmental chamber. For the purposes of this comparative study, the output data is processed into the same formats as in the experimental study – the macro stress and strain values are calculated using the reaction force and displacement data.

5.3.2.1 FEM: thermo-mechanical cycling

The first FEM study is a replication of the thermo-mechanical

study in section 4.2. The test parameters employed for this FEM study are presented in Table 5.4. Maximum strain increment is limited to 1% (the experimental study maximum strain increment is 2%).

Table 5.4: Experimental variables employed for thermo-mechanical cycling FEM study

Test Type	Strain Min→Max	Strain ramp rate	Temperature Min/Max	Temperature ramp rate
Thermo-mechanical cycling	0%→1% (10 cycles, 0.1% increment)	$1 \times 10^{-4} s^{-1}$	Rt	N/A

The stress strain results from the FEM thermo-mechanical cycling test are depicted in Figure 5.4, with the corresponding experimental data depicted on Figure 4.3. The response obtained successfully captures the characteristic behaviour of SMAs. The stress-strain curve can be described by an initial elastic phase, followed by a stress plateau as it is subjected to mechanical loading. Unloading is characterised by a steeper stress-strain curve ending with a strain residual at zero stress. As this utilises global (macro) stress and strain calculations, the response is somewhat different to the theoretical model response (Figure 5.1), which illustrates the same variants at a local (micro) level. One particular occurrence in the FEM stress strain data is a "wobble" characterising the response. This is a result of the step

increment value selected in ABAQUS that decreases job computational times. It is not believed that this has any repercussions beyond the small "wobble" observed.

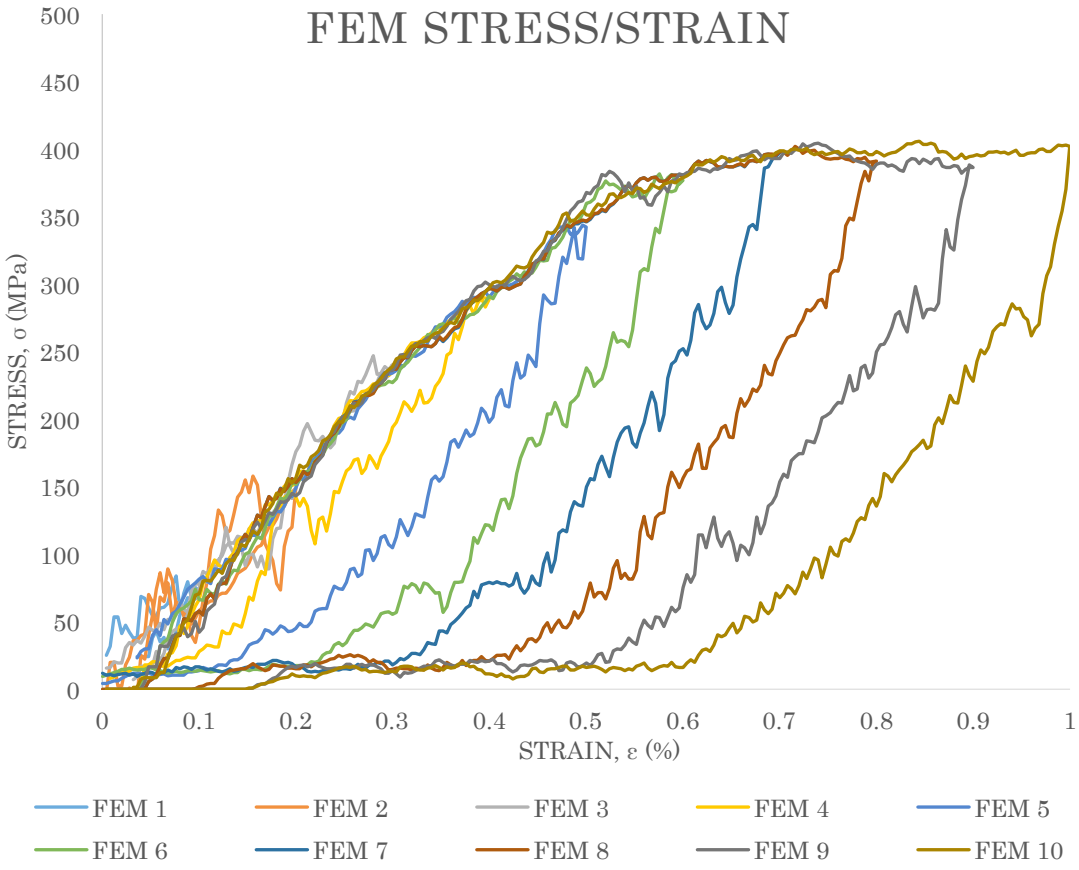

Figure 5.4: *FEM response under thermo-mechanical cycling*

Table 5.5 indicates values for stress obtained from the parallel FEM and Experimental thermo-mechanical cycling studies at specified strain magnitudes under loading, and the calculated comparative percentage error. These values indicate that there is

good agreement between the two studies with differences ranging between -8.9% → +13.8%, with a median of +2.44%.

Table 5.5: FEM vs. Experimental results: Stress values under mechanical loading

	Strain %									
	0.1	0.2	0.3	0.4	0.5	0.6	0.7	0.8	0.9	1
FEM	66.8	147.9	214.5	305	340.4	370.7	395	403	410	416
EXP	73.4	146.4	198.2	279.9	298.9	347.1	380.3	401.6	413.7	429
%ER	-8.9	+1.0	+8.2	+8.9	+13.8	+6.7	+3.8	+0.3	-0.9	-3.0

One area the model is unable to compute is the stress or thermal conditioning effects that SMAs typically undergo – signified by the sudden shift of material response after the 17th cycle in the experimental study (Figures 4.1 to 4.1 in section 4.2). Instead, the model is apt at describing behaviour of an already conditioned specimen, which outputs a stable response over a thermal or mechanical cycling environment.

5.3.2.2 FEM: Constant strain temperature sweep

The second FEM study is dedicated to the evaluation of NiTi behaviour as it is subjected to constant strain temperature sweep type tests. The parameters employed for the model are depicted in

table 5.6. This corresponds to the parallel study conducted experimentally in section 4.4.

Table 5.6: Experimental variables employed for constant strain temperature sweep FEM study

Test Type	Strain Min→Max	Strain ramp rate	Temperature Min/Max	Temperature ramp rate
Constant Strain Temperature sweep	0%→1% (6 increments)	N/A	Rt →+25°C, +25°C→Rt (Sweep)	1 x 10^{-1} °Cs^{-1}

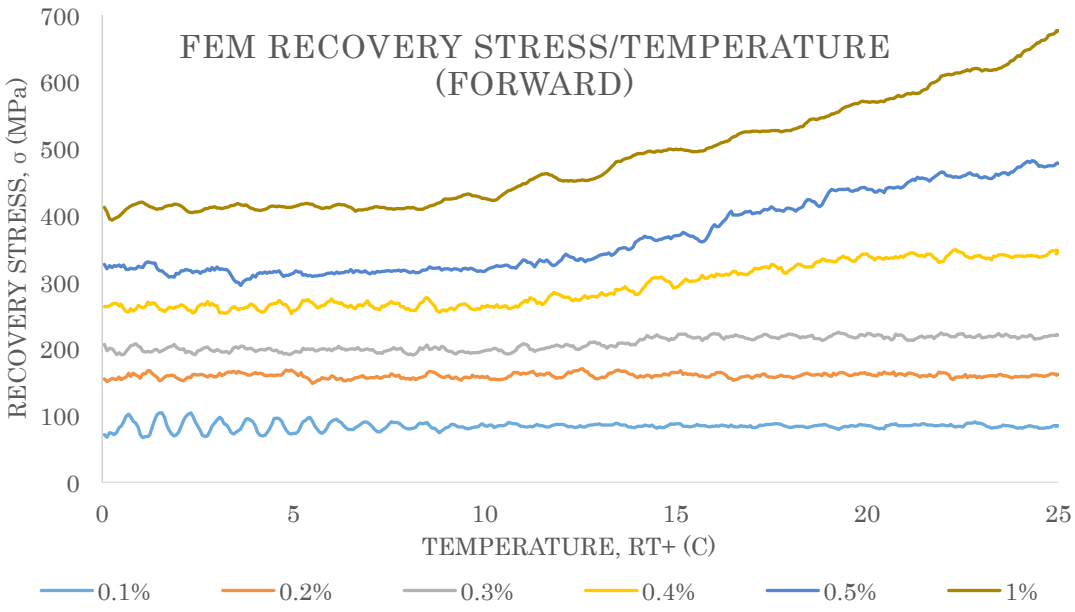

Figure 5.5: *FEM Recovery Stress as a function of Temperature for the forward temperature scan of Rt→+25°C at different strain magnitudes*

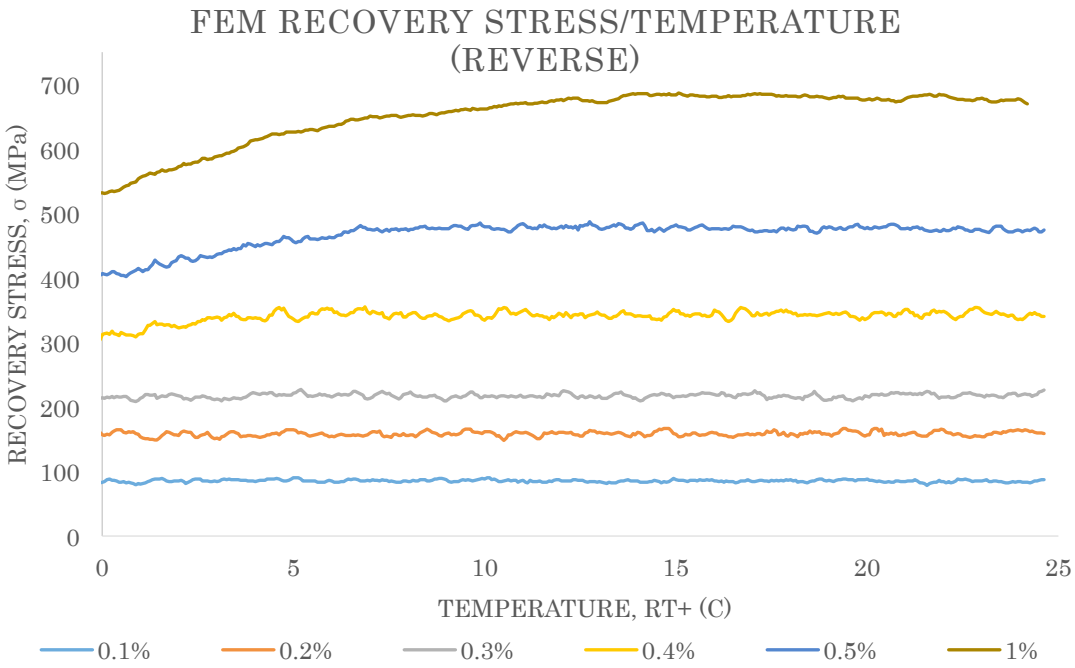

Figure 5.6: *FEM Recovery Stress as a function of Temperature for the reverse temperature scan of +25°C→Rt at different strain magnitudes*

The results from the temperature sweep study are depicted in Figure 5.5 and Figure 5.6, tracking the changes in recovery stress through a heating and cooling cycles respectively. The parallel experimentally obtained data is depicted in Figure 4.13 and Figure 4.14. This study highlights the impact of changes in temperature to the model response over an array of fixed strain magnitudes. At lower strain values which represent an elastic only deformation – 0.1%, 0.2%, 0.3% - there are negligible changes observed in the recovery stress in either the forward or reverse temperature sweeps. Responses with strain magnitudes past this point

demonstrate an increase in recovery stress with increases in temperature. A correlation can be drawn between this gradient - change in recovery stress/change in temperature – to the amount of de-twinning present at any given strain magnitude – the larger strain magnitudes produce responses with steeper dς/dt gradients. Moreover, this onset of increase in dσ/dt occurs at a lower temperature point with higher strain magnitudes.

The reverse temperature sweep demonstrates a different response characteristic. Most noticeably, the change in dσ/dt occurs at a much lower temperature point compared to the same occurrence in the forward temperature scan. This hysteresis can be credited to the difference between the Forward (M_f) and Reverse (A_f) transformation temperatures. As a result, the values obtained for Recovery Stress vary in accordance to their temperature loading history – values obtained with a forward temperature sweep are generally lower than parallel values obtained through a reverse temperature sweep.

This general behaviour compares favourably with the response observed through the parallel experimental study, as depicted in Table 5.7, which compares values for recovery stress between the two studies for tests conducted with a strain magnitude of 1%. For the purposes of this comparison, the FEM temperature of reference temperature corresponds to an experimental temperature of 25°C. The model struggles with values close to the reference temperature, due to its inability to vary dσ/dt significantly. As a result, the model is unable to simulate the spike in this value that occurs with the

forward and reverse martensitic transformation as detected in the experimental study. With higher temperatures, the FEM and experimental values converge, with the FEM data showing excellent correlation in the materials parent austenitic phase.

Table 5.7: Comparison of recovery stresses between FEM and experimental results under a static strain of 1%.

Temperature (°C)		Recovery Stress (Mpa)		
		FEM	EXP	%ER
Heating	Rt+10°C, 35°C	438.9	353.1	-24.2
	Rt + 15°C, 40°C	500.5	446.9	-11.9
	Rt+20°C, 45°C	571.2	593.2	+3.7
	Rt+25°C, 50°C	677.3	657.2	-3.0
Cooling	Rt+25°C, 50°C	688.2	696.1	+2.0
	Rt+20°C, 45°C	681.7	621.1	-7.1
	Rt + 15°C, 40°C	665.2	538.4	-16.5
	Rt+10°C, 35°C	627.5	449.4	-18.0

5.3.2.3 FEM: Constant temperature strain sweep

The final FEM study is dedicated to the evaluation of NiTi behavior as it is subjected to constant temperature strain sweep type tests. The parameters employed for the model are depicted in table 5.8. This corresponds to the parallel study conducted experimentally in section 4.3.

Table 5.6: Experimental variables employed for constant temperature strain sweep FEM study

Test Type	Strain Min→Max	Strain ramp rate	Temperature Min/Max	Temperature ramp rate
Constant temperature strain sweep	0%→1%, 1%→0% (Sweep)	1 x $10^{-4}s^{-1}$	Rt →+40°C (8 increments)	N/A

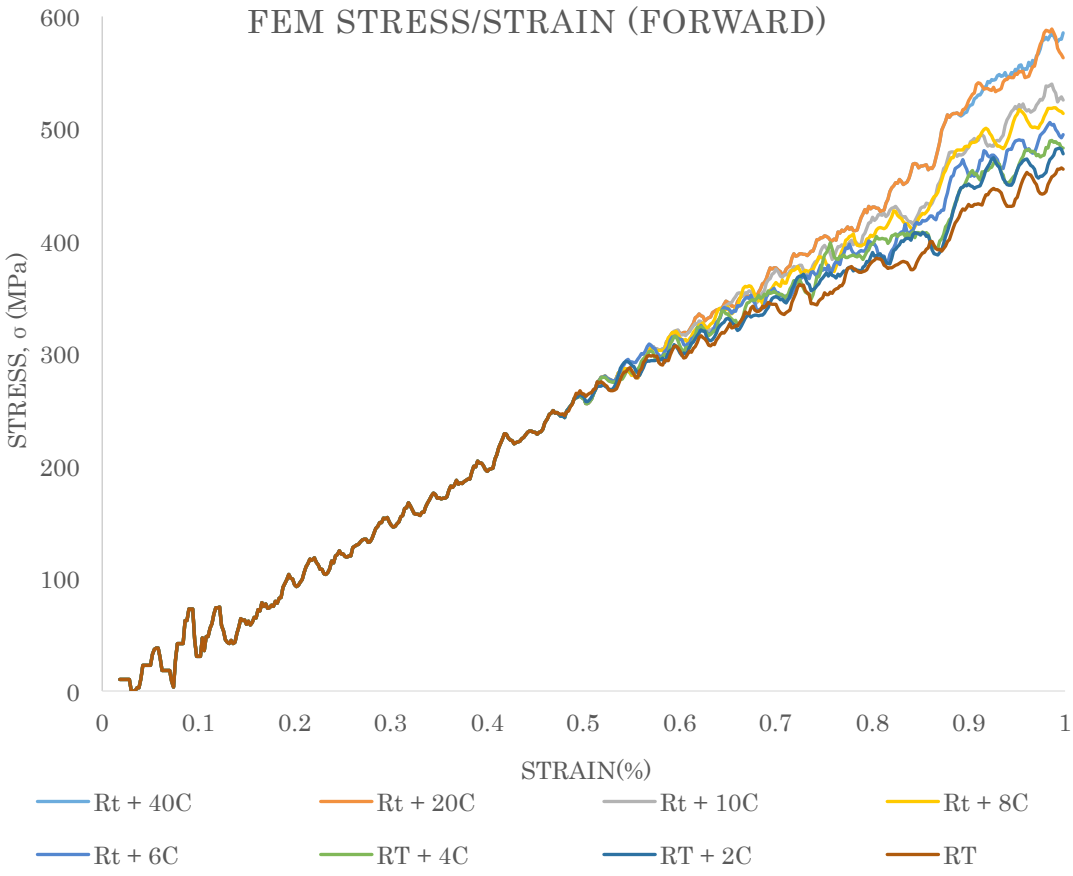

Figure 5.7: *Stress-Strain curves obtained with loading rate of $10^{-2}s^{-1}$ at different temperature magnitudes*

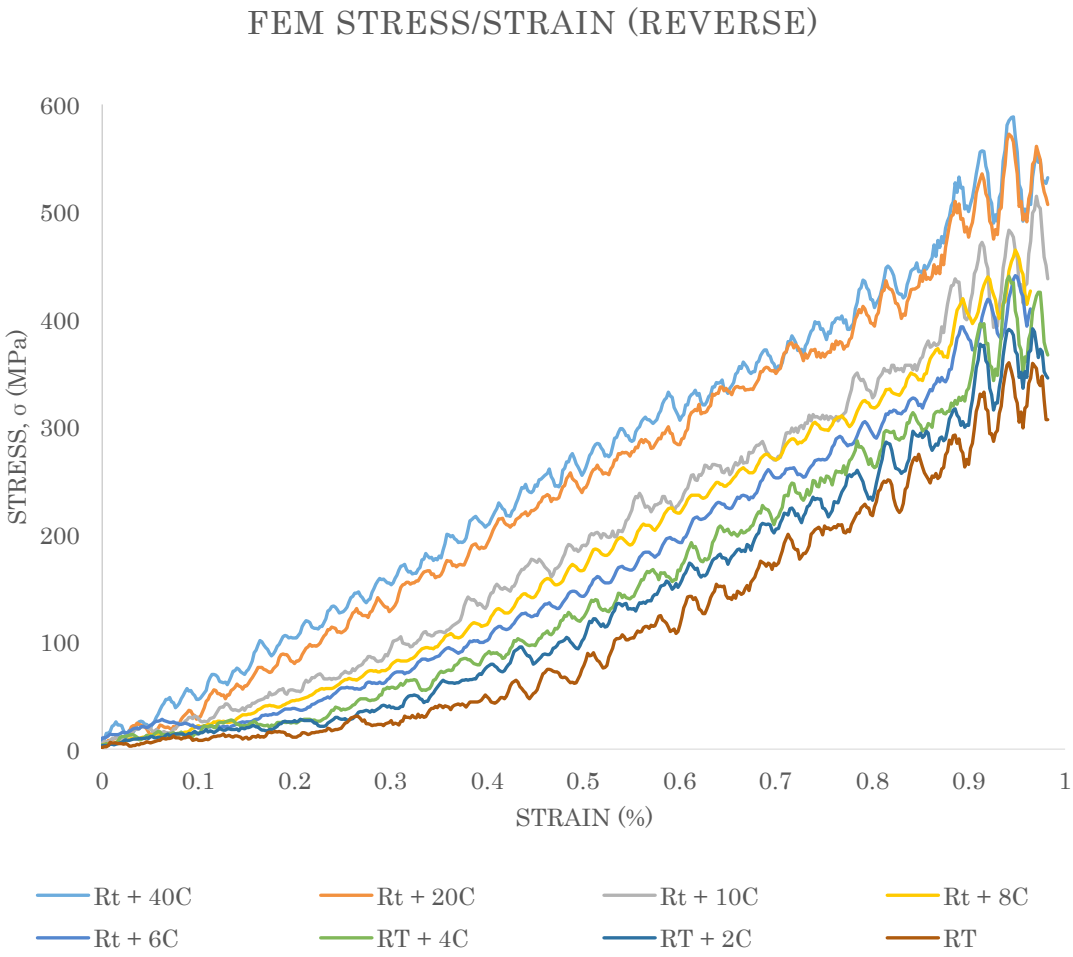

Figure 5.8: *Stress-Strain curves obtained with loading rate of $10^{-2}s^{-1}$ at different temperature magnitudes*

The results from the strain sweep study are depicted in Figure 5.7 and Figure 5.8. They highlight the impact of mechanical loading to the model response over an array of fixed temperatures. The same parameters were tested experimentally in section 4.2 and produced the results depicted in Figure 4.6.

During the loading period, the model outputs an identical response

up to a strain magnitude of 0.47% irrespective of the temperature condition. This point signifies the end of the elastic region in the material response at reference temperature. Further mechanical loading at this temperature condition results in drop in dσ/dε - the de-twinning period. The onset of this point is dependent on temperature, with this occurrence in the higher temperature runs of Rt+20°C and RRt+40°C not falling within the test strain envelope. The mechanical unloading characteristics are also dictated by the temperature condition the test is run at. While dσ/dε is similar across the temperature range, the lower stress value at the onset of unloading at lower temperatures (<Rt+10°C) result in a strain residual at zero stress.

One response characteristic that is not present in the loading/unloading sequence through FEM is the variance in the Tangent modulus from the onset of mechanical loading as exhibited in the parallel experimental study. Replication of this behaviour through FEM entails the start of transformation loading to occur simultaneously with the start of loading – which results in an unstable material response. Instead, to match this response as closely as possible, a low value of 100N is selected for this material parameter.

5.4 FEM Concepts

As the comparative study has determined the capability of the FEM model to provide an accurate map of SMA behaviour, the

subsequent step is using these fundamentals towards the development of SMA-based concepts. This section is dedicated to the presentation of the design and operative aspects of two FEM derived SMA based actuators that exploit contrasting deformation application/recovery philosophies: (Section 5.4.1) one-dimensional tension based and (Section 5.4.2) two-dimensional flexure based SMA-Actuators.

The common aim of the actuator concepts is to replicate the behaviour of a gas turbine engine Variable Stator Vane. This entails satisfying the operational requirement of providing an adequate angular displacement to redirect airflow as necessitated by the gas turbine engine. The two SMA based actuators employ an opposing actuator philosophy that provides faster de-activation periods and offers multiple degrees of tip-deflection. The non-NiTi sections of the concept structures demands a material outputting a highly elastic response characteristic (so it can withstand high strain mechanical load cycling - similar to superelastic SMA) and demonstrate a low rigidity at the same time (so it does not adversely affect actuator performance). Silicone-rubber is chosen for this purpose as it meets these requirements and brings additional benefits through its high chemical and thermal stability, and its ability to operate at elevated temperatures without damage. Table 5.7 specifies the material parameters employed in ABAQUS to simulate Silicone-Rubber behaviour.

Table 5.7: Material Properties assigned for non-NiTi structure in Actuator Concepts.

Material Name	Density (Tonne/mm^3)	Young's Modulus (Mpa)	Poisson's ratio
Silicone-Rubber	1.1 x 10^{-9}	1,500	0.47

Similar to previous FEM models, this study employs several measures to optimise computational resources: (1) *Z-axis symmetry* is applied as a boundary condition constraint, (2) all model parts are 1mm thick in the Z-plane (3) all non-NiTi model parts are meshed to an element size of 1mm^3, (the NiTi plates are meshed with a thickness of three elements in the Y-plane) and (4) the central plane in the Y-axis has a *Pinned* boundary condition constraint applied.

A temperature type boundary condition controls individual activation/deactivation of each NiTi plate. The models are specified with two types of contact properties in the ABAQUS interaction module: (1) A penalty type tangential behaviour with a frictional coefficient of 0.3 which is applied as a global model behaviour, and (2) Normal behaviour that restricts separation after contact, is applied to the surfaces of the attachment points. The NiTi plates in each system measure 30mm x 1mm x 1mm.

5.4.1 Pull: Tension based SMA actuator

The concept, as illustrated on Figure 5.9, is based on a one-dimensional deformation application/recovery system. It consists of two *linear actuators* (NiTi Plates -green), which are pre-strained in the X-plane and attached to the silicone-rubber central structure (red) at opposing sides.

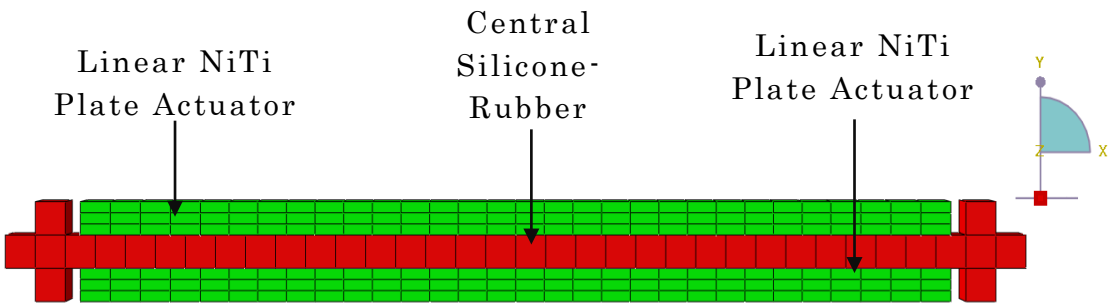

Figure 5.9: *ABAQUS model assembly replicating one-dimensional Actuator Concept (before application of pre-strain)*

The actuation mechanism can be described as follows. As the NiTi plate is thermally activated at its austenitic phase, it is shortened as strain is recovered. This creates a difference in lengths between the activated and strain limited non-activated side. To counteract this unbalanced environment, the whole structure bends, with the activated NiTi plate occupying the inner radii. The de-activated NiTi plate, which is at the onset of its stress plateau due to pre-straining, yields to become the outer radii of the structure. This

actuation mechanism forms the principles for many artificial muscle-type actuators.

5.4.2 *Push:* Flexure based SMA actuator

This concept, as illustrated on Figure 5.10, is based on a two-dimensional deformation application/recovery system. It consists of two *flexural actuators* (NiTi plates), which are pre-strained in the X-plane and Y-planes (through squashing the NiTi plates together) and attached to the silicone-rubber central structure at opposing sides.

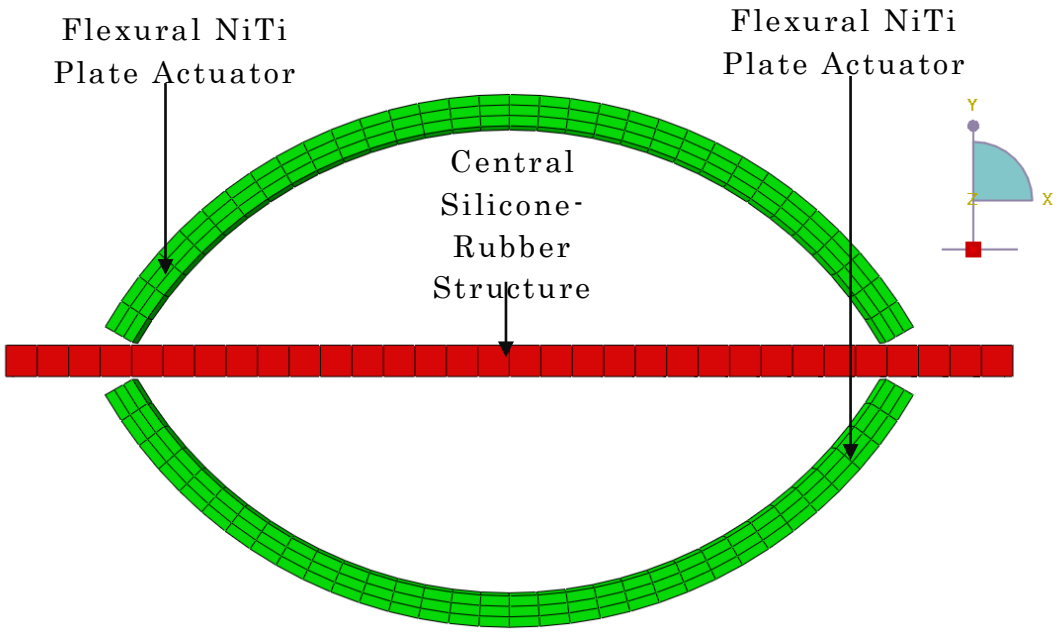

Figure 5.10: *ABAQUS model assembly replicating two-dimensional Actuator Concept (before application of pre-strain)*

In comparison to the Tension based solution, this employs a much simpler actuation mechanism. Strain recovery occurs as the NiTi plate is thermally activated at its Austenitic phase. The high stiffness modulus of the parent phase overwhelms and forces the remaining parts in the structure – consisting of the lower stiffness Silicone-Rubber central structure and deactivated NiTi plate on the opposing side which is in its martensitic phase and at the onset of its stress plateau due to pre-straining - to adapt a similar shape to the activated NiTi plate.

5.5 FEM Analysis of SMA Concepts

The advantages of using FEM techniques in conceptualisation and consequent evaluation tasks has been highlighted in previous sections. This comparative study utilises FEM to locate, report and evaluate the operational merits and drawbacks of the two VSV actuator concepts presented in Section 5.4.

Response characteristics of the actuator concepts are evaluated in three significant operating states: (1) The neutral state - Section 5.5.1, (2) The activated state - Section 5.5.2, (3) The deactivated state - Section 5.5.3. The relative performance of the actuators are comparatively analysed through the tracking of: (1) Temperature Vs. Deflection response - Section 5.5.4, and (2) Strain vs. Deflection response - (Section 5.5.5).

Observable parameters include outputs specific to the SMA UMAT: (1) Strain: *SDV24* (Equivalent uniaxial tensile total strain), (2) Stress: SDV22 (Equivalent uniaxial tensile stress), (3) Fraction of martensite: SDV21, and general ABAQUS outputs: (4) Temperature: TEMP, Deflection: U, MAGNITUDE.

5.5.1 The Neutral state

This section is dedicated to the comparative analysis of the two-actuator concepts at their neutral states. This condition is met following the application of pre-strain on the NiTi plate, and prior to any temperature input. Figures 5.11 to 5.16 illustrate the localised strain, stress and martensite fraction distribution at this condition for the two concepts.

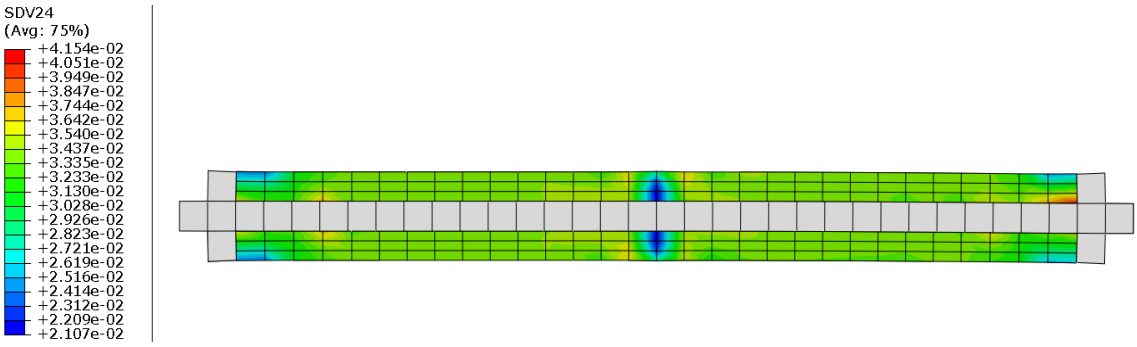

Figure 5.11: *ABAQUS representation of strain distribution of one-dimensional Pull model at a neutral state*

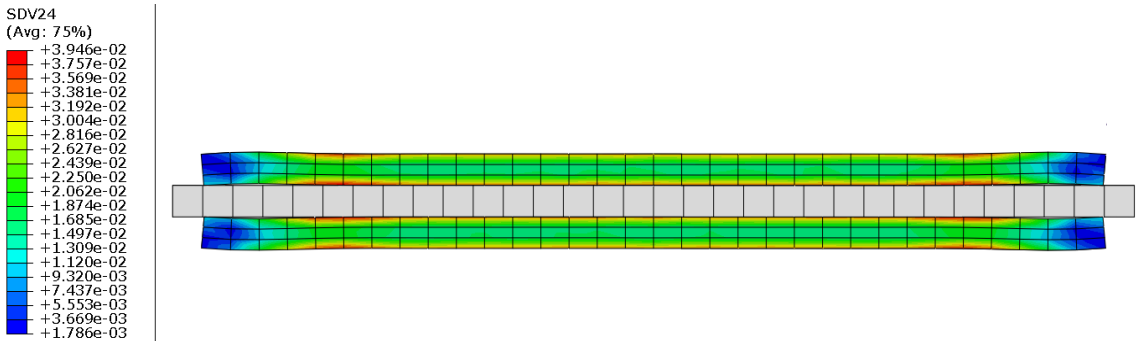

Figure 5.12 *ABAQUS representation of strain distribution of two-dimensional Push model at a neutral state*

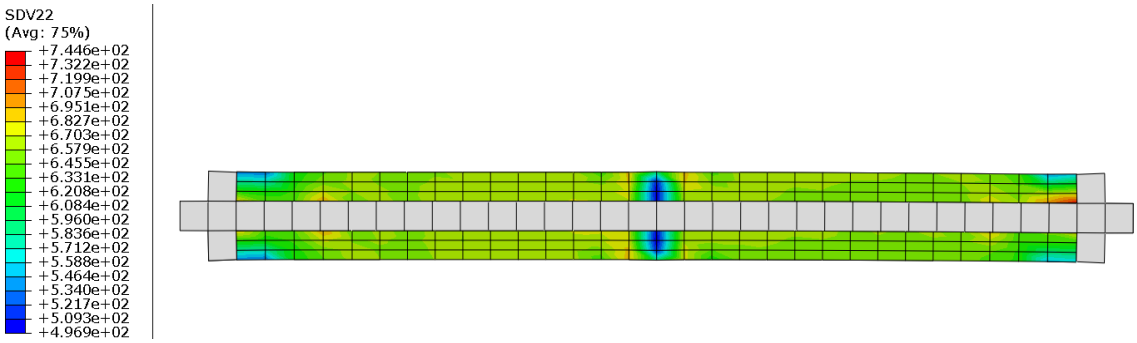

Figure 5.13: *ABAQUS representation of stress distribution of one-dimensional model Pull at a neutral state*

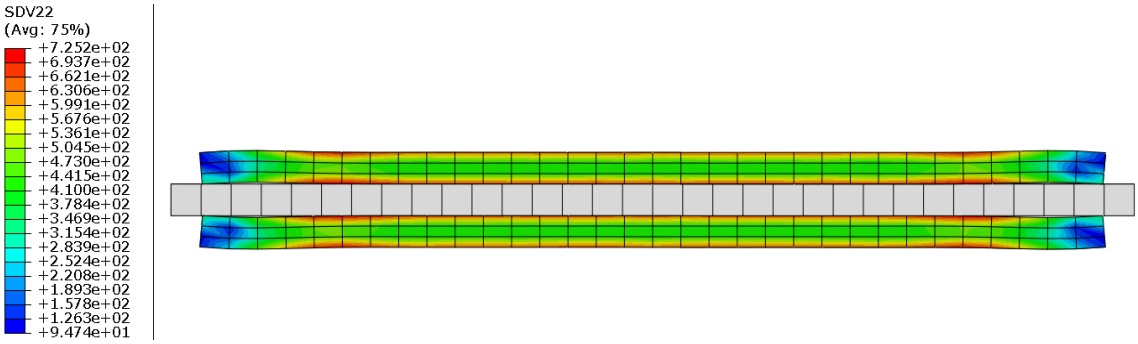

Figure 5.14: *ABAQUS representation of stress distribution of two-dimensional model Push at a neutral state*

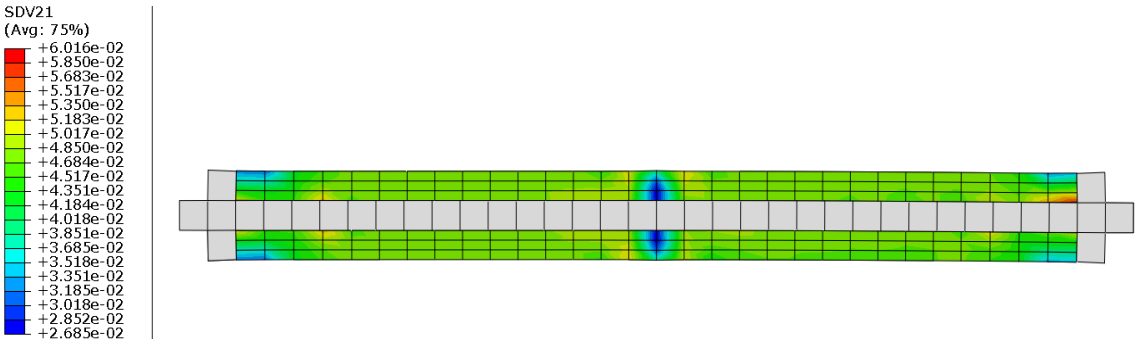

Figure 5.15: *ABAQUS representation of martensite fraction distribution of one-dimensional Pull model at a neutral state*

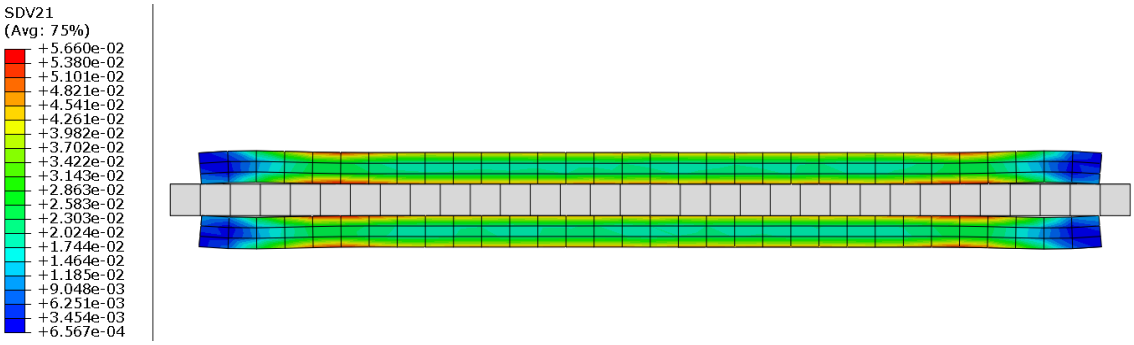

Figure 5.16: *ABAQUS representation of martensite Fraction Distribution of two-dimensional Push model at a neutral state*

The maximum magnitudes recorded for strain and stress at the neutral state is quite comparable between the two concepts: an average difference of only 3.96% is observed. However, the adaption of distinct NiTi plate profiles and application of contrasting methods of pre-strain result in vastly different distributions for each of these parameters. This distribution of Stress/Strain is overwhelmingly saturated towards the edges in

the *Pull* concept (which is subject to tensile and compressive forces as a result of flexure). The *Push* concept on the other hand, through its use of a one-dimensional pre-strain application, demonstrates a much more even Stress/Strain distribution – with the exclusion of one dead spot in deformation, observed half-way along the NiTi plate, due to this point being *Pinned* to the central structure.

A pre-requisite of the neutral state is to provide a suitable platform for subsequent activation. This entails retention of an adequate pre-strain loading the NiTi plate towards the onset of the strain plateau in its stress/strain material response curve. Whether this has been successfully accomplished can be observed through scanning the martensite fraction distributions, depicted in figures 5.21 and 5.22. As the *Pull* model was superior in its uniformity of pre-strain application, it is able to boast a broader presence of martensite Fraction. The *Push* model, on the other hand, has observable dead spots towards the ends of the NiTi plates.

5.5.2 The Activated state

Following the neutral step, a thermal boundary condition is specified on one NiTi plate, increasing its temperature from RT → RT + 50°C. The activated state is reached upon the completion of

this step. This section is dedicated to the comparative analysis of the two-actuator concepts at this *Activated* state. Figures 5.17 to 5.22 illustrate the localised Strain, Stress and martensite fraction distribution at this condition for the two concepts.

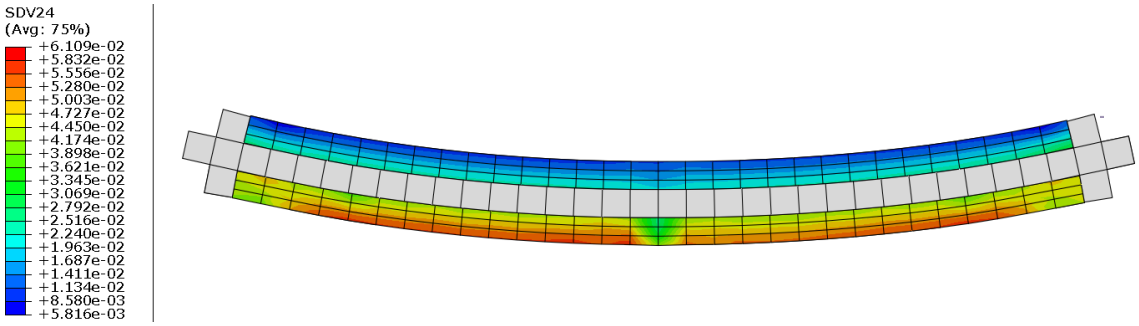

Figure 5.17: *ABAQUS representation of Strain Distribution of one-dimensional Pull model at Activated state*

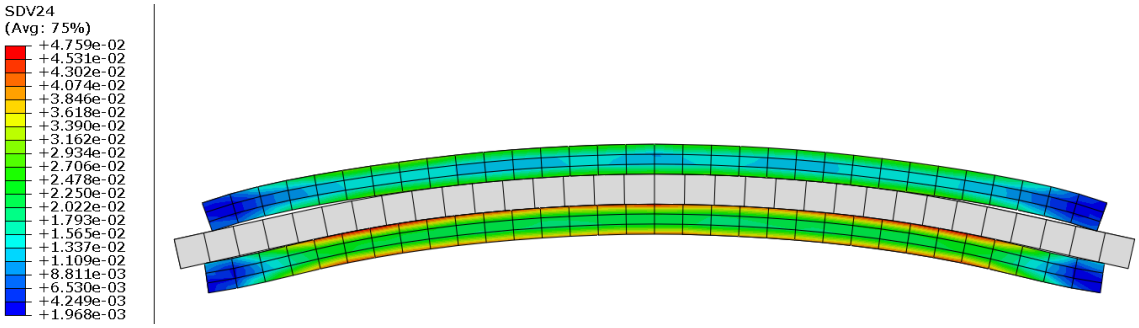

Figure 5.18: *ABAQUS representation of Strain Distribution of two-dimensional Push model at Activated state*

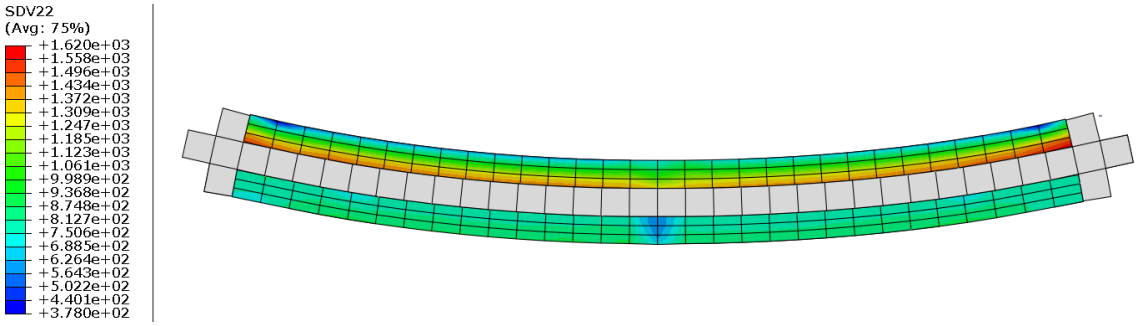

Figure 5.19: *ABAQUS representation of Stress Distribution of one-dimensional Pull model at Activated state*

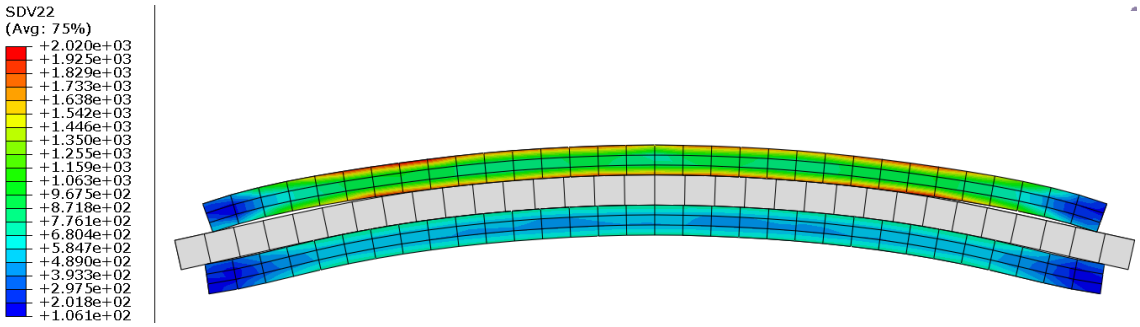

Figure 5.20: *ABAQUS representation of Stress Distribution of two-dimensional Push model at Activated state*

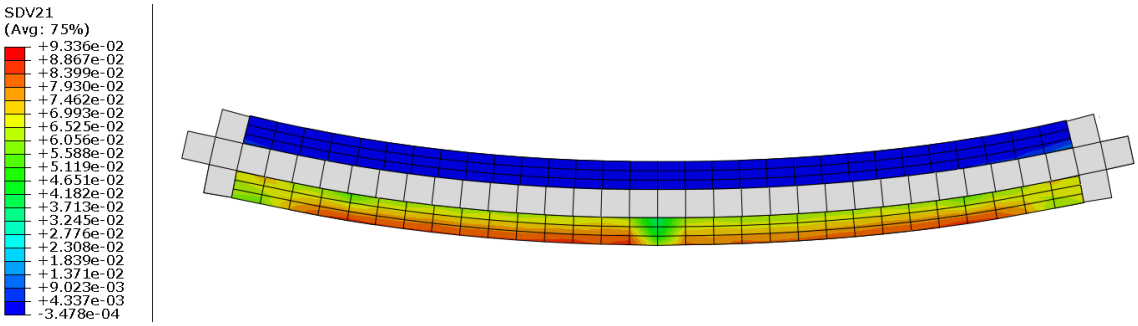

Figure 5.21: *ABAQUS representation of martensite Fraction Distribution of one-dimensional Pull model at Activated state*

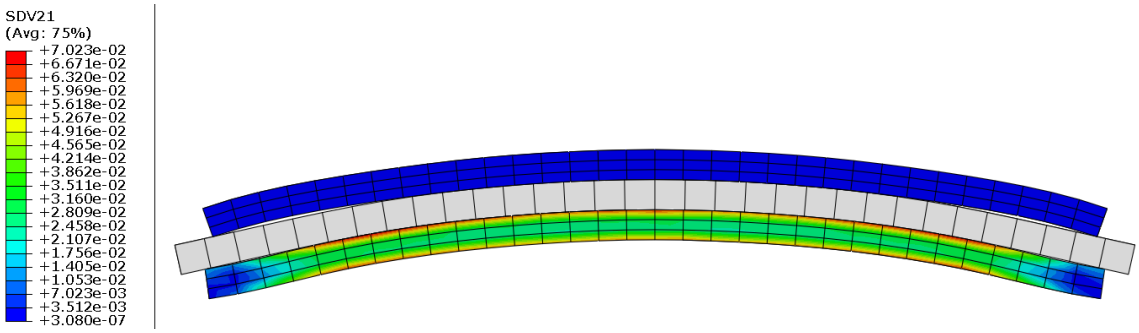

Figure 5.22: *ABAQUS representation of martensite Fraction distribution of two-dimensional Push model at Activated state*

As suggested by the concept names, activation of the NiTi plate in the *Push* and *Pull* concepts results in opposing directions of tip deflection. This is a direct result of the differences between the NiTi plate profiles and the pre-straining mechanisms.

At the activated state, the one-dimensional *Pull* concept is able to boast a higher maximum strain value (28.15% higher) whilst demonstrating a lower maximum stress value (19.80% lower). This underlines the efficiency of the one-dimensional concept; it requires less effort to drive the same amount of deformation in comparison to the two-dimensional concept. The fraction of martensite present demonstrates a similar outcome – the one-dimensional *Pull* model is able to generate a larger degree of martensite transformation at the non-activated plate (32.90% more than two-dimensional *Push* model).

However, observing the distribution of Strain, Stress and

martensite fraction of the one-dimensional model reveals a strong localisation on the outer plane of the non-activated plate. A less prominent concentration of the distribution is observed in the two-dimensional concept, on the inner plane of the non-activated plate. From a theoretical point of view, such localisation is detrimental to the performance of an actuator from operational standpoint, as the increased maximum stress/strain values decrease the lifespan and cyclic consistency.

5.5.3 The De-activated state

The thermal boundary condition subsequently specifies a reduction in the temperature of the Activated NiTi plate from RT + 50°C → RT. The model has now reached its De-activated state. This section is dedicated to the comparative analysis of the two-actuator concepts at this *De-activated* state. Figures 5.23 to 5.28 illustrate the localised Strain, Stress and martensite fraction distribution at this condition for the two concepts.

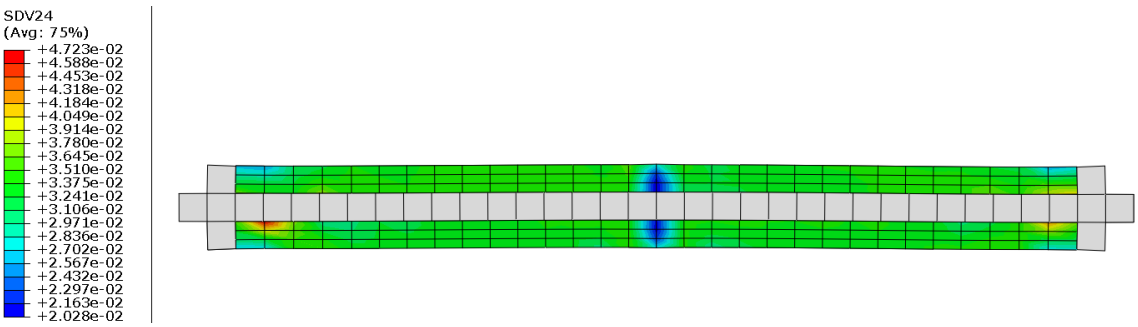

Figure 5.23: *ABAQUS representation of Strain Distribution of one-dimensional Pull model at De-activated state*

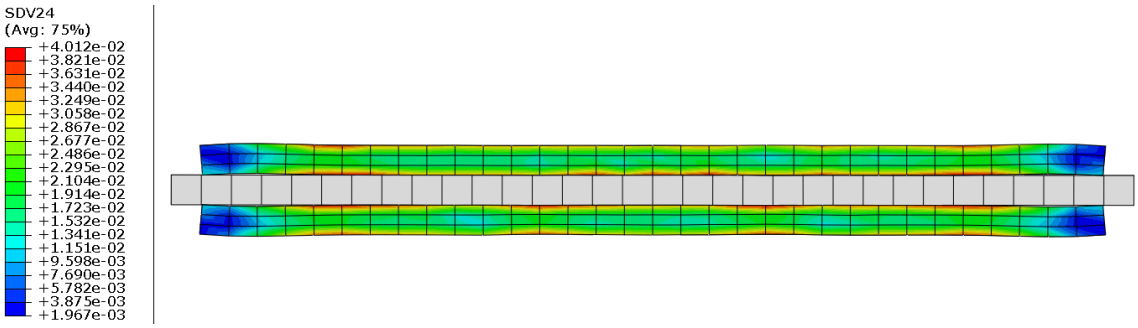

Figure 5.24: *ABAQUS representation of Strain Distribution of two-dimensional Push model at De-activated state*

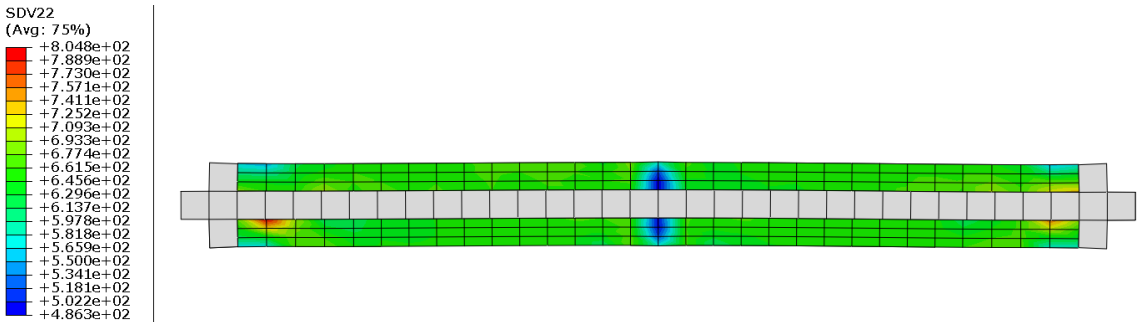

Figure 5.25: *ABAQUS representation of Stress Distribution of one-dimensional Pull model at De-activated state*

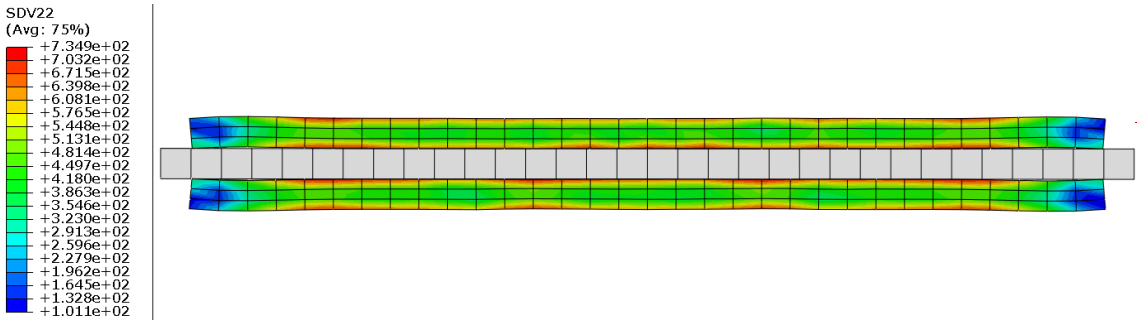

Figure 5.26: *ABAQUS representation of Stress Distribution of two-dimensional Push model at De-activated state*

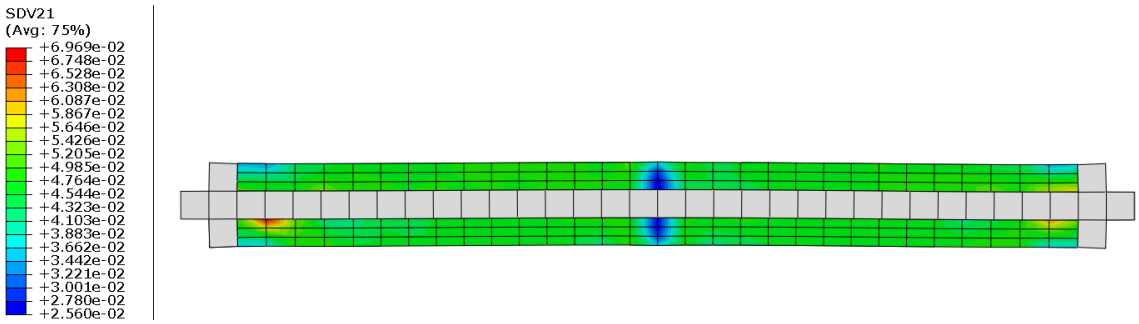

Figure 5.27: *ABAQUS representation of martensite Fraction Distribution of one-dimensional Pull model at De-activated state*

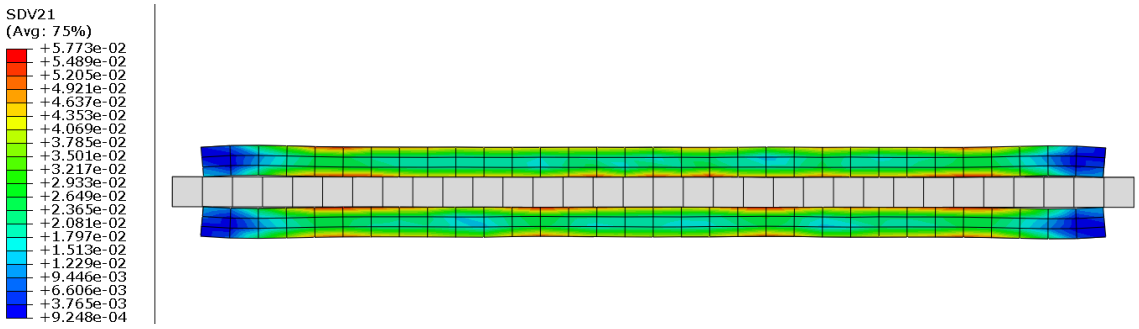

Figure 5.28: *ABAQUS representation of martensite Fraction distribution of two-dimensional Push model at De-activated state*

The core requirement of the de-activated state is to recover deformations generated through previous thermal loading. While the temperature is identical to that of the neutral state, there are observable differences between the Strain, Stress and martensite fraction magnitudes and distributions for both concepts. This occurrence can be attributed to the thermal and mechanical loading

subjected to the NiTi plate in prior steps: SMAs are very sensitive to occurrences of such load-history. This has manifested as an increase in peak strain (*Pull*: 12.07%, *Push*: 1.74%), an increase in peak stress (*Pull*: 7.46%, *Push*: 1.33%), and an increase in peak martensite fraction (*Pull*: 15.80%, *Push*: 1.94). The substantial increase in these peak values in the one-dimensional *Pull* model, is linked with the growth of a hotspot of deformation localisation at the upper left-side edge of the bottom NiTi plate. Such appearances of hotspots, particularly such early in the loading cycling, can develop into inconsistencies of the material response in subsequent cycles.

5.5.4 Temperature Vs. Deflection response

The actuation performance of each of the concepts can be assessed through the magnitude of deflection they are able to develop upon thermal activation. This response has been tracked in Figure 5.29 for the thermal Activation, and Figure 5.30 for the thermal de-activation of each opposing actuator for the two concepts. Deflection and Temperature values were obtained tracking the ABAQUS outputs: U2 at the NiTi plate tip, and TEMP at the activated plate.

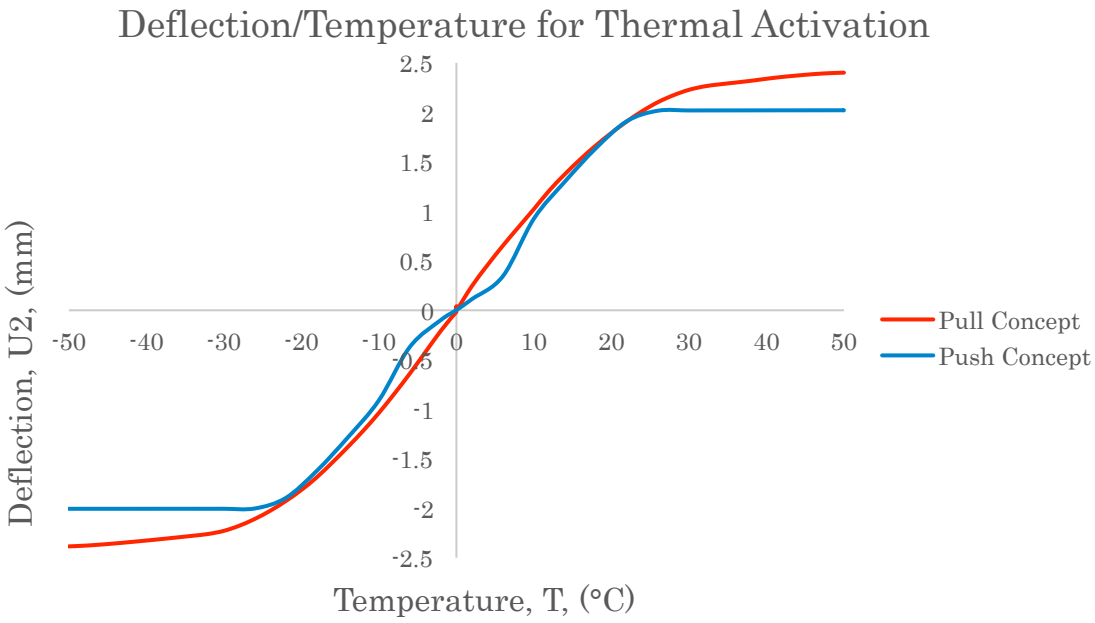

Figure 5.29: *Deflection/Temperature response of Pull Concept (red) and Push Concept (blue) as a result of thermal activation.*

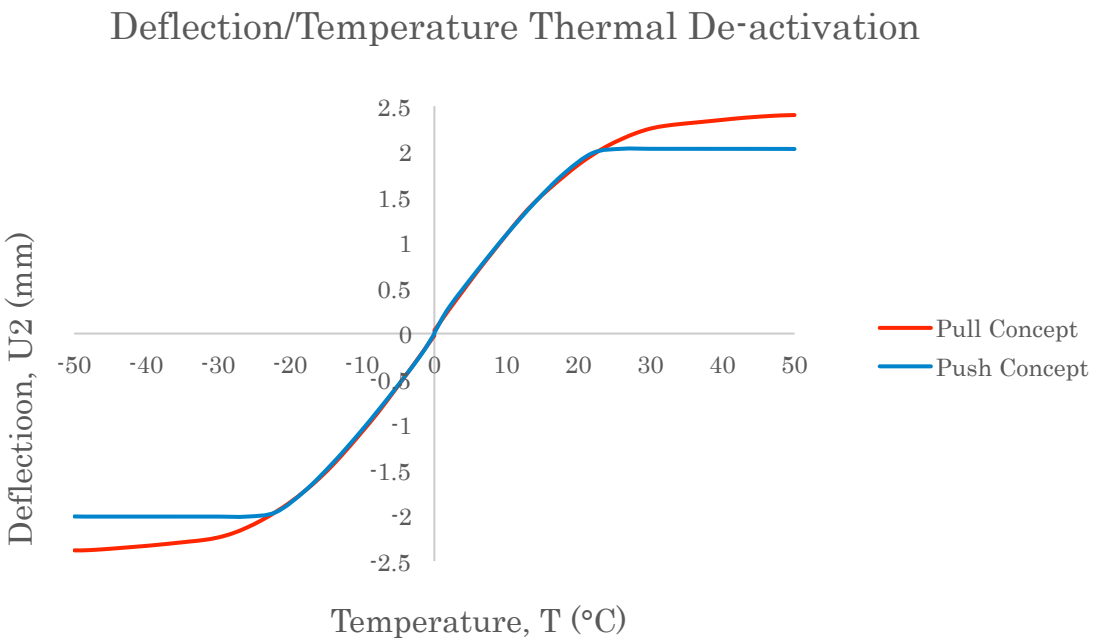

Figure 5.30: *Deflection/Temperature response of Pull Concept (red) and Push Concept (blue) as a result of thermal deactivation*

The most evident observation is the *Pull* concepts ability to generate a larger degree of tip deflection: (2.4mm as opposed to 2.0mm of the *Push* concept). This was an expected outcome, as indicated in the previous study of the activated state, where this concept demonstrated larger strain values. The two concepts demonstrate a similar deflection/temperature gradient during activation and de-activation. Due to the deflection magnitudes being smaller on the *Push* concept, it is able to reach its fully activated state sooner.

Moreover, the *Push* concept follows a non-linear response in the initial stages of thermal input as it is activated. This can be considered as a positive behavioural characteristic in the context of an actuation application: the concept is capable of tolerating small un-intentional temperature inputs without generating large magnitudes of deflection. This characteristic is however not observed through thermal de-activation.

5.5.5 Strain Vs. Deflection response

The actuation efficiency of each of the concepts can be assessed through the magnitude of strain necessitated to achieve a target deflection magnitude. This response has been tracked in Figure 5.31 and Figure 5.32 for the thermal activation of each opposing actuator for the two concepts respectively. Deflection and strain values are obtained by tracking the ABAQUS outputs U2 and NiTi plate tip, and SDV24 at the centreline of the respective plate (SMA UMAT specific output: Equivalent uniaxial tensile total strain).

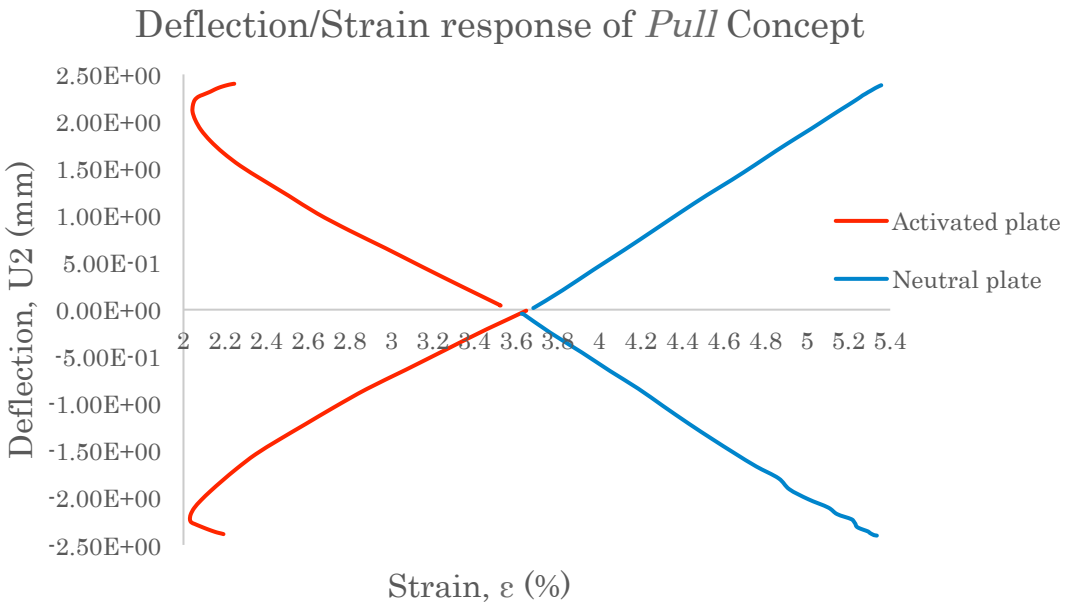

Figure 5.31: *Deflection/Strain response of Pull as a result of thermal activation*

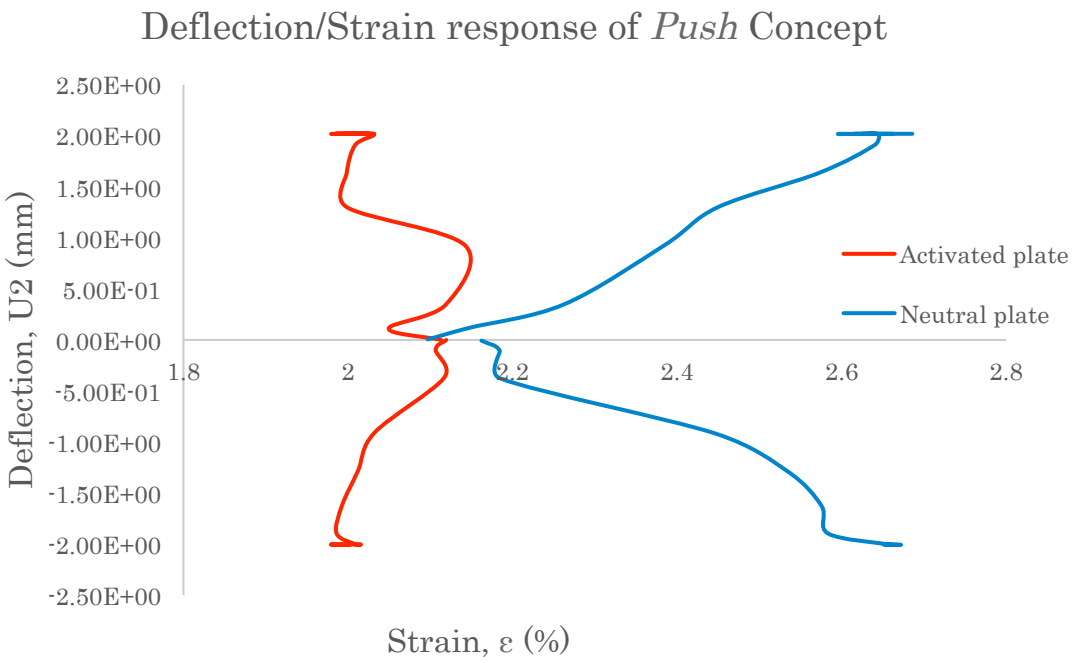

Figure 5.32: *Deflection/Strain response of Push Concept as a result of thermal de-activation*

The two concepts demonstrate stark differences in their response under the aforementioned criteria. At the neutral state, with zero deflection, the *Pull* concept applies a pre-strain in the region of 3.6% compared to only 2.1% for the push concept. While this means that more energy is stored on the *Pull* concept, this comes at the expense of a higher strain envelope that limits operating life cycles.

As actuation is based on the fundamentals of the SME, the strain recovery of the activated plate consequents in further deformation of the neutral plane. Whilst this behaviour is quite linear in the one-dimensional Pull concept, the two-dimensional push concept suffers from a very unconventional deflection/strain relationship. One consolation is, however, that the operating strain envelope of the *Push* concept is much narrower, and generally lower in magnitude in comparison to the *Pull* concept. The *Push* concept operates at strains between 1.99% → 2.67% (a span of 0.68%), whereas the corresponding values for the *Pull* concept are 2.07% → 5.34% (A span of 3.27%). Moreover, the *Push* model exhibits a favourable behavioural characteristic in its deflection/temperature response that could help in avoiding unintentional actuation.

5.6 Solid-state SMA Flexural Actuator Concept

The merits and drawbacks of a one-dimensional pull type actuator and the newly devised two-dimensional push type actuator were evaluated in the comparative study. It can be argued that while both concepts demonstrated several favourable behavioural

characteristics, neither emerged as a clearly superior solution. One differentiating factor is the inherent simplicity of the two-dimensional *Push* models implementation – theoretically requiring no additional structure to induce actuation. Moreover, the *Push* model's utilisation of a flexural deformation mechanism aligns well with the experimental study.

As a result of these key factors, the same conceptual philosophy used in the *push* type actuator was adapted and further evolved towards the creation of a viable VSV actuation system. The resulting concept is presented in a pre-strained condition in Figure 5.33, and depicting an "exploded" view of the original NiTi plate profiles in Figure 5.34.

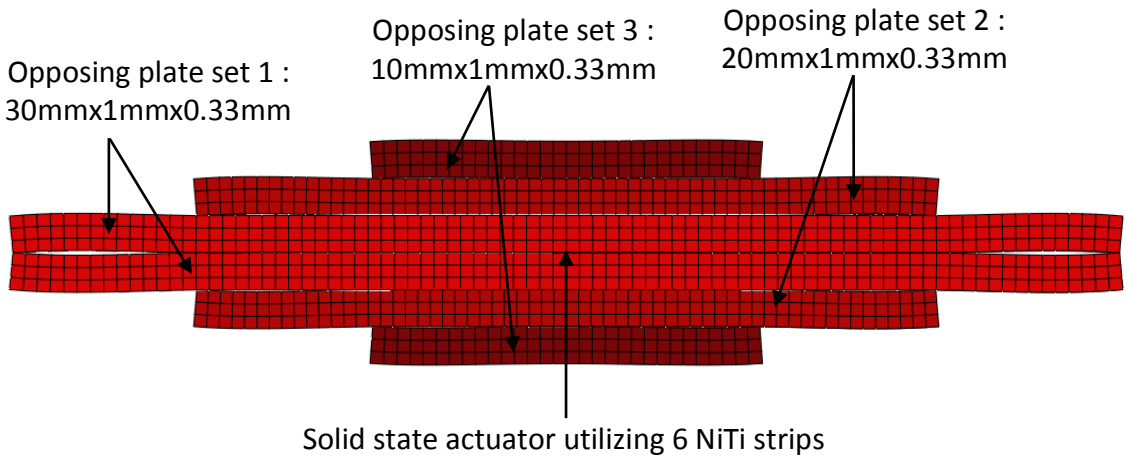

Figure 5.33: *Solid-State VSV actuator at prestrain condition*

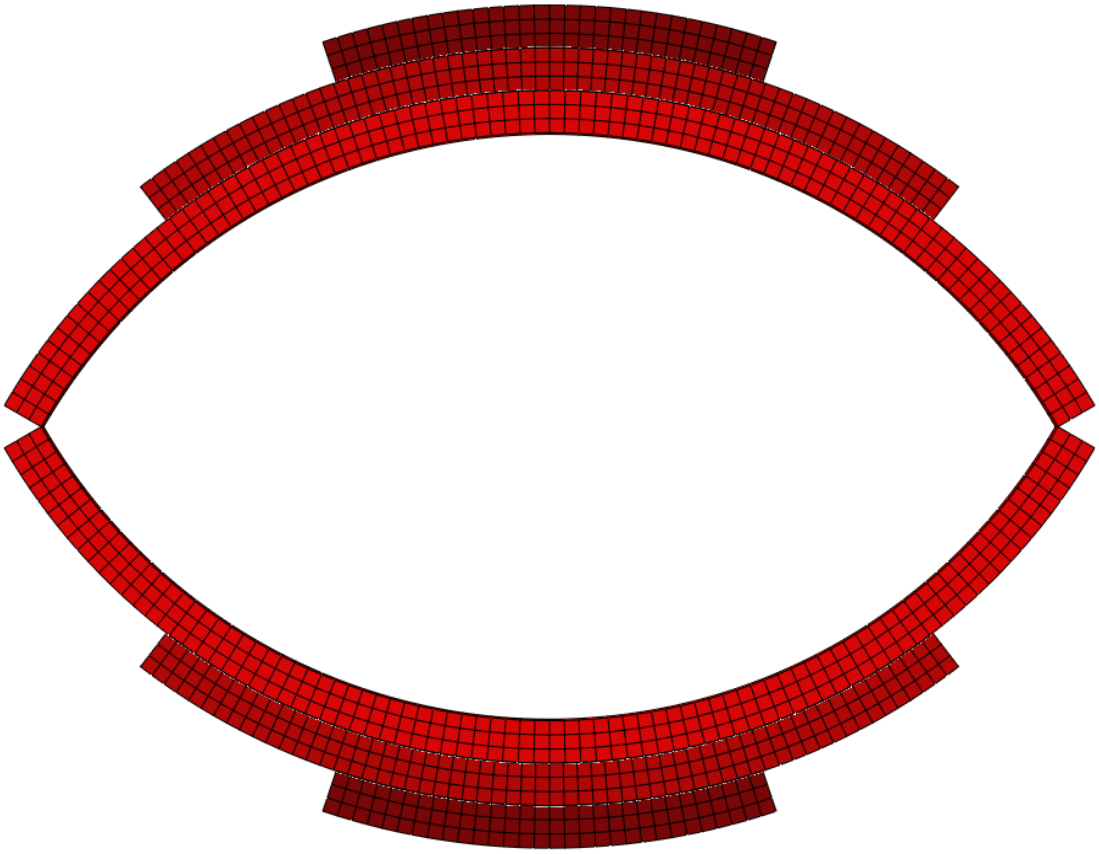

Figure 5.34: *Exploded view of Solid-State VSV actuator*

The solution can be categorised as a solid-state actuator as it contains no moving parts apart from the flexural actuators, which are load-carrying elements that determine the profile of the system. As a result, even faced with an actuator input failure event, the system is able to serve a purpose. The concept is able to boast a high specific performance, as it is energy dense with all parts geared towards delivering actuation. It also possesses a high damage tolerance, essential to any VSV application: it can experience partial mechanical failure but still be able to function, albeit at a reduced level.

The system consists of 6 NiTi plates arranged in a 3-3 configuration on opposing sides. The design incorporates plates of varying lengths - 30mm, 20mm and 10mm - to offer a range of strain recovery forces. Through the individual activation of the 6 NiTi plates, the system is able to boast 64 different tip deflection levels and morphing states.

The model was meshed in ABAQUS with an element size of $0.33mm^3$. As with all other FEM work, the model was constrained in the Z-axis and specified with a thickness of 1 element. The only additional boundary condition specified is that of a Pinned type through the centreline (Y direction).

Each actuation profile is activated through a specific thermal condition. The thermal conditions TC1 to TC64 are depicted through Figures 5.35 to 5.38. The left hand side of each diagram represents the activated plates (marked red). The right hand side shows the distribution of martensite fraction as a result of the thermal condition.

Figure 5.39 depicts the tip deflection magnitudes recorded at the inner, central and outer NiTi plate, for each of the transformation configurations (TC1→TC64). The assertion that the concept is able to provide a wide degree of morphing configurability is validated through this study. In a practical-space, this flexibility means that this system would be better suited to reacting to a gas turbine engine operating requirement compared to a conventional, hydraulically actuated VSV system.

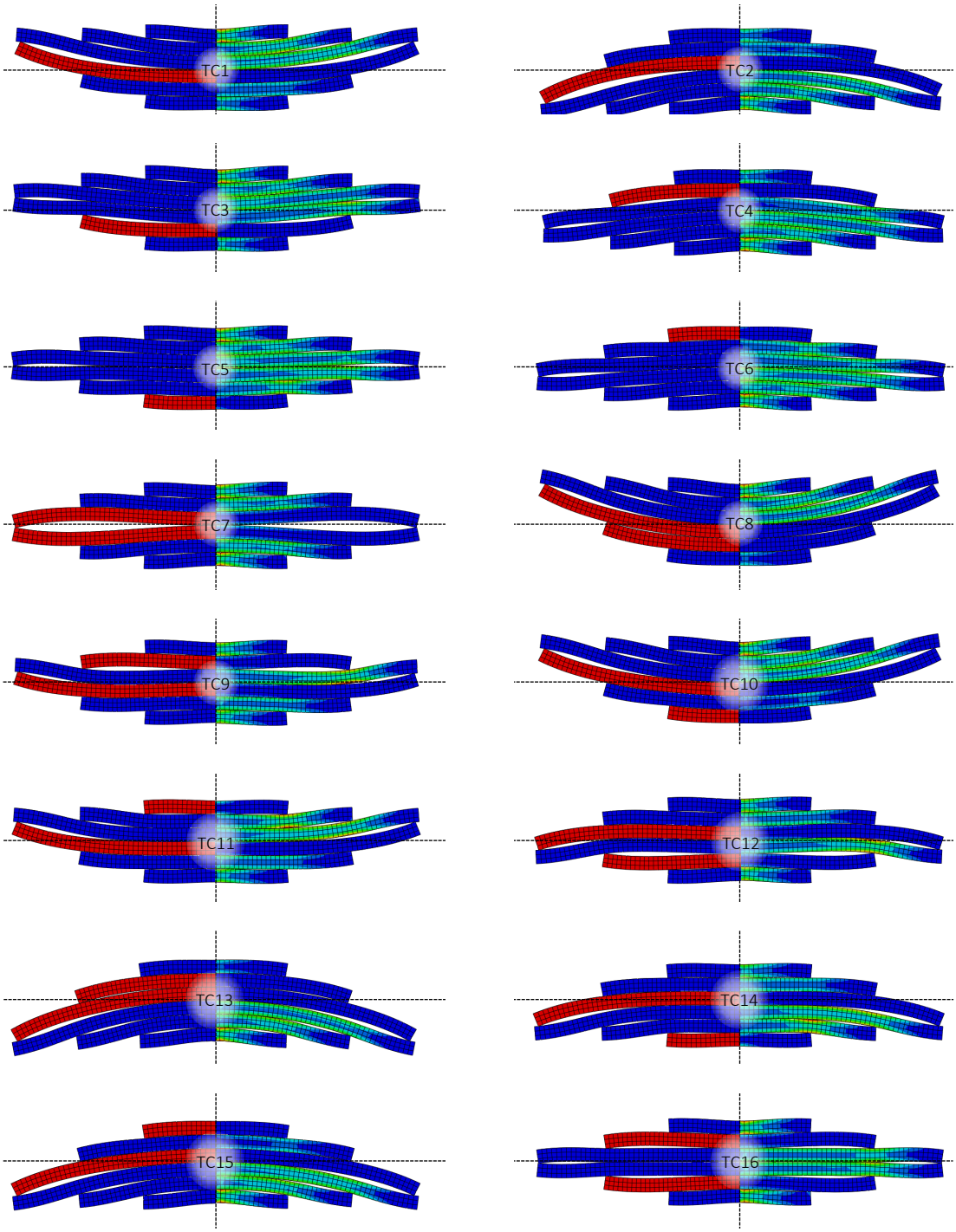

Figure 5.35: *VSV actuator morphed states under thermal conditions TC1->TC16 depicting LHS activated plates, RHS martensitic fraction*

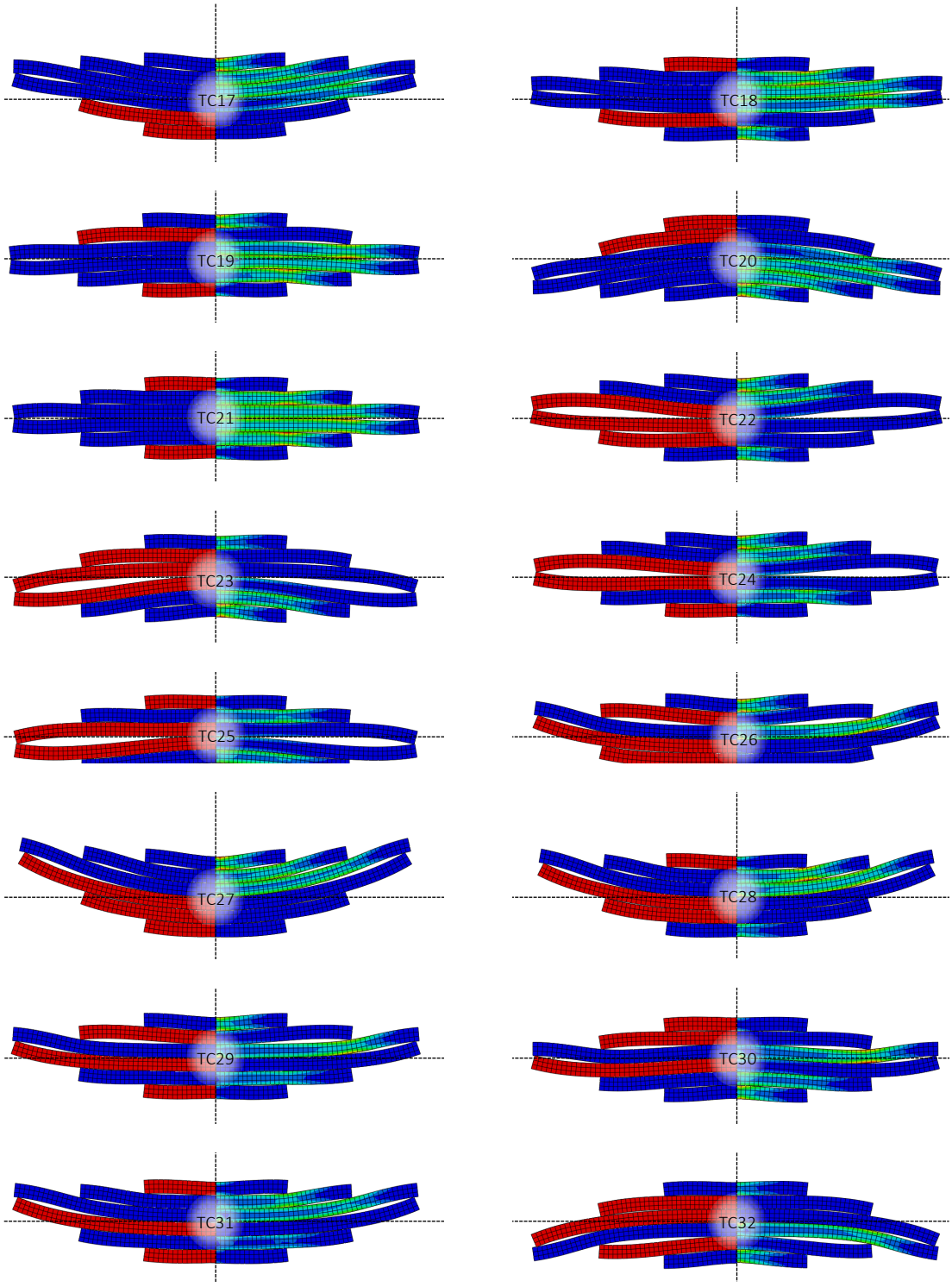

Figure 5.36: *VSV actuator morphed states under thermal conditions TC17->TC32 depicting LHS activated plates, RHS martensitic fraction*

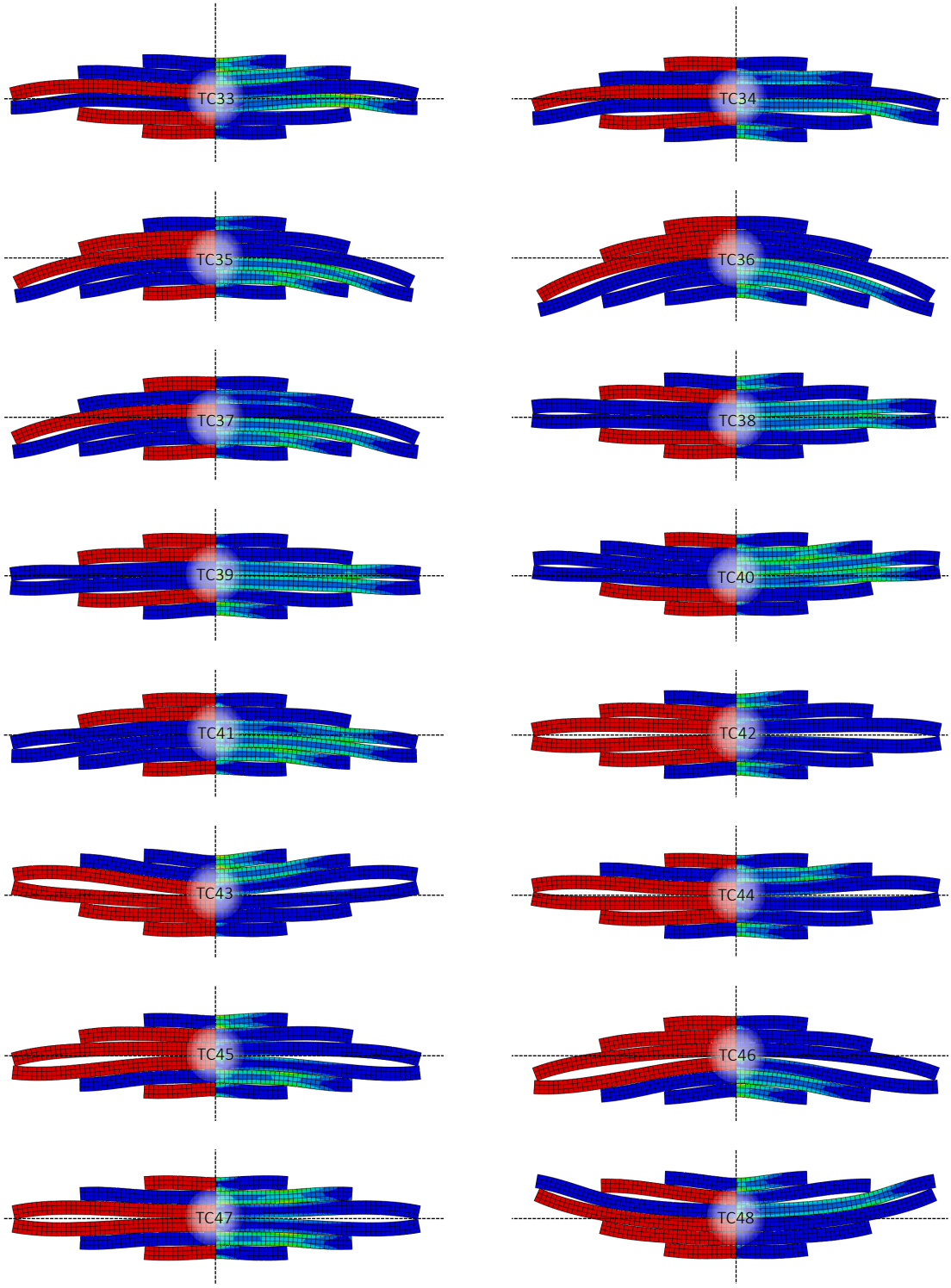

Figure 5.37: *VSV actuator morphed states under thermal conditions TC33->TC48 depicting LHS activated plates, RHS martensitic fraction*

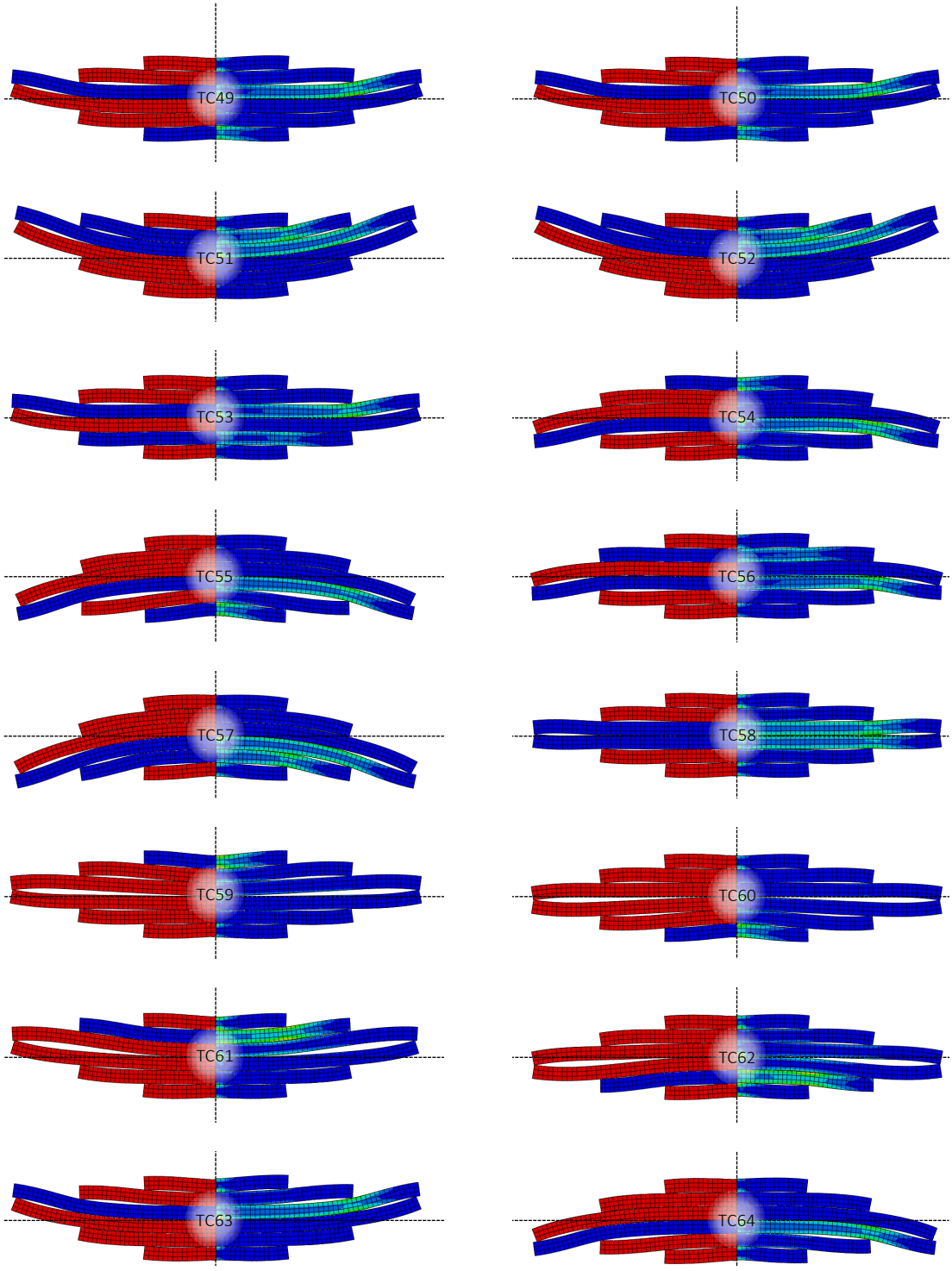

Figure 5.38: *VSV actuator morphed states under thermal conditions TC49->TC64 depicting LHS activated plates, RHS martensitic fraction*

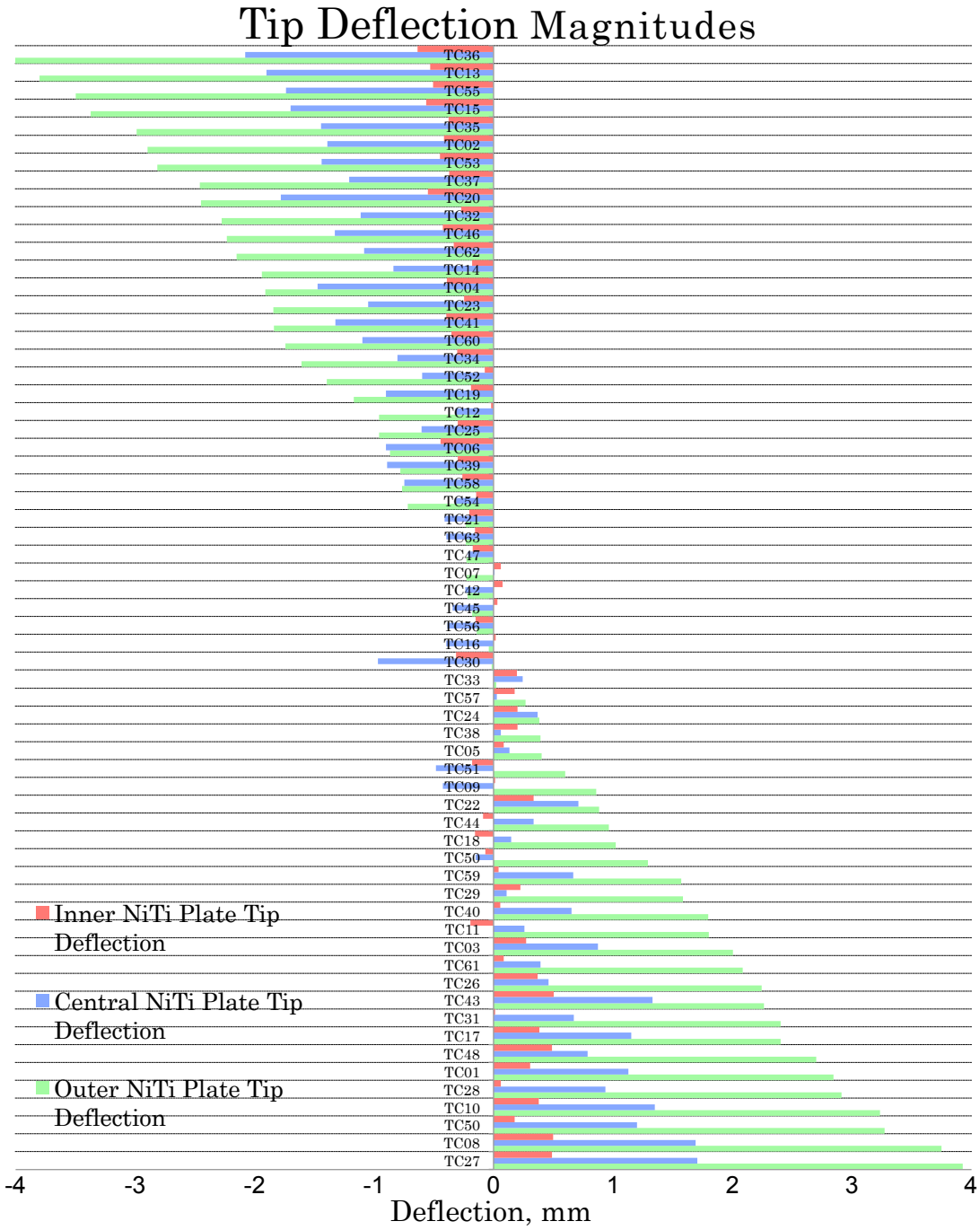

Figure 5.39: *Tip deflection magnitudes at inner NiTi plate tip (red), Central NiTi plate tip (Blue) and Outer NiTi plate tip (Green) for the 64 transformation configurations offered by the Solid-State SMA flexural actuator*

CHAPTER 6
DISCUSSION

6.1 Introduction to the chapter

The highly multidisciplinary nature of this study has resulted in contributions in numerous areas. The purpose of this chapter is to interpret and critically analyse these contributions and their impact towards knowledge. The chapter is categorised into three sections, each exploring a different research contribution type. Section 6.2 explores methodological contributions made towards the field of experimental studies involving Shape Memory Alloys. Section 6.3 analyses the empirical research contributions that have advanced theoretical knowledge on SMA behaviour. Section 6.4 assesses the artifact type contributions that are heavily interlinked with the end application. This includes an analysis of contributions through Computational Techniques and Findings.

6.2 Methodological contributions

The experimental study comprises of several novel methodological approaches that have been adopted in the experimental set up, the

testing strategy, and the specimen preparation. Previous experimental studies that have explored NiTi SMA behaviour have either lacked temperature control or optical in-situ integration. This study shares many parallels with the DIC enabled micro-macro study conducted by Brinson eta al [12]. This inspired some of the methodological solutions adopted for this study, in particularly the use of a interference filter to allow observation at a granular level without the prerequisite of elaborate etching treatments. This study is an extension of such work, as it strives to provide a more complete map of NiTi behaviour utilising both temperature control and in-situ optical analysis. Due to this combination of data capture streams; the conception of the experimental study was of paramount importance, requiring numerous novel methodological solutions.

6.2.1 Experimental set up

One of the fundamental decisions was the use of 4-point flexural fixture as the bender mechanism for the experimental study. This choice was taken in spite of point-based bend fixtures being theoretically problematic in NiTi studies due to the creation of undesired axial loads at the support constraints. These stress concentrations, if large enough, can lead to the premature transformation to martensite near the bearings, and result in inaccurate displacement measurements. As a result, past NiTi studies have preferred the use of custom pure bending apparatus,

which negate the superimposing of different types of loading on the specimens or introduction of shear stresses. Some of the most notable attempts at pure bending NiTi studies include work conducted by Reizner et al. [15] and Redlunn et al [16] that employ displacement controlled, custom pure bending fixtures. While these studies demonstrate their successful implementation for the analysis NiTi flexural behaviour, there are restrictions in the practical aspects such as the integration with other apparatus. This was one of the driving factors behind the implementation of a 4-point bender mechanism, as it provided with seamless integration with the MTS loading frame, which together offered a large degree of scope in test strain and temperature ranges and rates. Moreover, some of the negative drawbacks associated with point-bending fixtures were negated through several measures: (1) The inhomogeneity of the material response necessitates the use of a four-point fixture, which exposes the specimen to peak stresses over an extended volume, compared to traditional three-point layout which concentrates stresses over the central bearing, (2) relatively small peak deformations in tests, (3) a flat contact surface between specimen and bearings to reduce stress concentrations, and (4) contact surfaces polished to reduce shear.

A unique solution adopted was the use of an inverted 4–point bend fixture. This was employed to restrict movement of the specimen centreline in the vertical axis during flexure. This in turn permitted the use of a higher magnification magnitude focused onto a smaller observable area. The optical camera had the capability to

be operated remotely, whilst still placed within the temperature chamber, and withstand the test temperatures. This experimental set-up enabled the capture of in-situ optical micrographs, with a degree of detail that permitted both DIC analysis and observation of NiTi at a granular level.

Another stream of in-situ analysis that could have benefited this study is the observation of the thermal signature. This could be accomplished by using an Infrared camera, which can detect the instantaneous local heating of the domains due to the released latent heat during phase transformation. The synchronization of both kinematic and thermal measurements would lead to a highly attractive complete thermo-mechanical characterisation of phase transformation behaviour. However, the integration of such a technique alongside optical microscopy was logistically very difficult (antagonist surface texture requirements, imaging devices having different pixel and acquisition rates [85]). However, there is a novel technique developed by Maynadier et al. [85]—Infra-Red Image Correlation—synchronizes kinematic and thermal measurements and thus negates many of these drawbacks. This could be explored in future studies.

6.2.2 Specimen preparation

The primary focus of this effort was to stabilise the highly non-linear, loading history dependent behaviour of NiTi SMA. Heat

treatment of the material was undertaken to reset any cold working or damage the material had previously sustained. The annealing conditions suggested in Saikrishna et al's study of TMC effects [77] were employed as they ensured a large grain size, benefiting the optical in-situ investigation. To reduce the impact of TMC on material response, the specimens were thermally cycled between austenite and martensite phases in a water bath. Miyazaki et al [78] have demonstrated that such cycling is paramount in the stabilisation of the M_f and M_s temperatures.

The optical in-situ study observes the specimen edge to track changes in variant microstructure and relates it to specimen behaviour as a whole. For this to be accomplished, two criteria had to be met: (1) a polished surface of the specimen edge that allowed observation at a microstructural level, and (2) zero damage imparted on the specimen edge so it is representative of the specimen behaviour. As these can be conflicting requirements, careful consideration was necessary in the conception of the specimen preparation. In particular, steps such as the use of EDM for the specimen cutting were implemented to negate damages to the observed specimen edge.

6.2.3 Test strategy

The test schedule was conceived to analyse the behaviour of NiTi plate flexural deformation under a magnitude of conditions: thermo-cycling, constant strain temperature ramps, and constant

temperature strain ramps. Each test condition was designed to offer a unique perspective into the response of a NiTi plate actuator. Such an actuator centric study of SMA is unique, as most studies tackle SMA behaviour primarily on a theoretical level without linking it with an end application.

Meticulous planning was necessitated to successfully implement the testing schedule due to the nature of the material: previous studies have reported on a continuous change in the functional properties of the NiTi such as the transformation temperatures, transformation hysteresis and strain response under thermo-mechanical cycling [77]. As this study comprised of 132 tests, which effectively subjected the 3 test specimens to thermo-mechanical cycling throughout the study; the stability of the material response was a concern. Several measures were taken to dramatically reduce such effects, including careful thermal preparation of the specimens, use of low peak deformation magnitudes and careful workload management between the specimens in the experimental tests. The option to completely ignore thermo-mechanical cycling effects—employing a vast number of specimens—was not explored as it does not truly reflect the required characteristics of the NiTi plate actuator, a high cycle element with uniformity of performance required throughout its life cycle.

A major drawback in the experimental study, was the limitation of the test temperature range to A_f-10°C → A_f+10°C. This range is

restricted due to the lack of active cooling in the environmental chamber, which prevents tests being undertaken below ambient temperature and also the maximum operating temperature of the digital camera, which prevents tests being undertaken over 50°C. The temperature range should be sufficient to capture forward and reverse transformation at most load levels. Nevertheless, the integration of active cooling in future studies is a vital step, as it would allow recreation of the extreme temperatures that would be experienced by the NiTi plate actuator.

6.3 Empirical contributions

While the broader aim of the experimental study was the evaluation of material behaviour under the possible operating envelope of the NiTi plate actuator, it also assessed several NiTi SMA behavioural aspects that have academically significant implications. This section explores these contributions and their impact towards the existing understanding of SMA behaviour.

6.3.1 A complete map of transformation behaviour

Phase transformations, temperatures and applied stresses are closely intertwined where one affects the other. A complete map of SMA behaviour thus requires both the study of the stress and temperature induced phase transformation. However, due to the

difficulty of integrating the aspect of temperature control with loading frames, limited studies have attempted the analysis of both phase transformation mechanisms. One study of note that studied stress-strain response of SMA plate with variance in temperature is Adharapurapu's [135] evaluation of stress-strain response at quasi-static and high loading conditions. While tests were conducted at different specimen temperature conditions, it was restricted to constant temperature tests, as there were no means of in-situ temperature control.

This study on the other hand, through the use of the MTS environmental chamber, is capable testing NiTi behaviour at a range of temperature condition and temperature ramp rates. As a consequence, this study can be regarded as the only study to date that evaluates temperature and stress induced transformation behaviour in the flexural deformation regime. These attributes enabled this study to construct a complete phase diagram, showing the effect of applied flexural deflection on the phase transformations for the tested specimens.

6.3.2 Effects of loading rates

The constant temperature tests repeat every loading sequence at three loading rates: $1x10^{-4}s^{-1}$, $1x10^{-3}s^{-1}$ and $1x10^{-2}s^{-1}$. Changes in response were observed macroscopically between the quasi-static and high strain rate tests. Quasi static loading conditions exhibited characteristic NiTi behaviour, with the difference between the forward and reverse martensitic phase transformations inducing a

stress hysteresis loop. This effect was less obvious during dynamic high-rate loading conditions, with loading and unloading response being closely matched. This was attributed to the faster latent heat release of the dynamic loading condition that carried latent heat accumulation from the loading phase to the initial stages of the unloading phase. The effect of latent heat generation on SMA response, while minor during the experimental tests, can significantly impact SMA actuator operation as it can promote undesirable occurrences such as unintended actuation.

While the global behaviour of SMA response is largely unaffected by changes in strain rate, there are more substantial changes to its microstructure. Such a hypothesis was formed by Brinson et al. [81] as they observed that in quasi-static loading conditions stress induced martensite formed from a single band, while dynamic loading conditions resulted in the presence of the formation in multiple bands. To the author's knowledge, the implications on loading rate for bend tests using full-field in-situ methods such as DIC are largely unexplored. However, integration of DIC to variable strain rate tests requires a macro-level implementation, which does not permit observation of localised behaviour at a granular level. As a result, in-situ DIC in this study was limited to constant strain tests.

6.3.3 Relationships between macroscopic behaviour and microstructural observations

A majority of SMA related experimental studies either focus on a

micro or macro level approach. However, micromechanical studies are often theoretical and not directly applicable to end applications whereas macro level studies do not contain enough depth to explain the observed phenomena. This study combines microstructural and macroscopic analysis via in-situ optical investigation during flexural deformation tests. The employment of both approaches allowed relationships to be constructed, explaining material behaviour in greater detail.

The bend tests that allow the simultaneous evaluation of the material behaviour under both tensile and compressive deformation modes provide valuable insight into the flexural response of NiTi SMA. While classical Euler–Bernoulli bending kinematics assumes a linear strain profile across the cross section, the heterogeneous nature of the bending strain fields in NiTi result in a much more complex strain profile. In their bend study, Reedlunn et al. [80] report a significant shift of the neutral axis under bending. Similarly, the strain field maps in this study indicate a shift of the neutral axis towards tension. Through the use of NiTi plate specimens, this study avoids the appearance of the Brazier effect, a phenomena that could have affected Reedlun's results. Moreover, this study offers a richer understanding of the two deformation modes as it uses broader testing conditions studying both stress and temperature induced phase transformation.

In addition, this study was able to identify the granular level strain localisation activity. This behaviour is particular evident under tension, where NiTi is known to exhibit strain localization and propagation during portions of stress induced transformations [82].

Under flexural loading, however, the development of strain localisations can be non-linear due to the presence of compressive and tensile deformation modes in varying magnitudes through the specimen thickness. In their study of Superelastic NiTi tube, Reedlunn et al. highlight this effect, reporting on strain localisations in tension and on the absence of strain localisations in compression [80]. The DIC strain field maps gained from the constant strain tests in this study, further establish this phenomenon. In this study, such localisations in tension were only present at certain temperatures, which coincided with the specimen's martensitic phase, while at specimen temperatures above A_f, there were no strain localisations patterns. This does not translate to a hypothesis that these strain localisations bands are limited to martensitic temperatures, as it can be argued that the maximum tested strain magnitude of 1% is insufficient to introduce a stress induced martensite fraction that promotes such behaviour.

5.5 Artifact contributions

The objective of this study was the creation of a viable alternative utilising NiTi SMA's, to replace the archaic, pneumatically driven VSV system currently used in gas turbine engines. The design-driven journey undertaken towards the realisation of the solid state VSV actuator presented many challenges. The novel artifact type solutions that address them advance the understanding of SMA actuator design and gas turbine engine Actuator implementation.

One of the primary considerations in the design of a SMA actuator

is the establishing of its form and the mechanism of strain recovery/application it will adopt for actuation. The earliest uses of SMA have been in the form of 1-dimensional NiTi wire, which form linear actuators of considerable complexity to induce morphing behaviour. The SAMPSON F-15 inlet cowl is an example of such implementation, using SMA bundle containing 34 wire rods in a complex chain driven mechanism [62]. A more recent study by Advact [72] use NiTi plates in an opposing actuator arrangement to form an adaptive nozzle. Such a solid-state type implementation is more attractive due to its intrinsic simplicity and the potential for integration as a structural member. These advantages were the driving factors behind the use of NiTi in plate form for the proposed VSV actuator.

The strain recovery mechanism was governed by the requirements of the VSV actuator: the end product would need to manipulate incoming airflow so the subsequent rotors and stators work at best efficiency. As the study aims for a truly solid-state solution – the proposed system's VSVs individually "bend" to simultaneously meet the desired angle of attack and assume the ideal aerofoil shape. Using ABAQUS FEM, two models were designed each exploiting a contrasting strain recovery/application mechanism: (1) One dimension "pull" model with a linear actuator, (2) Two dimensional "push" mode with a flexural actuator. The 1-dimensional mechanism was more energy dense as it achieved marginally higher tip deflection magnitudes, though this came at the expense of higher strain envelope. On the other hand, the two-dimensional

model did not require an additional structure to induce the motion, as the bend motion was achieved through a similar flexural type strain recovery/application mechanism. For this reason, and the implications it has on the simplicity of the overall system, the flexural type was identified as the mechanism that the VSV concept would employ.

The presented replacement for the VSV system combined several novel features:

(1) A truly Solid-state design – The NiTi plates alone account for 100% of the structure. They assume the profile of the VSV and act as stress members. The eradication of superfluous structures is instrumental for a reliable and affordable system.

(2) Faster Activation / de-activation times – The thin SMA plate actuators have a very high surface/volume ratio. This form factor promotes the absorption and dissipation of heat. Moreover, the NiTi plates are mirrored along the horizontal axis, adopting an opposing actuator philosophy. While this substantially increases the range of tip deflection magnitude, a secondary benefit is reduction in deactivations times through momentary activation of an opposing NiTi plate.

(3) Multiple morphed profiles – The 6 NiTi plates are of 3 different lengths and arranged in a 3-3 configuration to form each VSV. Through individual activation of each plate, the system can offer 64 distinct morphed profiles. This offers significantly more flow conditions to the following rotors and stators.

(4) High deflection/Low strain – The NiTi plates are only constrained on the central plane, and are free to slide (like the pages in a book). This novel design, and the conscious use of relative thin SMA plate, combines to form a system with an intrinsically high deflection/strain ratio. This is a very important consideration in SMA actuator design, as a lower strain envelope would result in a greater lifespan.

However, as this system is still at a conceptual level, some of the more practical issues have not been addressed. Following are some potential pitfalls and possible solutions:

(1) Heat soak between the NiTi plates is a paramount concern. It can either lead to deactivation of an active plate due to heat loss, or unintended activation of an inactive plate due to heat transfer. An insulating layer between each NiTi plate is therefore necessitated to negate such effects. Silicone rubber would be an ideal material candidate, as it would provide the added benefit of damping instabilities caused by external factors such as turbulent airflow.

(2) The NiTi plates that form the VSV do not offer a continuous surface. As the jagged edges can potentially disrupt the airflow, smoothing of the profile using an outer membrane is necessary. Silicone rubber would be an ideal candidate again, as it would not substantially affect the performance of the actuator. Moreover, this would have the added benefit of insulating it from external temperature influences that could otherwise induce unintended activation.

CHAPTER 7

CONCLUSION

7.1 Thesis: In a nutshell

The content of the thesis can be summarised as an exercise in linking the theoretical knowledge of NiTi SMAs to a practical space. Background work included establishing a thorough understanding of the behaviour of Shape Memory Alloys, locating the opportunities for actuation available in gas turbine engines, and evaluating past studies that utilised SMA technologies in aerospace applications. Using this knowledge base, an experimental methodology was devised focused on assessing criteria specifically related to SMA actuation demands. FEM techniques were employed, using data from the experimental study, to develop and analyse SMA actuator concepts for the gas turbine engine Variable Stator Vane assembly.

7.2 Motivations

The University of Sheffield's Dynamics group has a rich history of involvement in SMA-related research. In particular, through their collaboration with the ADVACT group, they have made profound contributions towards the use of SMAs in aerospace applications. The Group also boasts strong links with Rolls Royce through their University Technology Centre, with collaborative studies dating back to 1993. The initial motivation for this research can be traced back to the Dynamic Group's active participation in these fields. Moreover, the knowledge base within the Group has provided an exceptional foundation for the start of this research.

The desire to undertake this specific topic of work, on the other hand, has stemmed from two key realities: (1) the lack of real world applications using SMAs for actuation purposes, and (2) the parallel shortage of theoretical studies, especially consisting of practical experimental work, on aspects of SMA behaviour unique to actuation applications.

7.3 Summary of Literature Review

Due to the diverse array of topics that this work links together, the assessment of past literature and studies are categorised into several sections. The common aim of each of these exercises is to contribute towards the subsequent experimental and computational

studies. The initial surveys into past work were in an attempt to build up a broad knowledge base. These include evaluation of (1) SMA behavioural aspects, and (2) opportunities for actuation in gas turbine engines. This work established the suitability of SMA based actuation systems, and revealed the predominantly archaic nature of actuation technology utilised in gas turbine engines. In effect, this provided with a potential problem and a potential solution. This study was followed by a more incisive effort aimed at pinpointing a specific gap in the research area. To accomplish this, an assessment of past experimental studies employing in-situ techniques or experimentally observed SMA behaviour in the flexural behaviour was undertaken. It was noted that the combination of these two aspects would lead to a novel study. A parallel review of SMA related aerospace applications was undertaken. Through this, a lack of studies relating to blade-morphing actuation systems was detected. These two literature reviews jointly aided in establishing the specifics of the experimental study. Lastly, selection of a fitting model for computational development and analysis purposes demanded for the review of the current eco-system of SMA related models. Through this exercise, it was determined that the Auricchio developed ABAQUS UMAT model was the most suitable for the requirements of this research.

7.4 Summary of Methodologies

The novel experimental study combines in-situ observational techniques to assess a wide array of NiTi SMA criteria specific to actuation applications. The most important experimental technique utilised in the study, however, lies beneath the surface, as it is specimen preparation. Amidst the complex, non-linear, mechanical and thermal load history dependent material response of NiTi SMAs, it is paramount that the specimens are able to produce a consistent material response throughout their test schedule. This entailed the specimens to undergo a gruelling conditioning regime, which included: (1) EDM Machining, (2) Heat treatment, (3) Thermal cycling, and (4) Surface grinding and polishing.

The setting of appropriate test parameters in the test schedule was a vital element, closely tied to the overall integrity of the experimental results. The determination of such parameters required preliminary experimental work to be undertaken: (1) DSC tests to locate material transformation temperatures and subsequent approximation of test temperatures, and (2) Uniaxial tensile tests on wire specimens to locate SMA mechanical deformation characteristics and subsequent approximation of test strain magnitudes.

The experimental set up was based around an MTS 858 load frame. The specimens were placed inside a Thermcraft environmental

chamber, on a custom designed *inverted* four-point bend fixture. In-situ optical investigations were obtained through a Panasonic Hx-A500 digital camera.

The computational study also entailed application of certain experimental techniques. The material parameters were determined through the experimental data from the four-point flexural study. This study was simulated through FEM to verify and validate the operational capability of the ABAQUS based FEM model. The validated model architecture was subsequently used to develop, present and evaluate SMA based actuator concepts.

7.5 Summary of findings

The findings presented through this body of work can be classified with respect to their origination; from (6.5.1) the experimental study, or (6.5.2) the computational study.

7.5.1 Experimental findings

The experimental findings are based on observations from the experimental study, consisted of evaluating criteria specific to actuation applications. The cyclic tests observed material response upon mechanical and thermal cycling. An interesting phenomena observed through this was the sudden shift of material response shift, attributed to the emergence of the R-Phase with repeated

thermo-mechanical cycles. The constant strain temperature sweep tests evaluated the effects that strain variation has on the material response as it is subjected to a thermal load cycle. This test provided valuable insight towards potential actuation response characteristics of SMAs. The constant temperature strain sweep tests evaluated the effects temperature change has on the material response as it is subjected to a mechanical load cycle. From a practical space, this was designed to investigate the effects of mechanical loading to a SMA actuator at any given thermal state. The in-situ DIC analysis based on the constant strain temperature sweep tests produced strain field maps that highlight the asymmetry between tension and compression. This asymmetry manifested as (1) strain localisation under tension, and (2) movement of the neutral plane towards tension.

7.5.2 Computational findings

The computational findings consist of assessing merits and drawbacks of the two SMA-based actuator concepts. This comparative study assessed the following operational criteria: (1) Evaluation of the Neutral State, (2) Evaluation of the Activated state, (3) Evaluation of the de-activated state, (4) Temperature vs. Deflection response, and (5) Strain vs. Deflection response. These efforts, together with all experimental and theoretical work undertaken in this study, summated in the final conceptualisation of the flexural type SMA based VSV actuator concept.

7.6 Contributions

The contributions brought by this thesis can be classified into five aspects: (6.6.1) Theoretical knowledge, (6.6.2) Experimental Techniques, (6.6.3) Experimental Findings, (6.6.4) Computational techniques and (6.6.5) Computational findings.

7.6.1 Theoretical knowledge

The preliminary Chapters of this thesis are focused on providing a suitable foundation in SMA literature and potential aerospace actuation applications. There are many studies that have performed evaluations exclusively focused on one subject: Lagoudas' study of SMA modelling and engineering applications [2], and Horn's assessment of gas turbine Actuation opportunities [54] are outstanding examples. The novelty of this study is in the interlinking of these two subjects: SMAs are introduced with a view towards gas turbine actuation applications and vice versa. The compilation of this focused narrative thus contributes to the theoretical knowledge base. This work is particularly beneficial for any future undertakings, which attempt to link SMAs to aerospace applications.

7.6.2 Experimental Techniques

Past in-situ type SMA flexural studies have been localised towards analysis of SMA behaviour at either a martensitic or Austenitic

thermal condition. The absence of thermal control in these studies stipulate this restriction. Attempts from Reedlunn et al. [16] fall into this category. Their evaluation of SMA tube bending characteristics introduced numerous experimental solutions, some of which have been adapted for this study. Through the use of similar techniques, such as in-situ optical investigation to locate local strains, several comparisons can be drawn between the two studies. However, this study extends Reedlunn's efforts by introducing thermal control to the tests, enabling the investigation of actuation specific characteristics. This necessitated the adaption of a novel experimental methodology, inclusive of an original experimental set-up that was capable of investigating both thermal and stress induced transformation behaviour of SMAs. The use of this innovative approach can be classed as a contribution towards the SMA experimental methods field.

7.6.3 Experimental Results

The novel experimental methodology produced an equally novel set of experimental findings that advance the theoretical knowhow pertaining to SMA actuation design. The combination of the thermo-mechanical cycling, temperature sweep and strain sweep tests provided a comprehensive map of behavioural aspects specific to actuation applications in the flexural domain. The analysis of the behaviour at a granular level through DIC produced strain field maps provided insight into the asymmetrical, localised behaviour

that the stress induced martensitic transformation undergoes. This inhomogeneity in behaviour could potentially have detrimental repercussions to the life span of a NiTi based actuator.

7.6.4 Computational Techniques

The built-in Auricchio developed constitutive model in ABAQUS was chosen as the framework for all subsequent FEM modelling and analysis. Whilst this model has been traditionally employed to model Superelastic behaviour of SMAs [92], this study manipulates the material parameters to simulate shape memory effect induced actuation. The methodology adapted for the Computational study involved a validation and verification exercise between the FEM model and four-point bend study. The linking between the data from the experimental work to the computational data provided a successful and original solution for this task. The end result was the creation of a model architecture, which is adept at simulating SMA actuation behaviour in the flexural deformation mode.

7.6.5 Computational Findings

The computational study was able to introduce a new *Push* type, two-dimensional flexural NiTi SMA plate actuator concept. A comparative study ensued, pitting it against a conventional *Pull* type, one-dimensional linear NiTi plate actuator, where it closely matched performance criteria. This concept was further developed

into a Final VSV concept, boasting 64 activation configurations. The originality and the effectiveness of this final concept signifies a notable contribution towards the growing field of SMA-based actuation.

7.7 Future research directions

This work can be used as a framework to stem numerous adjacent studies. As this study blends theoretical, experimental and practical efforts, each of these disciplines contains exciting future possibilities:

7.7.1 Theoretical

The full-field in-situ DIC analysis of variable strain tests under constant temperatures has not been attempted in the flexural deformation regime. This was omitted in this study because of the requirement of granular level strain distribution observation, which necessitated a high degree of magnification. Such an analysis would interlink with the parallel constant temperature strain sweep tests.

7.7.2 Experimental

The Auricchio FEM model accepts individual parameters for tension and compression to define NiTi behaviour. Tension only and

compression only stress-strain testing of the specimens would be ideal in identifying these tension and compression specific material parameters for the FEM model.

Four-point flexural investigation on shape-set flexural NiTi plates. This would simulate the behaviour of the prestrain condition and strain recovery mechanism adopted for the VSV concept. This could stem a comparative study with which the accuracy of the model can be further improved.

7.7.3 Practical

The FEM model can be further extended to include a thermal analysis. This inclusion enables the evaluation of phenomenon such as heat transfer between NiTi plates, and heat transfer between the NiTi plates and the environment.

The fabrication and experimental investigation of the Flexural VSV actuator concept is an essential step in the realisation of the SMA based system. The replication of the actuation profiles experimentally would be very insightful, especially if it is paired with in-situ DIC analysis.

REFERENCES

[1] Wu, M., Schetky, L., (2000). Industrial Application For Shape Memory Alloys. Proceedings of the International Conference on Shape Memory and Superelastic Technologies, pp 171-182.

[2] Lagoudas, D., (2008). Shape Memory Alloys: Modelling and engineering Applications. Texas: Springer.

[3] Kauffman, G., Mayo, I. (1993). Memory Metal. Chem Matters. pp 4-7.

[4] Warlimont, H., Delaey, L., Tas, H., Krishnan, R.V., (1974). Thermoelasticity, pseudoelasticity and the memory effects associated with martensitic transformations. Journal of Materials Science. Vol. 9 (9), pp 1521-1535.

[5] Sun, Q., Hwang, K., (1993). Micromechanics modeling for the constitutive behavior of polycrystalline shape memory alloys. Journal of Mechanical Physics and Solids , 41, p 1-19.

[6] Buehler W.J. & Wang F.E., (1967), A summary of recent research on the NiTiNOL alloys and their potential application in ocean engineering, Ocean Eng. 1, pp 105-120.

[7] Funakubo, H., (1987). Shape memory alloys. New York: Gordon and Breach Science Publishers. pp 275.

[8] Breme HJ. Rev Meetall., (1989), pp 625.

[9] Van Humbeeck J, Stalmans R, Besselink PA., (1998), Shape Memory Alloys, Metals as biomaterials. Ed. 1. Chichester: Wiley and sons, pp 73-100 Chichester: Wiley, pp 73.

[10] Otsuka, K., Wayman, C. M., (1999) “Introduction,” in Shape Memory Alloys, K. Otsuka and C. M. Wayman, Eds., chapter 1, pp 1–26. Cambridge University Press.

[11] Vandygriff, E.R., (2002). Fabrication and characterisation of porous NiTi Shape Memory Alloy by elevated pressure sintering. PhD Thesis.

[12] Mizar, P.M., (2005). Thermomechanical characterisation of NiTiNOL and NiTiNOL based structures using ACES methodology. PhD Thesis.

[13] Kaufman, L., Cohen, M., (1958) martensitic transformations, in Progress in Metal Physics, B. Chalmers and R. King, Eds., vol. 7, pp 165–246, Pergamon Press.

[14] Wayman, C.M., (1989) An introduction to martensite and shape memory engineering Aspects of Shape Memory Alloys ed T W Deurig et al (Boston, MA: Butterworth-Heinemann) pp 3–20.

[15] Schuerch, H.U., (1968) Certain physical properties and applications of Nitinol NASA Report Cr-1232, NTIS N69-11420, pp 1–23.

[16] Dye, T.E., (1990), An experimental investigation of the behavior of Nitinol MSc Thesis Virginia Tech, Blacksburg, VA, USA.

[17] Bekker, A., Brinson, L.C., (1997) Temperature induced phase transformation in a shape memory alloy: phase diagram based kinetic approach J. Mech. Phys. Solids, 45, pp 949–88.

[18] Jonnalagadda, K.D., Sottos, N.R., Qidwai, M.A., Lagoudas, D.C.. (2000). In situ displacement measurements and numerical predictions of embedded SMA transformation. Smart Material Structures. 9 (2), pp 701-710.

[19] Duerig, T.W., Melton, K.N., Stockel, D., Wayman, C.M., (1990) engineering aspects of shape memory alloys (London: Butterworth) Heinemann, Part I & Part II.

[20] Liu, Y., Xie, Z., van Humbeeck, J., Delaey, L., (1999). Some results on the detwinning process in NiTi shape memory alloys. Scripta Materialia 41, pp 1273–1281.

[21] Schetky, L., (1979), Shape-memory alloys, Scientific American, vol.

241, pp 74–83.

[22] Wayman, C.M., (1988) Transformation and mechanical behaviour of NiTi shape memory alloys, Phase Transformations ’87, G. W. Lorimer, Ed. Inst. of Metals, pp 16–19.

[23] Airoldi, G., Rivolta, G., (1988) Order of transition in R-phase of NiTi alloys, Phase Transformations ’87, G. W. Lorimer, Ed. Inst. of Metals, pp 74–75.

[24] Fukuda, T., Kakeshita, T., Kitayama, M., Saburi, T., (1995) Effect of aging on martensitic transformation in a shape memory Ti-40.5Ni-10Cu alloy, Journal de Physique IV, R. Gotthardt and J. Van Humbeeck, Eds., vol. 5, pp 717–722.

[25] Pelosin, V., Riviere, A., (1998) Effect of thermal cycling on the R-phase and martensitic transformations in a Ti-rich NiTi alloy, MMTA, vol. 29A, no. 4, pp 1175–1180.

[26] Miller, D.A., Lagoudas, D.C., (2001) Influence of cold work and heat treatment on the shape memory effect and plastic strain development of NiTi, Material Science and engineering A, vol. A308, pp 161–175.

[27] Bataillard, L., Gotthardt, R., (1995) Influence of thermal treatment on the appearance of a three step martensitic transformation in NiTi, Journal de Physique IV, R. Gotthardt and J. Van Humbeeck, Eds., December 1995, vol. 5, pp 647–652.

[28] de Silva, C.W. (2005). Vibration and Shock Handbook : CRC press.

[29] Perkins, J., Sponholz, R.O., (1984), Stress-Induced martensitic Transformation Cycling and Two Way Shape Memory training in CuZnAl Alloys, Metall. Trans. 15, pp 313.

[30] Stachowiak, G.B., McCormick P.G., (1988), Shape memory behavior associated with the R and martensitic transformations in a NiTi alloy, Acta Metall. 36, pp 291.

[31] Eggeler, G., Hornbogen, E., Yawny, A., Heckmann, A. Wagner, M.,

(2004), Structural and Functional Fatigue of NiTi Shape Memory Alloys. Materials Science and engineering A378, pp 24.

[32] Saikrishna, C.N., Venkata Ramaiah, K., Bhaumik, S.K., (2006), Effects of thermo-mechanical cycling on the strain response of Ni-Ti-Cu shape memory alloy wire actuator, Materials Science and engineering A428, pp 217.

[33] Ramaiah, K.V., Saikrishna, C.N., Dhananjaya, B.R., Bhaumik, S.K., (2008) Proceedings of internation conference on smart structures and systems, Bangalore, IISc.

[34] Bhaumik, S.K., Saikrishna, C.N., Ramaiah, K.V., Venkataswamy M.A., (2008), Trans. Indian Inst. Met., 61, pp 435.

[35] Stalmans, R., Humbeeck, J.V., Delaey, L., (1991), Journal de Physique IV, 1, C4, pp 403.

[36] Jiang, X., Hida, M., Takemoto, Y., Sakakibara, A., Yasuda, H., Mori, H., In situ observation of stress-induced martensitic transformation and plastic deformation in TiNi alloy. Materials Science and engineering A 238, pp 303–308.

[37] Bhagyaraj, J., Ramaiah, K.V., Saikrishna, C.N., Gouthama, Bhaumik, S.K., (2009) Conference proceedings of electron microscopy and allied fields and XXX annual meeting of EMSI, New Delhi: Janvani Prakashan, pp 18.

[38] Erbstoeszer, B., Armstrong, B., Taya, M., Inoue, K., (2000), Stabilization of the shape memory effect in NiTi: an experimental investigation, Scripta Materialia, 42, pp 1145.

[39] Melton, K.N., Mercier, O., (1979), Fatigue of NiTi thermoelastic martensites, Acta Metall., 27, pp.137–144

[40] Eggeler, G., Hornbogen, E., Yawny, A., Heckmann, A., Wagner, M., (2004), Structural and functional fatigue of NiTi shape memory alloys, Mater. Sci. Eng., A 378, pp. 24–33

[41] McNichols, J.L., Brooks, P.C., (1981), NiTi fatigue behaviour, J. Appl. Phys., 52, 7442–4

[42] Tobushi, H., Hachisuka, T., Yamada, S., Lin, P.H., (1997), Rotating-bending fatigue of a TiNi shape-memory alloy wire, Mech. Mater., 26, pp. 35–42

[43] Tobushi, H., Hachisuka, T., Hashimoto, T., Yamada, S., (1998), Cyclic deformation and fatigue of a TiNi shape memory alloy wire subjected to rotating bending, J. Eng. Mater. Technol., 12064–70

[44] Young, J.M., VanVliet, K.J., (2005), Predicting invivo failure of pseudoelastic NiTi devices under low cycle, high amplitude fatigue, J. Biomed. Mater. Res., B 72, pp. 17–26

[45] Miyazaki, S., (1990) engineering Aspect of Shape Memory Alloys, (London: Butterworth– Heinemann)

[46] Miyazaki, S., Mizukoshia, K., Uekib, T., Sakumac, T., Liu, Y., (1999), Fatigue life of Ti 50 (at.%) Ni and Ti 40Ni 10Cu (at.%) shape memory alloy wires, Mater. Sci. Eng., A 273–275 658–63

[47] Gall, K., Maier, H.J., (2002), Cyclic deformation mechanisms in precipitated NiTi shape memory alloys Acta Mater., 50, 4643–57

[48] Bertacchini, O.W., Lagoudas, D.C., (2003), Fatigue life characterization of shape memory alloys undergoing thermomechanical cyclic loading, Proc. SPIE 5053, 612–24

[49] Bigeon, M.J., Morin, M., (1996) Thermomechanical study of the stress assisted two way memory effect fatigue in TiNi and CuZnAl wires, Scr. Mater., 35, 1373–8

[50] Predki, W., Klonne, M., Knopik, A., (2006) Cyclic torsional loading of pseudoelastic niti shape memory alloys: damping and fatigue failure, Mater. Sci. Eng., A 417, 182–9

[51] Gall, K., Tyber, J., Wilkesanders, G., Robertson, S.W., Ritchie, R.O., Maier, H.J., (2008), Effect of microstructure on the fatigue of hot-rolled and cold-drawn NiTi shape memory alloys, Mater. Sci. Eng., A 486, pp. 389–403

[52] Reynaerts, D. van Brussel, H. (1991). A SMA High Performance Actuator For Robot Hands. Journal De Physique IV. Vol. 1 (C4), pp 157-162.

[53] Stoeckel, D., (2011), Shape Memory and Superelasticity: From Scientific Curiosity to Life Saving Technology, Presentation, Jones Seminar on Science, Technology, and Society.

[54] Horn, W., Ardey, S., Grauer, F., Schmidt, K., Staudacher, S. (2008). Opportunities and Challenges for more Intelligent gas turbine engines. Deutscher Luft- und Raumfahrtkongress. 81265, pp 1-3.

[55] Culley, D., Garg, S., Hiller, S.-J., Horn, W., Kumar, A., Matthews, H.K., Moustapha, H., Pfoe rtner, H., Rosenfield, T., Rybarik, P., Schadow, K., Sitharu, K., Viassolo, D.E., Webster, J.. (2009). More Intelligent gas turbine engines. RTO Technical Report, Chapters 1 & 2.

[56] Turner, T. L., Buehrle, R. D., Cano, R. J., Fleming, G. A., (2004) Design, Fabrication, and Testing of SMA Enabled Adaptive Chevrons for Jet Noise Reduction, SPIE Vol. 5390, pp 297-308.

[57] Turner, T. L., Cabell, R. H., Cano, R. J., and Fleming, G. A, (2004) Design, Fabrication, and Testing of a SMA Hybrid Composite Jet engine Chevron, SPIE Vol. 6173.

[58] Turner, T. L., Buehrle, R. D., Cano, R. J., and Fleming, G. A, (2006) Modeling, Fabrication, and Testing of a SMA Hybrid Composite Jet engine Chevron Concept, Journal of Intelligent Material Systems and Structures, 17(6),

[59] Calkins, F., Butler, G., and Mabe, J., (2006) Variable Geometry Chevrons for Jet Noise Reduction, AIAA- 2006-2546.

[60] Webster, J.R., Potential Applications for Smart Technologies Within gas turbines, (2006) ISABE-2001-1109.

[61] Webster, J.R., (2006), High integrity adaptive SMA components for gas turbine applications, SPIE Smart conference 2006.

[62] Pitt, D.M., Dunne, J., White, W., Garcia, E., (2001), Wind tunnel demonstration of the SAMPSON Smart Inlet. Proceedings of SPIE, 2003. 4332: pp 345.

[63] Care, I., Seamus, G., Jiffri, S. (2011). Bearing assembly with damper. European Patent Application. 10194831.1.

[64] Soares, C., (2008). gas turbines: A handbook of Air, Land, and Sea Applications. Texas: Butterworth-Heinemann. pp 125-132.

[65] Cervenka, M., 2000, Rolls-Royce Trent engine, PowerPoint presentation, Rolls Royce, Derby.

[66] Kumar, A., Mukherjee, A.. (Unknown). Vibration of Blade Assembly in a gas turbine. Department of Mechanical engineering, Indian Institute of Technology Kharagpur, India 721302.

[67] Krishnan, V.B.,. (1996). Design, fabrication and testing of a Shape Memory Alloy bases Cryogenic Thermal Conduction Switch. PhD Thesis.

[68] Vilar, Z.T., Leal, A.S.C., dos Santos, A.G., Cavalcanti, M.B.A., de Araujo, C.J., (Unknown), Thermomechanical Characterisation of a CFRP-NiTi Composite Active, Bairro Universitário.

[69] http://01db-cn.orionis.fr/dma-instruments.7/dma-instruments.150/dma-100.411/?L=1., DMA+100 brochure, Last accessed August 2012.

[70] Van Humbeeck, J.. (1996). Damping properties of Shape Memory Alloys During Phase Transformation. Journal De Physique IV. 6 (C8), pp 371-380.

[71] Song, G., Ma, N., (2001) Control of Shape Memory Alloy Actuators using Pulse Width Pulse Frequency (PWPF) Modulation, the Proceedings of 2001 International Mechanical engineering Congress & Exposition.

[72] ADVACT Aerospace. (2010). Development of Advanced Actuation concepts to provide a step change in technology used in future aero-engine control systems. Final Publishable Report.

[73] Huang, S., Leary, M., Attalla, T., Probst, K., Subic, A., (2012), Optimisation of Ni–Ti shape memory alloy response time by transient heat transfer analysis, Materials & Design, 35: 655- 663

[74] Tawfik, M., Ro, J., Mei, C., (2002), Thermal post-buckling and aeroelastic behaviour of shape memory alloy reinforced plates, Smart Materials and Structures, 11, pp. 297–307

[75] Walther, R., (2006). Advanced engine Technology: Precondition for Economy, Profitability and Environmental Compatibility in Future Civil Air Transportation. MTU Aero engines GmbH.

[76] Wickramasinghe, K., Tomlinson, R., Rongong, J., (2014) In situ Observation of NiTi Transformation Behaviour: A Micro–Macro Approach, Experimental and Applied Mechanics, Volume 6: Proceedings of the 2014 Annual Conference on Experimental and Applied Mechanics, Conference Proceedings of the Society for Experimental Mechanics Series

[77] Saikrishna, C., Ramaiah, K., Prabhu, S., Bhaumik, S., (2009) On stability of NiTi wire during thermo-mechanical cycling. Bull Mater Sci 32(3):343–352

[78] Abeyaratne, R., Chu, C., James, R., (1994). Kinetics and hysteresis in martensitic single crystals. In: Proceeding of symposium on the mechanics of phase transformations and shape memory alloys

[79] V. Brailovski, P., Terriault, S., Prokoshkin, J., (2002) Materials engineering. Performance, Vol 11, 614

[80] Reedlunn, B., Churchill, C., Nelson, E., Shaw, J., Daly, H., (2014) Tension, compression, and bending of superelastic shape memory alloy tubes. J Mech Phys Solids 63:506–537

[81] Brinson, L., Schmidt, I., Lammering, R., (2004) Stress-induced transformation behavior of a polycrystalline NiTi shape memory alloy: micro and macromechanical investigations via in situ optical microscopy. J Mech Phys Solids 52(7):1549–1571

[82] Bechle J, Kyriakides S (2014) Localization in NiTi tubes under bending. Int J Solid Struct 51:967–980

[83] GonzalezI, H., Oliveira, C., *; FilhoI, E., Filho, O., AraújoI, C., (2010), Mat. Res. vol.13 no.3 São Carlos July/Sept.

[84] Liu, Y., Xie, Z., Van Humbeeck, J., Delaey, L., (1999) Effect of texture orientation on the martensite deformation of NiTi shape memory alloy sheet. Acta Mater 47(2):645–660

[85] Maynadier, A., Poncelet, M., Lavernhe-Taillard, K., Roux, S., (2013). One-shot thermal and kinematic field measurements: infra-red image correlation. In: Conference proceedings of the society for experimental mechanics series 2013, pp 243–250

[86] Khandelwal, A., Buravalla, V., (2009), Models for Shape Memory Alloy Behavior: An overview of modeling approaches, International journal of structural changes in Solids – Mechanics and Applications Volume 1, Number 1, December 2009, pp. 111-148

[87] Birman, V., (1997). Review of mechanics of shape memory alloy structures, Appl. Mech. Reviews 50, pp. 629-645.

[88] Bernardini, D., and Pence, J., (2002). Shape memory materials, modeling. In: Encyclopedia of Smart Materials, John Wiley & Sons, pp. 964–980.

[89] Paiva , A., and Savi, M., (2006). An overview of constitutive model for shape memory alloys, Math. Prob. Engg. 2006, pp. 1-30.

[90] Smith, R., (2005). Smart Material Systems- Model development, SIAM, Frontiers in Applied Mathematics, SIAM, USA.

[91] Lagoudas, D., (2008) Shape memory alloys: modelling and engineering applications. Springer, Texas

[92] Arghavani, J., Auricchio, C., Naghdabadi, R., Reali, A., Sohrabpour, S., (2010), A 3-D phenomenological constitutive model for shape memory alloys under multiaxial loadings, International Journal of Plasticity 26, 976–991

[93] Auricchio, F., Taylor, R., (1997), Shape-memory alloys: modeling and numerical simulations of the finite-strain superelastic behavior, Computer Methods in Applied Mechanics and

engineering, 143 (1–2), pp. 175–194

[94] Auricchio, F., Taylor, R., Lubliner, J., (1997), Shape Memory Alloys: macromdelling and numerical simulations of the superleastic behavior, Computer Methods in Applied Mechanics and engineering, 146, 281-312

[95] Rebelo, N., Walker, N., Foadian, H., (2001) Simulation of implantable stents, Abaqus User's Conference, 143, pp. 421–434.

[96] Gong, X., Pelton, A., (2003), Finite Element analysis on NiTiNOL medical applications, Proceedings of IMECE-2002, vol.53, 1-2

[97] Rebelo, N., Hsu, M., and Foadian, H., (2000), SMST-2000: Proceedings of the International Conference on Shape Memory and Superelastic Technologies, eds. S.M. Russell and A.R. Pelton, pp.457-469.

[98] Rebelo, N., Gong, X., Connally, M., (2003), Finite Element Analysis of Nitinol's Plastic Behaviour, SMST-2003: Proceedings of the International Conference on Shape Memory and Superelastic Technologies

[99] Lee, H., Withers, R., (1978), Search for the electronic phase transition in NiTi, Journal Applied Physics, 49, 5488

[100] Escher, K., Huner, M., (1990), Metallographical preparation of NiTi Shape Memory Alloys, Praktishe Metallographie, 27, 231-235

[101] Brazier, L., (1927) On the flexure of thin cylindrical shells and other "thin" sections. Proc R Soc Lond A 116(773):104

[102] Shaw, J., Kyriakides, S., (1995) Thermomechanical aspects of NiTi. Journal of the Mechanics and Physics of Solids 43 (8), 1243–1281.

[103] Shaw, J., Kyriakides, S., (1997) Initiation and propagation of localized deformation in elaso-plastic strips under uniaxial tension, International Journal of Plasticity 13(10), 837-871

[104] Tobushi, H., Shimeno, Y., Hachisuka, T., Tanaka, K., (1998),

Influence of strain rate on superelastic properties of TiNi shape memory alloy, Mech. Mater., 30 141–150

[105] Humbeek, K., Cederstrom, J., The Present State of Shape Memory Materials and Barriers Still to be Overcome'. In, Proceedings of 'SMST-94 The First International Conference on Shape Memory and Superelastic Technologies'. 4

[106] Huo, Y., (1989). A mathematical model for the hysteresis in shape memory alloys, Continuum Mechanics. Thermodynamics. 1: 283–303.

[107] Ortin, J., (1992). Preisach modeling of hysteresis for a pseudoelastic Cu-Zn-Al single crystal, Journal of Applied Physics. 71: 1454–1461.

[108] Bekker, A., Brinson, L., (1998). Phase diagram based description of the hysteresis behavior of shape memory alloys. Acta Materialia 46(10): 3649-3665

[109] Likhacev, A., Koval, N., (1992). On the differential equation describing the hysteretic behavior of shape-memory alloys, Scripta Metall. Mater. 27: 223–227.

[110] Ivshin, Y., Pence, J., (1994). A constitutive model for hysteretic phase transition behavior, Int. J. Eng. Sci. 32: 681–704.

[111] Falk, F., (1980). Model free-energy, mechanics and thermodynamics of shape memory alloys. Acta Metallurgica 28 (12): 1773-1780.

[112] Falk, F., (1983). One-dimensional model of shape memory alloys. Archives of Mechanics 35(1): 63-84.

[113] Falk, F., Konopka, P., (1990). Three-dimensional Landau theory describing the martensitic transformation of shape memory alloys. Journal de Physique (2): 61-77.

[114] Müller, H., Xu, (1991), On the pseudo-elastic hysteresis. Acta Metallurgica 39

[115] Bertran, A., (1982), Thermo-Mechanical Constitutive Equations for the Description of Shape Memory Effects in Alloys, Nuclear engineering and Design, 74:173–182.

[116] Silva, P., (1995) Mechanical Modeling of Stress Induced Phase Transformation in Solids, M.Sc. Dissertation, University of Brasilia – Department of Mechanical engineering

[117] Souza, C., Mamiya, N., Zouain, N., (1998), Three-Dimensional Model for Solids Undergoing Stress-Induced Phase Transformations, European Journal of Mechanics A – Solids, 17:789–806.

[118] Motta, L.B., Guillen, L., Mamiya, N., Vianna, D., (1999), A Study on the Hardening in Particular Model for Pseudoelastic Materials," In: Proceedings of the 15th Brazilian Congress of Mechanical engineering.

[119] Auricchio, F., Lubliner, J., (1997), A Uniaxial Model for Shape Memory Alloys, International Journal of Solids and Structures, 34(27):3601–3618.

[120] Auricchio, F., Sacco E., (1997), A One-Dimensional Model for Superelastic Shape Memory Alloys with Different Elastic Properties Between austenite and martensite, International Journal of Non-Linear Mechanics, 32(6):1101–1114.

[121] Brandon, D., Rogers, C., (1992), Constitutive laws for pseudo-elastic materials, Journal of Intelligent Material Systems and Structures 3, 255-267

[122] Govindjee, S., Kasper, E., (1997), A Shape Memory Alloy Model for Uranium-Niobium Accounting for Plasticity, Journal of Intelligent Material Systems and Structures, 8:815–826.

[123] Leclerq, S., Bourbon, G., Lexcellent, C., (1995), Plasticity Like Model of martensite Phase Transition in Shape Memory Alloys, Journal de Physique IV, 5:513–518

[124] Tanaka, K., Nagaki, S., (1982) Thermomechanical Description of Materials with Internal Variables in the Process of Phase

Transformation, Ingenieur – Archiv., 51: 287–299.

[125] Tanaka, K., (1986), A thermomechanical sketch of shape memory effect: one dimensional tensile behavior, Res Mechanica 18, 251-263

[126] Tanaka, K., Hayashi, T., Itoh, Y., Tobushi, H., (1992), Analysis of thermomechanical behavior of shape memory alloys, Mechanics of Materials 13, 207-215

[127] Tanaka, K., Hayashi, T., Nishimura, F., Tobushi,H., (1994), J. Materials Engng Performance 3, 1- 9.

[128] Tanaka, K., Nishimura, H., Tobushi, E., Oberaigner, F., Fischer, F., (1995), Thermomechanical behavior of an Fe-Based shape memory alloy: Transformation Conditions and Hysteresis, Journal de Physique IV Colloque, 05, 463, 468

[129] Boyd, J., and Lagoudas, D., (1996), A Thermodynamical Constitutive Model for Shape Memory Materials. Part I. The Monolithic Shape Memory Alloy, International Journal of Plasticity, Vol. 12, pp. 805- 842. Part II. The SMA Composite Material," International Journal of Plasticity, Vol. 12, pp. 843-873.

[130] Brinson, C., (1993), One-Dimensional Constitutive Behavior of Shape Memory Alloys: Thermomechanical Derivation with Non-Constant Material Functions and Redefined martensite Internal Variable. Journal of Intelligent Material Systems and Structures 4(2): 229-242.

[131] Liang, C., Rogers, C., (1990). One-Dimensional Thermomechanical Constitutive Relations for Shape Memory Materials. Journal of Intelligent Material Systems and Structures 1(2): 207-234.

[132] Pang, B., (2009). Reliability-guided digital image correlation for image deformation measurement. Applied Optics March 2009 pp. 1535-1542.

[133] Pang, B., Li, K., (2011). A fast digital image correlation method for deformation measurement. Optics and lasers in measurement 49 2011 pp. 841-847.

[134] Liu, Y., Xie, Z., Humbeeck, J.V., Delaey, L,. (1998). Asymmetry of stress–strain curves under tension and compression for NiTi shape memory alloys. Acta Materellia 1998 46 pp. 4325–38.

[135] Plietsch, R., Ehrlich, K., (1997),. Strength differential effect in pseudoelastic NiTi shape memory alloys. Acta Materellia 1997 45 pp.2417–24.

[136] Orgeas, L., Favier, D., (1998) Stress-induced martensitic transformation of a NiTi alloy in isothermal shear, tension and compression. Acta Materellia 1998 46 pp. 5579–91.

[139] Adharapurapu, R., (2007) Phase Transformations in Nickel-rich Nickel-Titanium Alloys: Influence of Strain-rate, Temperature, Thermomechanical Treatment and Nickel Composition on the Shape Memory and Superelastic Characteristics. Doctoral dissertation, University of California

[140] Noebe, R., Gatdosh, D., Padula, S., Garg, A., Biles. T., Nathal, M., (2005) Properties and Potential of Two (ni,pt)ti Alloys for Use as High-temperature Actuator Materials, Metals and metallic materials 2005